석 . 박사 학위논문 등표지

Fabrication and Characterization of Organic Light Emitting Diodes based on Printed Electronic Approaches

Muhammad Zubair • 2014

A THESIS
FOR THE DEGREE OF DOCTOR OF PHILOSOPHY

Fabrication and Characterization of Organic Light Emitting Diodes based on Printed Electronic Approaches

Muhammad Zubair

Department of Mechatronics Engineering
GRADUATE SCHOOL
JEJU NATIONAL UNIVERSITY
2014. 08

Fabrication and Characterization of Organic Light Emitting Diodes based on Printed Electronic Approaches

Muhammad Zubair

(Supervised by Professor Kyung Hyun Choi)

A thesis submitted in partial fulfillment of the requirement for the
degree of Doctor of Philosophy

2014. 08

The thesis has been examined and approved.

Ki Rin Kwon

Thesis Director, Ki Rin Kwon, Professor, Department of Mechanical & System Engineering

Yang Hoi Doh

Yang-Hoi Doh, Professor, Department of Electronic Engineering

Chulung Kang

Chul-Ung Kang, Professor, Department of Mechatronics Engineering

KYUNG HYUN CHOI

Kyung-Hyun Choi, Professor, Department of Mechatronics Engineering

Jeongdai Jo

Dr. Jeong-Dai Jo, Korea Institute of Machinery and Materials

2014/05/27

Date

Department of Mechatronics Engineering
GRADUATE SCHOOL
JEJU NATIONAL UNIVERSITY
REPUBLIC OF KOREA

To

My mom and dad

Acknowledgements

In the name of Almighty Allah, the most merciful, the most beneficent. First, I would like to present my gratitude in front of Allah, Who gave me strength to accomplish this work.

I would like to thank my supervisor Prof. Kyung Hyun Choi for his trust, support, and supervision. The completion of this work would not be possible without his guidance and expertise. His thought-provoking seminars and discussions and a never-ending appetite for excellence I will admire and cherish forever. His encouragement and guidance during my high time and support and kindness during the down times have all been a source of motivation towards learning more and more. I am also thankful to Prof Yang Hui Doh, Prof Jeongdai Jo and Prof Sang Jae Kim for their useful lectures and discussions.

I want to thank my seniors and mentors including Dr. Ganeshthanaraj Ponniah, Dr. Maria Mustafa, Dr. Muhammad Naeem Awais, Dr. Khalid Rehman, Dr. Muhammad Nauman Malik, Dr. Adnan Ali, Dr. Navaneethan Duriasamy, and Dr. Thanh Tran.

I had the company of wonderful friends in lab that helped and made research enjoyable including Junaid Ali, Shahid Aziz, Ghayas ud din Siddiqui, Murtaza Mehdi, Memoon Sajid, Su Won, Hum Beoum, Hyun Woo Dang, Bong Su, Young Jin Yang and Jae Hee Park. The friends from university Dr. Anil Kumar, Safdar Ali, Rashid Ahmad, Farrukh Israr, Sohail Khan, Zahid Manzoor, Shokat Ali, Wasim Abbas, Thiyagarajan, Annathakumar, Aunshka, Sarwan, Ganesh, Dr. Kartick, Niroshana, Annan, Lakman and Jamil Choudhry made my stay in Jeju easy. I would like to mention my sports buddies Suresh Ria, Konak Kanti Kar, Dr. Konstantin Lyakhov and Dr Kalpa. Finally, I want to thank my good friends Kamran Ali and Vane Yao with whom I spent my most of time with during my stay in Jeju.

The support from family was the fuel for the whole journey and I want to thank my mom and dad for their love and support. I am thankful to my family for relaxing chats. Love you all.

Contents

List of Figures

List of Tables

ABSTRACT

The organic electronics have found their way into market with their devices like organic light emitting diodes and organic solar cells etc. Organic light emitting diodes are used in displays, large area lighting, advertising, information, and communications. Organic light emitting diodes have a number of advantages over the inorganic light emitting diodes. The organic light emitting diodes are fabricated using sustainable raw materials. Fabrication of organic light emitting diodes devices on R2R system can handle the future demands for mass production with low cost.

Fabrication of OLEDs by printed electronics is achieved by using electrohydrodynamics spray deposition technique (ESD). Spin coating technique has disadvantages like the wastage of material, limitations on the size of substrate and difficulties in forming thin films with nanoscale thickness. These problems can be solved by using cheap and easy ESD technique operated at room temperature and pressure conditions.

OLEDs are fabricated by employing conjugate polymers of PEDOT:PSS and MEH-PPV. ITO, aluminum, and silver are used as electrodes. The silver electrode is printed by a gravure offset printer installed on a R2R system. The web tension of R2R system is controlled for better printing. ZnO-graphene and CdSe/ZnS QDs are used to enhance the OLED performance. The thin films are characterized for their morphology, element analysis, optical analysis, and conductivity. Electrical and luminescence properties of organic light emitting diodes devices are also characterized. In the end, the spin coated samples are compared with ESD samples.

The fabrication of solution based, flexible, OLEDs on a mass scale is made possible by the use of simple and cheap printed electronics approaches of ESD technique and gravure offset printing.

1. Introduction

The field of printed electronics involves the implementation of advanced systems and specialized group of materials to develop electronics devices on various kinds of flexible substrates like plastic, paper or metal foils. The advantages of printed electronics include low cost, simple processes and solution based large area processing while all processing is performed at room temperature and atmospheric pressure. The techniques of printed electronics follow a mature field of graphic printing. The throughput in graphical printing is enhanced by R2R processing. Different types of printing systems like inkjet, flexographic, gravure offset and screen printers can be used in a R2R system. The graphical printing provides a road map for the field of printed electronics to fabricate electronic devices by printing techniques ensuring the mass production and cost effectiveness.

A breakthrough in materials opened new doors for printed electronics when three bright scientists (Heeger, MacDiarmid and Shirakawa) in 1970's showed conductivity in organic materials (Derivatives et al., 1977). They were awarded Nobel Prize in chemistry for their efforts in 2000. The organic electronics became a hot topic of research and lot of good work has been done in this area. Organic electronics offer the unique advantages such as low cost, flexibility, lightweight, chemically modifiable and easy availability of raw materials.

1.1 Organic Light Emitting Diodes (OLEDs)

In 1987 Tang and van Slyke presented the first organic light emitting diode with luminance performance using Alq_3 (Tang and VanSlyke, 1987). Since then there on a lot of research has been reported on OLEDs (Guo et al., 2013; Son et al., 2012). The conjugated polymer devices have advantages like easy fabrication, low cost, lightweight, human friendly, sustainable raw materials, very thin, large view angle, and fast response (Forrest, 2003; Mustafa et al., 2013). The solution-based polymers make the fabrication process easy as compared to the inorganic conventional LEDs (Nguyen et al., 2013). In OLEDs, usually ITO coated glass is used as the transparent anode on which a hole transport layer is casted by spin coating. On this hole transport layer, emissive layer is coated in which the holes and electrons combine and emit photon. Electron transport layer is coated on top of emissive layer. Finally, a reflective metallic layer is thermally evaporated onto the electron transport layer as the cathode (Nguyen, 2011; Saleh et al., 2009). The schematic diagram of a general OLED is shown in Figure 1-1.

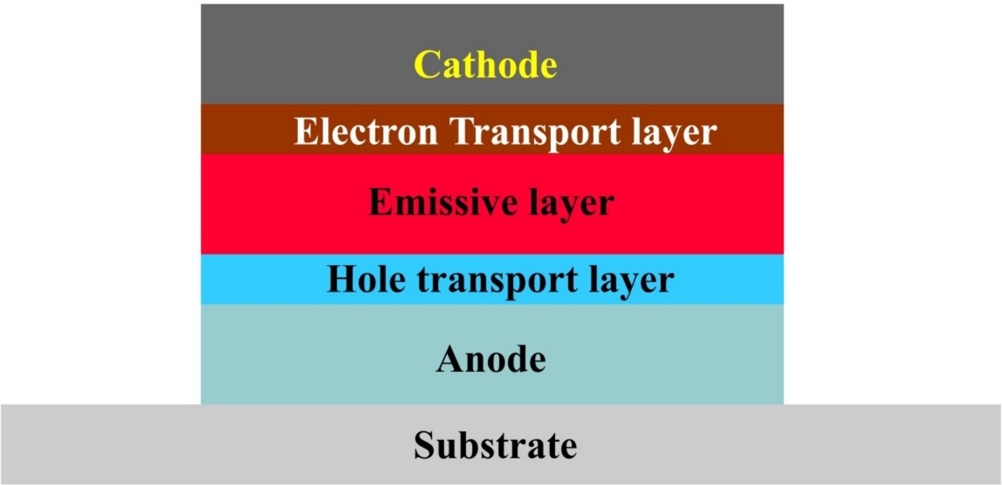

Figure 1-1: Schematic of an organic light emitting diode

1.2 Mechanism of OLEDs

The mechanism of OLEDs is based on the transport of holes and electrons from anode and cathode respectively by the help of hole and electron transport layers into the emissive layer where holes and electrons combines to emit a photon. Figure 1-2 shows the mechanism of OLEDs. High work function of anode enables the release of holes and lower work function cathode releases electrons as shown in Figure 1-3. The charge transfer in organic materials and quantum dots is generally by hopping mechanism. The electroluminescence of the device depends on an even transfer of holes and electrons in an emissive layer and layers thickness optimization. To facilitate the movement of holes and electrons multiple layers are added to perform tasks like charge injection, charge transport, and charge blocking.

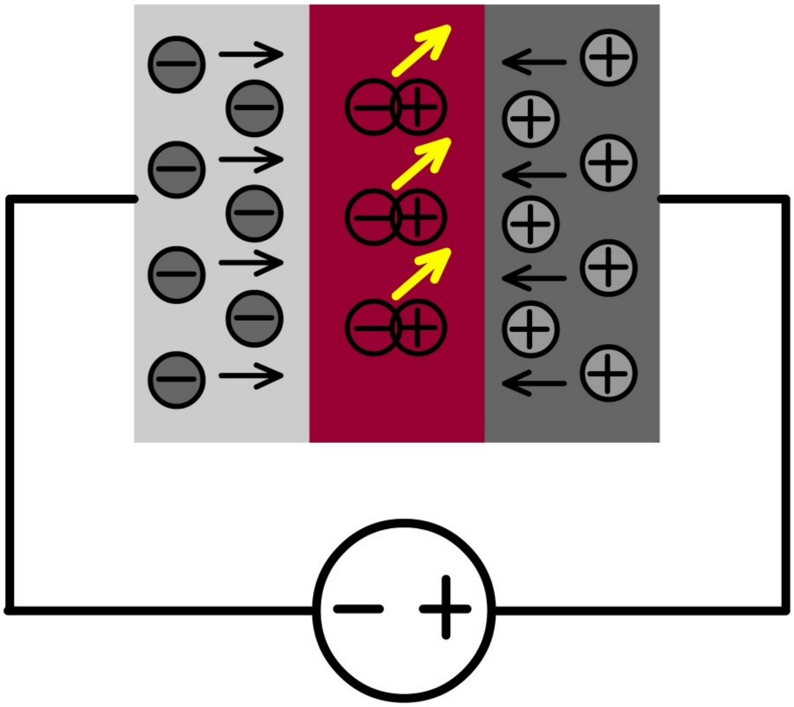

Figure 1-2: Working principle of an organic light emitting diode

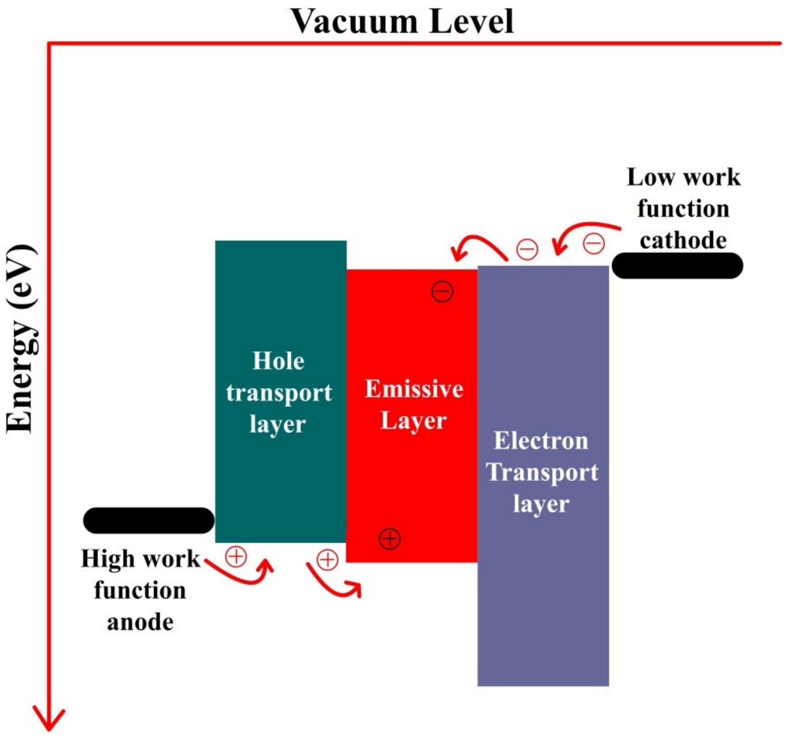

Figure 1-3: Energy level diagram for organic light emitting diode

1.3 Material for OLEDs

Different materials are used in the manufacturing of OLEDs. Here flexible OLEDs are under investigation; therefore, only the materials that can be processed under low temperature on plastic substrate are discussed. Here polyethylene terephthalate (PET) is used as the plastic substrate. The working temperature for PET substrate is below 120 ^{o}C. Metals conductors and organic conductors are used as electrodes. Usually one electrode is transparent and the other is reflective so that the concentrated light should be visible through the transparent electrode. The electrodes should have low resistance, environmentally stable, low surface roughness, chemically stable and should have work function based on their function as anode or cathode. Where work function is the amount of energy required to eject one electron from the surface of material. Electrodes in OLEDs are of metals, organic conducting materials and metal oxides. Metals in printed electronics are based on nanoparticles and nanowires. The nanoparticles are sintered to attain conductance. The metal electrodes are reflective in nature and can be used as one of the electrode while other electrode must be transparent for proper OLED lighting.

Organic conductors are also used in OLEDs. Organic conductors are still about 1000 times less conductive than the metals. PEDOT:PSS (Poly(3,4-ethylene dioxythiophene):poly (styrene sulfonate)) (Heywang and Jonas, 1992; Jonas and Schrader, 1991) is a conductive polymer which is commercially available and dispersible in water. With latest non-vacuum techniques, PEDOT:PSS is easily processable into thin films from aqueous solution and has high strength and flexibility. Apart from that it has excellent thermal, mechanical, and environmental stability. PEDOT:PSS prevents the electrostatic discharges during film rewinding, reduces dust buildup after processing and has high transparency in the visible range (Chin et al., 2010; Jönsson et al., 2003; Kim et al., 2002; Tsai et al., 2008). Carbon nanotubes are used as one-dimensional conductive electrode. Metal composites like silver nanowires blended with carbon nanotubes are used as electrodes. The organic electrodes are flexible and solution processable and many techniques are being used to enhance their conductivity so that they can compete with the metal and metal oxides electrodes.

In metal oxides Indium Tin Oxide (ITO) exhibits good transparency, high conductivity and it is commercially available etched on glass and PET substrates (Raoufi et al., 2007; Schmidt et al., 2009). ITO has its shortfall as well. ITO has poor mechanical flexibility (Aernouts et al., 2004; Koenig et al., 2001), releases Indium and oxygen in organic layer (de Jong et al., 2000b), has poor transparency for blue region (Na et al., 2008) and is a scarce earth metal which makes it expensive (Garter et al., 1999). Despite all disadvantages, ITO is still the leading transparent electrode in OLEDs applications. New materials are being under investigation while the conductivity of conducting polymer is enhanced to match the conductivity of ITO while keeping transmittance in good range.

Different organic and inorganic semiconductors are used in OLEDs. In organic materials, many materials can be used as semiconductor and emissive layers such as small molecules, oligomers, and polymers. Many organic emissive materials have been developed for OLEDs. The advantages of organic materials are their solution process ability and good charge mobility. Different hybrid materials are also used which have organic and inorganic blends. These hybrid materials offer the advantages of organic process ability and flexibility while they also enjoy the high charge mobility of inorganic materials.

To enhance the emissive characteristics of OLEDs, quantum dots (QDs) have been used (Bae et al., 2010; Cho et al., 2009; Shirasaki et al., 2012). QDs are nanocrystal with excellent emissive properties because of quantum confinement effect (Bera et al., 2010). The narrow emission wavelength of QDs is tunable throughout the visible spectra. Tunable band gap and solution process ability make QDs excellent candidates in many application such as emissive layers in OLEDs devices (Qiao et al., 2012; Tuan et al., 2011), composite materials (Zhang et al., 2013), solar cells (Li et al., 2012; Rath et al., 2011), electroactive polymers (Oh et al., 2013) and biological imaging (Bera et al., 2010). Figure 1-4 shows the size tunable luminescence of QDs.

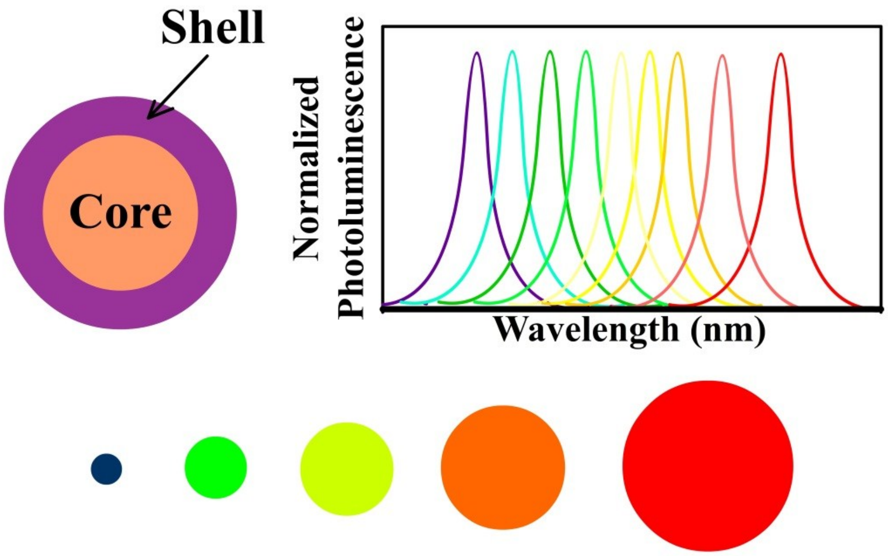

Figure 1-4: Shell core of QDs with their size tunable photoluminescence

1.4 Fabrication Processes

The solution-based fabrication of OLEDs can be performed by different methods like spin coating, dip coating, Langmuir-Blodgett technique, screen-printing and spray. The fabrication process for industrial scale demands the low cost operation with advantages like low cost materials at high volume manufacturing and low materials losses.

1.4.1 Conventional Processes

1.4.1.1 Spin Coating

Spin coating is performed by rotating the substrate and after ink is applied on substrate, the excess ink is spun out under the effect of centrifugal forces. Air pressure is used along with centrifugal forces for ultra-thin films. The spin coating has limitations such as it is limited to small areas, material loss is significant and this technique cannot be adopted for mass scale production.

1.4.1.2 Langmuir–Blodgett Technique

In Langmuir–Blodgett technique, an amphiphile is created in a water insoluble solvent. The amphiphide solution is attained by depositing it on the surface of water with the help of micro syringes. The amphiphile solution is compressed to form a uniform top layer. Now the substrate is dipped in the solution carefully at constant rate. The substrate is then pulled up while compressing the amphiphile layer to get a final monolayer with accurate thickness.

1.4.1.3 Dip Coating

Dip coating is the process where substrate is dipped in the solution. Then the substrate is pulled up for the thin film fabrication. In this process, a substrate is immersed in the solution at a constant speed without jerks so that the substrate is completely wet. Now the substrate is pulled out of the solution at a constant speed. This pulling out speed specifies the film thickness achieved on the substrate. The excess solution on substrate is drain from surface of substrate. Figure 1-5 shows the procedure of dip coating.

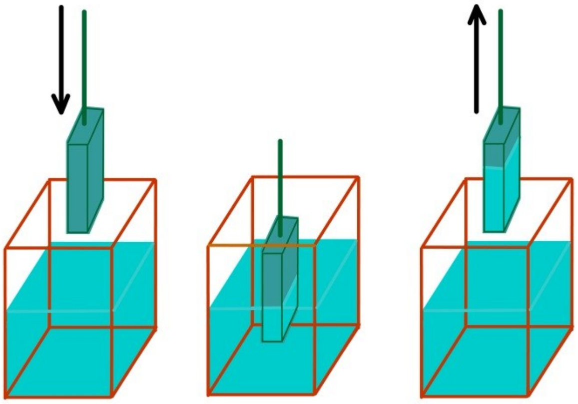

Figure 1-5: Procedure used for dip coating

1.4.2 Printed Electronics Processes

1.4.2.1 Slot Die

Slot die is simple method of coating. Slot die is an ink dispensing system that has three basic parts, which are cavity body, ink pump and die. The ink pumps push the ink into the cavity and ink is forced out of cavity from die. The lips of die are in close proximity of the substrate that moves at a uniform speed. Web tension, velocity, flow rate and the gap between the die lips and substrate are important parameter of printing by slot die. Figure 1-6 shows the slot die system.

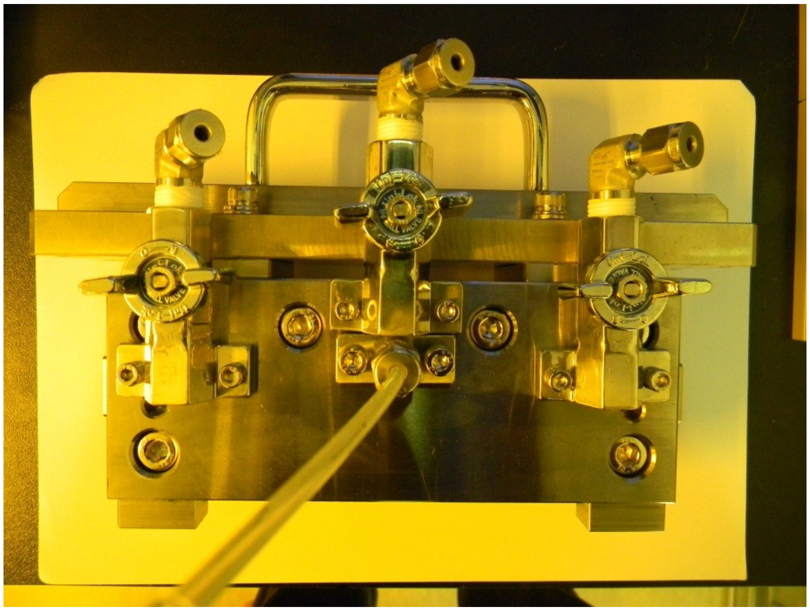

Figure 1-6: Slot die system

1.4.2.2 Inkjet printing

Inkjet printers are scalable for batch and large scale processing and provide flexibility to print any kind of pattern in a plane without wasting the expensive material, ink. The ink is pushed electrostatically or pneumatically through the nozzle to form a pattern also called a print. Commercial inkjet printers however had their share of problems, e.g. low ejection frequencies, limited applicable viscosities, thermal problems, nozzle clogging, nozzle size, and inability to make a smaller drop than their nozzle diameter (Kim et al., 2012).

Electrohydrodynamics Printing and Spray

Electrohydrodynamic (EHD) printing is achieved by pulling out functional ink from the nozzle and use of electric field to overcome the liquid surface tension. The schematic diagram of experimental setup required for electrohydrodynamics is shown in Figure 1-7. Therefore, this pulling of ink is in contrast to previous inkjet printer designs where ink is pushed out. EHD printing is one-step device printing technique with the capability to process a broad range of solution-based materials in terms of viscosity and conductivity.

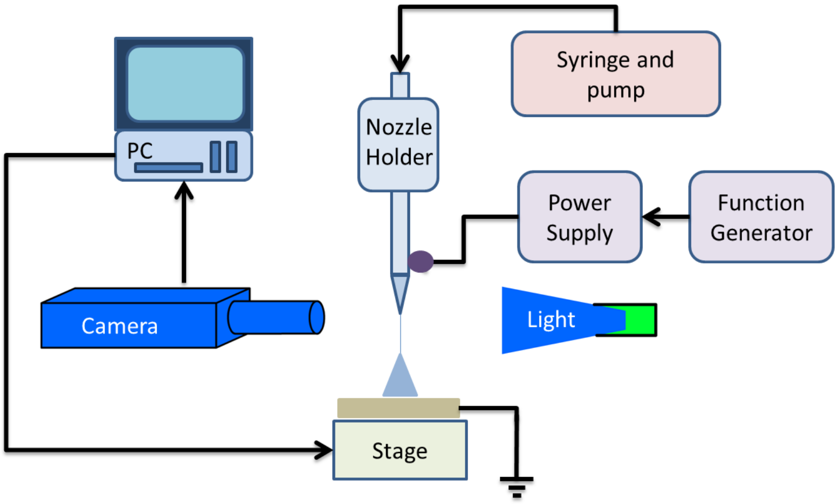

Figure 1-7: Electrohydrodynamics printing system schematic diagram

EHD is performed under ambient temperature and pressure conditions (S. Khan et al., 2011) and provides more throughput and speed than other inkjet techniques (Pikul et al., 2010). EHD printing is useful in many applications (Yang and Rida, 2007). EHD has created newer opportunities in many fields (K. Kim et al., 2010). EHD printing can be performed in continuous (Khan et al., 2012; Rahman et al., 2012b) and drop-on-demand (DOD) (D. S. Kim et al., 2011; Lee et al., 2012; Mishra et al., 2010; Rahman et al., 2012a, 2011) approach and spray for thin film fabrication. In continuous mode printing is performed after a stable taylor-cone jet is achieved, while in DOD patterns are created by falling droplets at certain frequency over a suitable substrate. The lines can be created by controlling the speed of head and the frequency of ejecting drops in DOD.

EHD can be performed on high frequencies; the printed patterns are smaller than their nozzle size. In EHD printing the aspect ratio of patterns can be controlled (Dickey et al., 2007; Onses et al., 2013). The pattern can be re-printed to increase the thickness. There is no need of register control as in the case of gravure-offset printer. A simple EHD setup is used here which is extremely cost effective as compared to gravure offset printer in which a fixed pattern can be patterned by an expensive gravure roll.

Electrohydrodynamics atomization (EHDA) is one of the easy, cost effective, and robust techniques for spraying which can be applied for large area spray applications using the same setup as shown in Figure 1-3. In the case of spray the standoff distance is increased. A cone is formed at the exit of capillary by the surface tension of the solution working against Maxwell stresses induced by the electric field. The jet breaks into droplets and further disintegrates into smaller droplets by Coulomb forces and this continually fission leads to micron sized droplets which are deposited on substrate and a uniform thin layer is achieved (Hayati et al., 1987, 1986; Leng and Lin, 2011). Under different voltages, different modes of EHDA phenomena can be observed. Different researchers have used EHDA for spray purposes of organic and inorganic materials (Awais et al., 2013a, 2013b; Choi et al., 2012b; Duraisamy et al., 2013, 2012a; Muhammad et al., 2012b; Mustafa et al., 2012). Muhammad et al. discussed characterization of ZnO sprayed by EHDA (Muhammad et al., 2012a). ZrO_2, TiO_2 and graphene oxide were sprayed by EHDA for memristor devices (Awais et al., 2013a; Choi et al., 2012a; Duraisamy et al., 2012b; Mustafa et al., 2012). Organic polymers like MEH-PPV, PEDOT:PSS, P3HT:PCBM and F8BT solutions were sprayed by EHDA by Muhammad et al. (Awais and Choi, 2013), Navaneethan et al. (Duraisamy et al., 2013, 2012a) and Maria et al. (Mustafa et al., 2013) respectively. Zhu et al. and Wei et al. showed that the QD in ionic liquid aided in the formation of polymer nanofibers by electrospinning process (Zhang et al., 2010; Zhu et al., 2011).

1.4.2.3 Screen Printing

In screen-printing, a woven mesh is used to transfer ink from the open areas of the mesh while restricting ink flow from the rest. A high viscosity ink is used in screen-printing which is squeezed through the screen by the help of a squeegee. During deposition, the substrate is placed just few mm below the screen. Film thickness is dependent on screen thread diameter, mesh count and viscosity of ink. The procedure of screen-printing is shown in Figure 1-8.

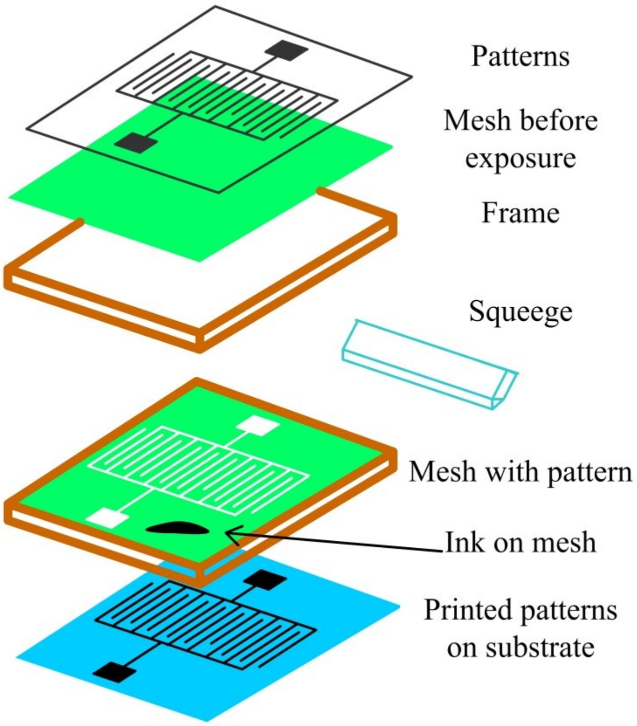

Figure 1-8: Process of screen-printing

1.4.2.4 Gravure offset printing

Gravure offset printer is a mass production system. In this system, patterns are engraved on a roll known as gravure roll. When this gravure roll is rotated after putting ink in engraves a doctor blade is used to remove excess ink. The ink in engraves is transferred to the PDMS layer of offset roll. This print is then transferred under pressure on the flexible substrate by the help of an impression roll as shown in Figure 1-9. The gravure-offset printer has high efficiency at high speed. The gravure-offset printer has the advantages of printing at high volume with good accuracy, good reproducibility, and low cost at high volumes.

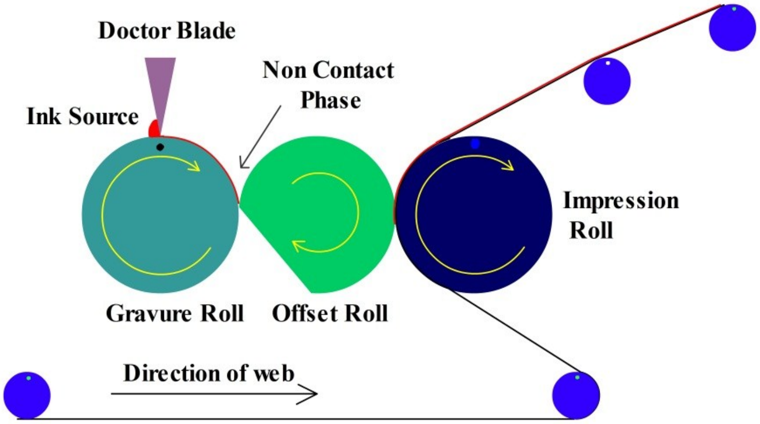

Figure 1-9: Gravure offset printer schematic diagram

1.4.2.5 Microgravure coating

Microgravure coating system is used to make a uniform thin film. A gravure roll, smaller in diameter, is used which has cells or well on the whole roll. The cells of microgravure are filled with ink by passing into ink sump. A doctor blade is used to remove the excess ink. The ink in the engraves is transferred onto the flexible substrate with the help of tension created by two idle rolls. The schematic diagram of microgravure is shown in Figure 1-10.

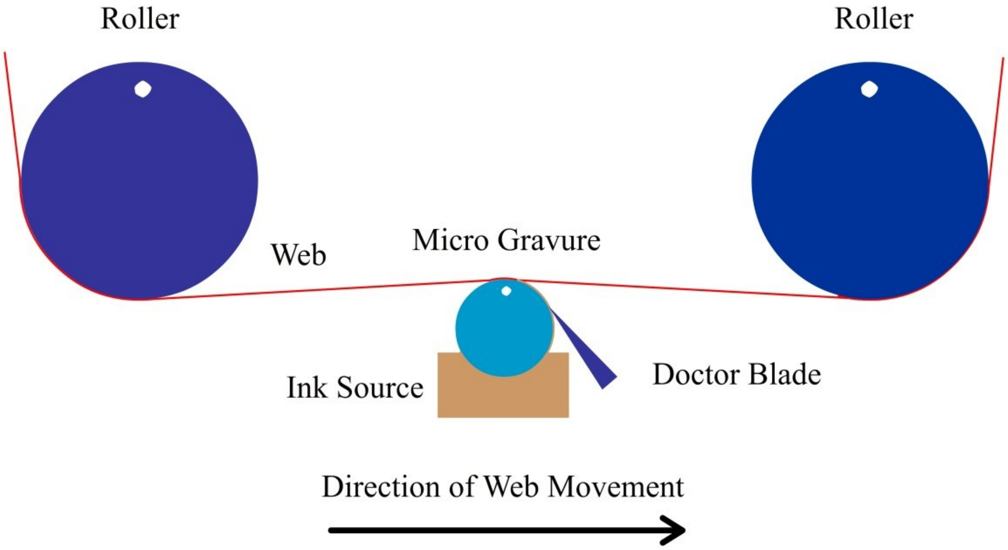

Figure 1-10: Microgravure printer schematic diagram

1.5 Development Orientation and Thesis Outline

R2R system is used for the mass production of devices. Organic light emitting diodes are being used in cell phones, televisions, displays, lighting and more. The annual requirements of OLEDs are growing very fast and by IDTectEx 2009-2029 Market Report (Das and Harrop, 2009) future growth will be doubled from 2013 to 2017 as presented in Figure 1-11. All personal devices will have OLEDs for display purposes.

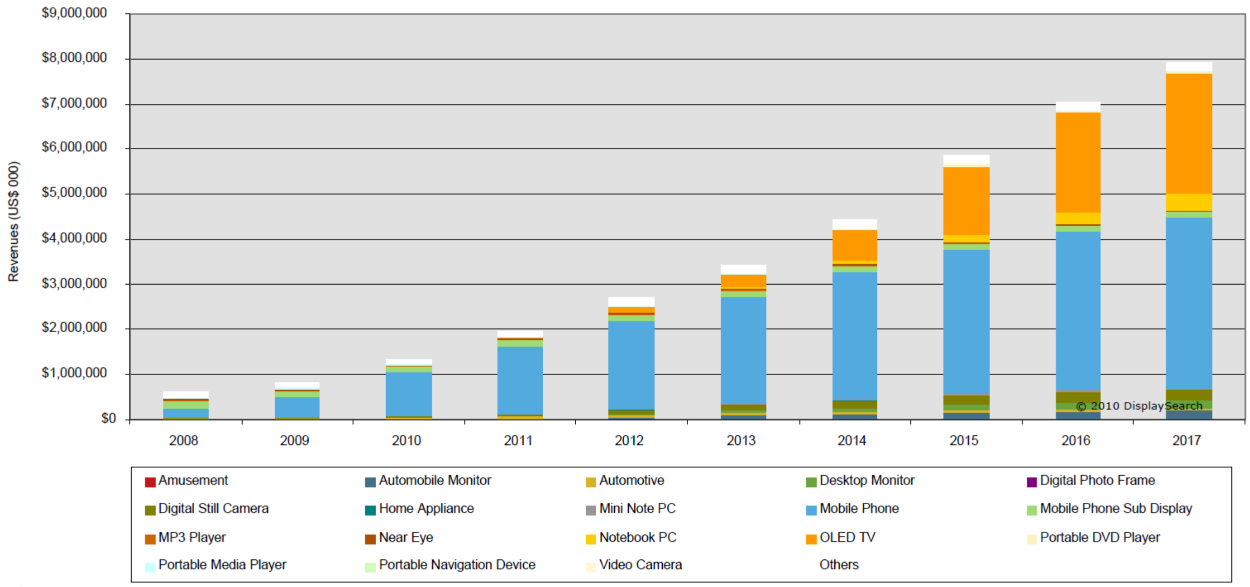

Figure 1-11: Future growth of OLEDs displays

Lighting is yet another big market that OLEDs will capture. Industry report on OLEDs lighting market report by Calvin Hsieh presented the future of lighting in OLEDs Lighting in 2009 and Beyond: the Bright Future (Hsieh, 2009) shown in Figure 1-13. The lighting revenue prediction shows more than 11 times increase from 2013 to 2018.

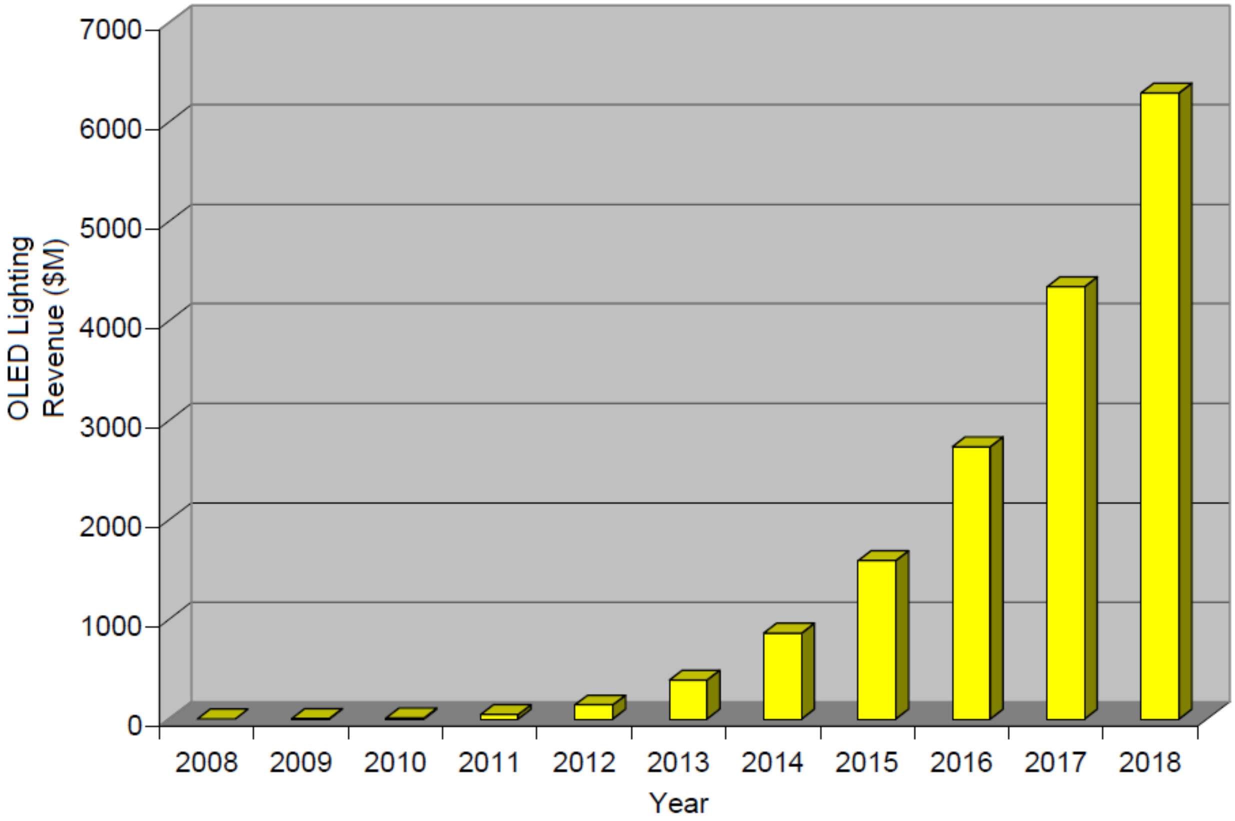

Figure 1-12: Future prediction of OLEDs lighting

The thesis is divided into four sections. First section discusses the inks and their recipes that are used for the fabrication the OLEDs. The next section describes the printed electronics hardware that is used as the experimental setup including spin coating, electrohydrodynamics system and gravure offset printing system. These printed electronics systems are installed on a Roll-to-Roll system so the control of Roll-to-Roll system is discussed. The third section describes fabrication of organic light emitting diodes. The forth section includes the results of the fabricated devices and discusses the comparison of classical spin coating fabrication technique with the printed electronics electrohydrodynamics technique. Finally, conclusions and future work are presented based on this research.

2. Materials for OLEDs

In 1987 organic light emitting diode with luminance performance were reported (Burroughes et al., 1990; Tang and VanSlyke, 1987) and they have seen a steady progress afterwards (S. W. Kim et al., 2010; Kulkarni et al., 2004; Reddy et al., 2006; Thejo Kalyani and Dhoble, 2012). OLEDs are advantageous for lower power consumption, better contrast, eco-friendly nature, large view angle, thin, lighter in weight and having better colour rendering index. Conjugate polymers, being semiconductors in nature, are also solution process-able. This solution process-able nature allows easy and economical large scale manufacture of the polymers based OLEDs whereas vacuum based processing is expensive (Saleh et al., 2009). In OLEDs, a transparent anode is used to provide holes while a metallic reflective electrode with lower work function is used as cathode to provide electrons. The electron-hole recombination within the emissive layer produces light (Chang et al., 2005). A balance transfer of electrons and hole is achieved by optimizing the layer thickness offer good electrical and optical properties.

2.1 Transparent Conductive Electrodes

In transparent electrodes, Indium Tin Oxide (ITO) exhibits good transparency and high conductivity (Raoufi et al., 2007; Schmidt et al., 2009) but has its shortfall as well. ITO has poor mechanical flexibility (Aernouts et al., 2004; Koenig et al., 2001), releases Indium and oxygen in organic layer (de Jong et al., 2000a), has poor transparency for blue region (Na et al., 2008) and is a scarce earth metal which makes it expensive (Garter et al., 1999). The comparable alternative transparent electrodes are conducting polymers, carbon nanotubes and metal nanowires. The carbon nanotubes have short life (Hagen et al., 2005; Ohno et al., 2010; Reich et al., 2005) and metal nanowires fail under current flow(Goldys et al., 2007; Khaligh and Goldthorpe, 2013) and conducting polymers still do not match the conductivity of ITO.

2.2 Solution Processable Materials

All solution processable materials were used in the fabrication of OLEDs. The inks were tailored to satisfy the electrohydrodynamics atomization conditions. In this research ITO, PEDOT:PSS and MEH-PPV were the basic materials. To enhance the OLED properties, quantum dots (QD) were used. Mostly aluminum was used as the top electrode of OLED devices. Aluminum is still not processable in printed electronics due to its problems of oxidation in atmospheric conditions. Therefore, the aluminum was thermally evaporated onto electron transport layer, which is a vacuum deposition technique. The work function of aluminum is -4.3 eV. The subsequent replacement of aluminum in printed electronics is silver. The silver has good conductivity, reflectance and is processable at lower temperature in nanoparticles form. The work function of silver is -4.5 eV that is higher than that of aluminum. This gives an edge to aluminum in OLED applications.

Poly (2-methoxy-5-(20ethyl-hexoxy)-1,4-phenylenevinylene) MEH-PPV powder (average molecular weight 40,000-70,000), ITO coated polyethylene terephthalate (PET), dimethyl sulfoxide (DMSO, 99.9%), dimethylformamide (DMF, 99.9%), were purchased from Sigma Aldrich (South Korea). Poly(3,4-ethylenedioxythiophene) Polystyrene sulfonate (PEDOT:PSS) was purchased from Agfa Materials Japan. Acetone, chloroform, and isopropanol were purchased from Daejon Chemicals and Metal Co, Ltd, South Korea. CdSe/ZnS QDs were prepared by Department of Chemical and Biomolecular Engineering, Yonsei University. All solvents were used as received.

2.2.1 Conjugate Polymers

2.2.1.1 PEDOT:PSS

The conductive polymers are used in many applications like optoelectronics (Friend et al., 1999; Günes et al., 2007), sensors (Arshak et al., 2009; Janata and Josowicz, 2003; McQuade et al., 2000), batteries (Suga et al., 2009), super capacitors (Mastragostino et al., 2002, 2001), and superconductors (Hayden et al., 2010; Pron and Rannou, 2002). Conductive polymer materials have advantages of low cost, lightweight, and large area coverage by vacuum free fabrication techniques(Chen et al., 2003). The PEDOT:PSS (Heywang and Jonas, 1992; Jonas and Schrader, 1991) is a conductive polymer which is commercially available and dispersible in water. With latest non-vacuum techniques, PEDOT:PSS is easily processable into thin films from aqueous solution and has high strength, flexibility, excellent thermal, mechanical, and environmental stability. PEDOT:PSS prevents the electrostatic discharges during film rewinding, reduces dust buildup after processing and has high transparency in the visible range (Chin et al., 2010;

Jönsson et al., 2003; Kim et al., 2002; Tsai et al., 2008). Many researcher have studied the conductivity enhancement of PEDOT:PSS (Ashizawa et al., 2005; Chin et al., 2010; Dimitriev et al., 2009; Gasiorowski et al., 2013; Jönsson et al., 2003; Kim et al., 2002; Lin and Su, 2012; Ouyang et al., 2004; Park et al., 2011; Semaltianos et al., 2010; Tsai et al., 2008; Wang et al., 2005). The conductivity was improved by heating, UV treatment, addition of solvents, adding nanowires and nanoparticles. Tsai et al. improved conductivity by heating the solution of PEDOT before deposition(Tsai et al., 2008). The conductivity was enhanced by adding and treating organic solvents like ethylene glycol (EG), 2-nitroethanol, methyl sulfoxide, 1-methyl-2-pyrrolidinone, poly(ethylene glycol) or dimethyl sulphoxide (Ashizawa et al., 2005; Chin et al., 2010; Dimitriev et al., 2009; Gasiorowski et al., 2013; Jönsson et al., 2003; Kim et al., 2002; Ouyang et al., 2004; Wang et al., 2005). Conductivity of PEDOT:PSS improvement by carbon nanotubes doping was reported by Park et al. (Park et al., 2011). Lin & Su and Semaltianos et al. used ZnO nanoparticles to improve the conductivity of PEDOT:PSS(Lin and Su, 2012; Semaltianos et al., 2010). Mechanical characteristic of PEDOT:PSS were discussed by Lang et al. (Lang et al., 2009) (Kim et al., 2002; Ouyang et al., 2004; Park et al., 2013). The conductivity improvement of PEDOT:PSS by pressing was also reported (Zubair et al., 2013). The structure of PEDOT:PSS is shown in Figure 2-1.

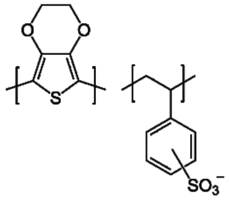

Figure 2-1: Conducting polymer PEDOT:PSS structure

2.2.1.2 MEH-PPV

MEH-PPV is a Light-emitting conjugated polymer soluble in toluene and chloroform. The band gap of MEH-PPV is 2.3 eV and its HOMO and LUMO values are 5.3 eV and 3 eV respectively. The excitation wavelength of MEH-PPV is 493 nm and emissive wavelength is 554 with toluene as solvent. MEH-PPV was dissolved in chloroform and its emissive wavelength was around 585 nm as reported in literature (Omer, 2012). The light emitted by MEH-PPV lies in orange-red colour zone. The structure of MEH-PPV is shown in Figure 2-2.

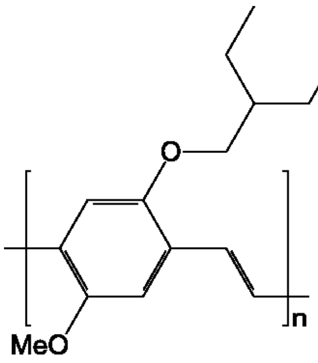

Figure 2-2: MEH-PPV polymer structure

2.2.2 Quantum Dots

To enhance the emissive characteristics of OLEDs, quantum dots (QDs) have been used (Bae et al., 2010; Cho et al., 2009; Shirasaki et al., 2012). QDs are nanocrystal with excellent emissive properties because of quantum confinement effect (Bera et al., 2010). QDs have the narrow emission wavelength that is tunable throughout the visible spectra. QDs have tunable band gap and are dispersed in solvents making them solution processable. The solution process ability make excellent candidates in many application as emissive layers in OLEDs devices (Qiao et al., 2012; Tuan et al., 2011), composite materials (Zhang et al., 2013), solar cells (Li et al., 2012; Rath et al., 2011), electroactive polymers (Oh et al., 2013) and biological imaging (Bera et al., 2010). Since homogenous and uniform spray of QDs in large area is an essential requirement in emissive devices (Bae et al., 2010), researchers have opted for dropping solution and then drying in oven (Suo et al., 2010), spin coating (Yeh et al., 2008), spin coating with air-shear force (Bae et al., 2010) and transfer printing (T.-H. Kim et al., 2011). Still there is a need to adopt a fabrication technique that can be deployed to produce thin film for large area coverage.

Different functional materials have been mixed with polymers in order to develop high efficiency, low power OLEDs (Saygili et al., 2011). Graphene has many advantages over other materials viz., high transparency, impermeability, elasticity, thermal conductivity (Klekachev et al., 2012; Sun and Shi, 2013). The lack of band gap gives graphene metal-like conductivity.

Graphene is already popular for improving performance of applications like fuel cells, photovoltaic cells, batteries, and sensors (Mukhopadhyay and Gupta, 2011). The lack of band gap makes graphene an ideal candidate for photovoltaic cell applications, yet this is a limiting property in the case of using graphene in an emissive application(Son et al., 2012). In OLEDs many researchers have used graphene as an electrode (Han et al., 2012; R.-H. Kim et al., 2011). The quantum confinement of graphene for band gap tuning has been studied (Lingling Li, Gehui Wu, Guohai Yang, Juan Peng, 2010). The quantum confinement effect on nanoscale materials offers high electrical and optical performance (Bera et al., 2010; Gu et al., 2004; Takei et al., 2011). A hybrid nanocomposite of graphene and QDs of high direct band gap material can transform graphene into a semiconductor with a finite band gap to have controlled electron flow (Jetson et al., 2010; Liu et al., 2013; Nguyen, 2011).

ZnO is a semiconductor with a high direct band gap of -3.37 eV (Muhammad et al., 2012a; Qiao et al., 2012), which offers the advantages of higher breakdown voltages, sustain high electric fields, lower noise and high temperature and power operations (K. H. Choi et al., 2010). ZnO is an ecofriendly material(Ramadoss and Kim, 2013) while extremely toxic heavy metals like Cadmium QDs are used for the same purpose (Willemse et al., 2011). ZnO has high exciton binding energy of 60 meV and high electron mobility(Park et al., 2010). Furthermore, ZnO QDs (0D) (Sidorov et al., 2010), confined in three dimensions, has better electrical and optical properties (Cheng et al., 2006). The quantum confinement makes the excitons to move to higher energies which result in increasing the energy gap(Yoffe, 2002). Combining graphene and ZnO QDs to make ZnO-Graphene QDs improves the electrical and optical properties for emissive applications (Son et al., 2012).

2.3 Ink preparation

Ink solution of PEDOT:PSS, MEH-PPV, ZnO-Graphene QDs, CdSe/ZnS QDs and silver nanoparticles paste were used in the experimentations. The inks were tailored from their spin coating recipes to fit the conditions of electrohydrodynamics atomization.

2.3.1 Inks for Spin Coating

PEDOT:PSS ink was prepared from the PEDOT:PSS paste. This paste was diluted using isopropanol in the ratio of 1:2 w/w. This solution was stirred for 20 minutes at 1500 rpm. After stirring, the solution was further diluted by drop by drop addition of deionized –water in ratio of 2:1 while continuously stirring. The solution was stirred for 2 hours at ambient conditions. The solution was filtered by polymeric filter (PTFE – 0.45 μm) to achieve homogenous dispersion. This method is explained clearly in previous work (Duraisamy et al., 2012a).

MEH-PPV ink of 0.5 % concentration was prepared in chloroform with viscosity of 4.76 mPa.s. MEH-PPV powder was dissolved in chloroform by bath sonication for 5 mins using ice packs and then magnetic stirred for 2 hrs. After stirring, the ink was stored in fridge to at 2 ^{o}C.

ZnO-Graphene QDs were obtained from a research institute which they made using the following process. To make the precursor solution of ZnO, 10 mmol of $ZnAc_22H_2O$ was added with 100 mL anhydrous ethanol. The solution was refluxed for 4 hours at 70 ^{o}C. $LiOH.H_2O$ of 3 mmol concentration was dissolved into 10 mL anhydrous ethanol. This solution was vigorously mixed with precursor solution to get ZnO QDs. The ZnO QDs solution was centrifuged for 10 min after adding 20 mL n-hexane. The precipitates were dissolved in anhydrous ethanol and the clear top solution was separated and dried to get powder of ZnO QDs. The prepared QDs were dispersed in N-methyl-pyrrolidone by bath sonication. Graphene flakes with less than 4 layers and surface area greater than 750 m^2/g where bought from Cheap Tubes. Graphene flakes were dispersed by ultra-sonication for 4 h at 50 % amplitude. The graphene was added to ZnO QD solution and mixed thoroughly by magnetic stirrer at temperature of 80 ^{o}C for 4 h. ZnO-Graphene QDs ink, with viscosity of 49.0 mPa.s measured by Viscometer VM-10A system.

CdSe/ZnS QDs were obtained from Kangtaek Lee and Cheolsang Yoon from Yonsei University, South Korea which they made using the following process. CdSe/ZnS QDs were synthesized using the previously reported method with modification (Lim et al., 2007). Briefly, 2 mmol of CdO, 4 mmol of $Zn(CH_3COO)_2$, 5 mL of OA were placed into 250 mL of three-neck flask with vigorous stirring, and the temperature was raised to 150 ^{o}C, followed by evacuation for 30 min. Then, 50 mL of 1-octadecene was added, and then reactor was heated to 300 ^{o}C to form $Cd(OA)_2$

and $Zn(OA)_2$. At the elevated temperature, 0.4 mL of 1 M TOPSe was rapidly injected into the reactor to produce CdSe cores. After 1.5 min, 0.6 mL of dodecanethiol was added drop wise at rate of 1 mL/min, and the mixture was allowed to react at 300 ^oC for 20 min under N_2 atmosphere. To passivate QDs, 4 mmol of sulfur dissolved in 2 mL of TOP was added, and the reaction proceeded for additional 10 min under N_2 atmosphere. Then the mixture was cooled to room temperature to produce CdSe/ZnS core/shell QDs. For purification, chloroform and acetone were added to the suspensions, followed by centrifugation at 7,000 rpm for 30 min and redispersion in toluene and DMSO cosolvent.

2.3.2 Inks for Electrohydrodynamics Spray

The conductivity of ink solution is tailored to fit the electrohydrodynamics phenomena. According to the classical electrohydrodynamic atomization of the stable cone jet mode, the electrical relaxation time, T_e, must be very much smaller than the hydrodynamic time, T_h (Gañán-Calvo et al., 1997). It is established by the inequality

$$\frac{\beta \varepsilon_o}{K} \ll \frac{LD}{Q} \tag{2-1}$$

where β is the relative permittivity, K is the electrical conductivity, L is the axial length of the jet, D is the jet diameter, Q is the given flow rate and ε_0 is the permittivity of vacuum ($8.85 \times 10{-}12$ Fm^{-1}). Here conductive solutions are increases the conductivity of ink, which results in reduction of the electrical relaxation time. The lower results in satisfying the inequality and achieve better spray results.

PEDOT:PSS ink was made from PEDOT:PSS screen printing paste. The paste was diluted with isopropanol in the ratio of 1:1.75 w/w. The solution was stirred for 30 mins. Conductivity of the solution was enhanced by adding DMSO in ratio of 7:1. The solution was stirred for 30 mins and then triton was added in ratio of 40:1. The solution was stirred again for 30 mins and then solution was filtered by using a polymeric filter and stored in fridge in a sealed bottle. The DMSO was added to enhance the conductivity of ink while the triton was added for better dispersion. The viscosity of ink was 20 mPa.s.

Different recipes for MEH-PPV electrohydrodynamics spray were used. Final working recipe is described here. 0.2 per cent concentrated MEH-PPV solution was prepared form MEH-PPV powder by bath sonication with ice packs for 5 mins and magnetic stirring for 2 hrs. DMF was added to this solution in the ratio of 3:1. Solution was stirred for 30 mins. 0.05 per cent ZnO nanoparticles of average size of 40 nm were dispersed in the solution. The final viscosity of the solution was 4.76 mPa.s. The ZnO nanoparticles were added to the ink solution to eliminate the electrospinning phenomena during electrohydrodynamics spray.

CdSe/ZnS QDs at 5 wt % were dispersed in toluene with Dimethyl sulfoxide (DMSO) as cosolvent. The viscosity of QDs solution was 0.56 mPa.s.

2.3.3 Paste for Gravure Offset Printing

The silver paste used for the fabrication of top electrode was bought from Advanced Nano Product Korea 363-942. The paste had silver nanoparticles contents of around 70 to 80 per cent. The viscosity of paste was between 10000 to 30000 cps. The sheet resistance was around 2 to 3 x 10^{-5} Ω cm.

3. Experimental Setup

3.1 Conventional Processes

Spin coating is a commercialized conventional printing process in which a uniform thin film on flat substrate is formed by spinning the substrate after putting a small amount of functional ink on the centre of substrate. The centrifugal forces act on the material poured on the substrate, and remove all access material, resulting in the formation of a thin film. The parameters to control the thickness of the film are coating speed, time, viscosity and concentration of ink and the solvent of ink. The spin coating is widely used in photolithography for the fabrication of 1 μm thick photoresist layer. Figure 3-1 shows the mechanism of a spin coating system

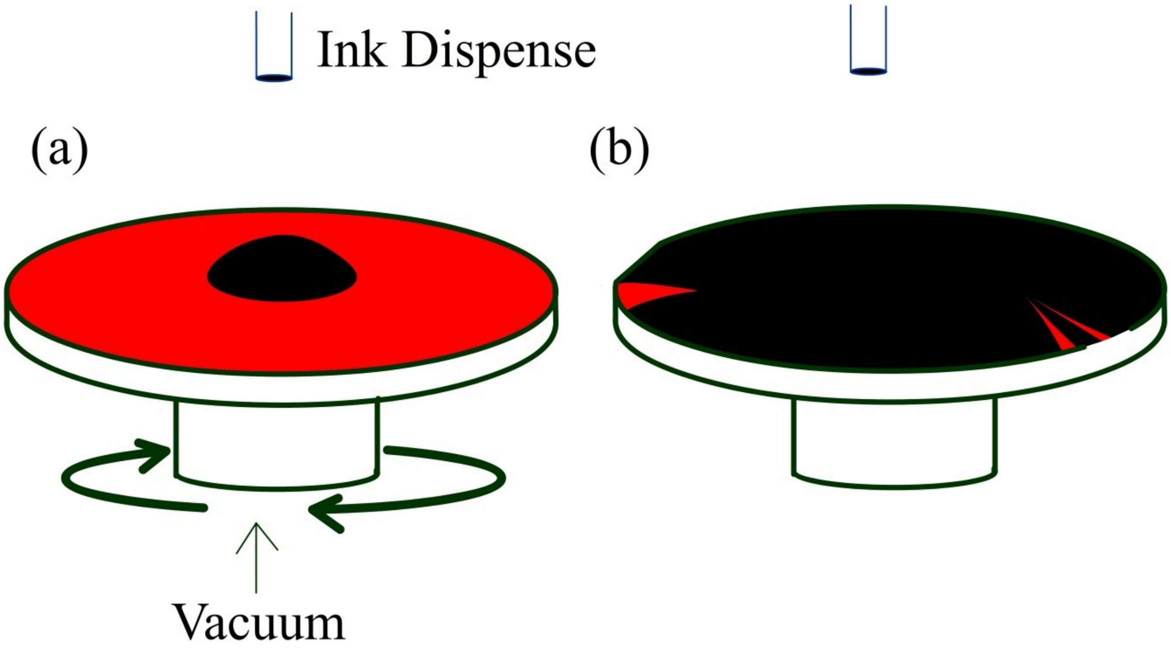

Figure 3-1: Spin coating system. a) Ink is dispensed onto substrate, which is held by vacuum, b) the substrate after spinning the substrate for a particular speed and time.

The spin coater (ACE-200) was used for the experiments to fabricate OLEDs. The spin coater is shown in Figure 3-2.

Figure 3-2: Spin coating system (ACE-200)

3.2 Printed Electronics Processes

Different printed electronics processes are discussed in Section 1.4.2. In this research, electrohydrodynamics spray technique was used for the fabrication of thin films from those processes. A gravure offset printer was used to fabricate top electrodes of an OLED. The electrohydrodynamics printing system and gravure offset printing system were installed on a Roll-to-Roll (R2R) system. To achieve the full potential of these printing systems web tension control of the R2R system was required. The web tension control and integration of these printing systems on R2R system is discussed here before describing the printing systems.

3.2.1 Roll-to-Roll System

The R2R processing for electronics, also known as web processing or reel-to-reel processing is a system consisting of many rolls. Most of the rolls are idle rolls that just rotate held by a ball bearing and they guide the web along its path. The web is defined as the material that has its width in serveral orders of magnitude larger than its thickness. The length of web can be very long. The web material of R2R system is flexible and usually made up of metallic foils, fabric, plastic or paper. Some rolls are motorized and these are used to control the speed of web motion and the tension in the web.

During the last century, R2R systems have been used in processing of clothes, packaging, paper, graphical printing, and in metal sheet industry. Now, R2R system has found its way in printed electronics, which is the process of making electronic devices on flexible substrates. This is the future of electronic devices as the process is carried out at normal room conditions. The flexible substrate used in this system can be of plastic like polyethylene terephthalate (PET), paper or metal sheet. R2R system is simpler and cost effective method as compared to the conventional manufacturing processes currently adopted in electronic industry. R2R process comprises of selecting suitable ink, a printing system for printing the ink on the substrate like direct gravure, gravure offset, micro gravure, electrohydrodynamics, and slot die printing method and then finally curing of the ink. Figure 3-3 shows a typical R2R system schematic diagram.

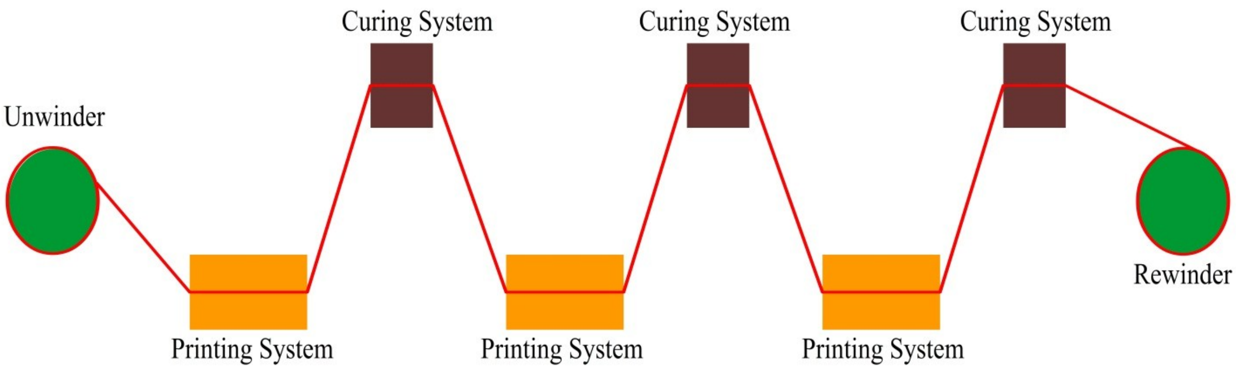

Figure 3-3: Schematic diagram of a R2R system

R2R system requires web tension control, lateral control and register control. The printing of functional materials on the substrate demands the substrate to be in a proper tension. The roughness and layer thickness defines the performance of a device (Wang et al., 2011). Lee et al. showed that the print thickness and roughness depend on the tension while keeping all other parameters constant in a R2R process (Lee et al., 2010). Hence, printed electronics require highly regulated tension in R2R process. Fluctuation in tension causes register error (Lee et al., 2009) which ultimately result in failure of the device. Graphic media uses the R2R system for printing with acceptable tension error of ± 10 per cent of reference tension in steady running state (Liu and Davison, 2003) and register control error up to 76.2 μm (Cockrell, 1946; Yoshida et al., 2008). Song and Sul presented the tension control for metal processing line (Song and Sul, 2000). For printed electronics, highly regulated tension is required as compared to graphic printing.

R2R system is a multi-input multi-output (MIMO), time variant nonlinear (NLTV) system. The roll diameter of the unwinder roll decreases whereas diameter of rewinder increases when the R2R system operates and web is moved from unwinder to rewinder. This makes R2R system a time variant system. The interactions between two spans make the system nonlinear. Disturbances of R2R system include the slip of web in NIP rolls, friction of the idle rolls, printing processes tension disturbances and backlash in the gears. R2R system is a modular machine. Many printed devices with different layer structures have to be made on R2R system. A single device may require different printing processes like gravure offset, EHD or Slot Die.

Web Tension Control

Many researchers (Chen et al., 2004; Dwivedula et al., 2006; Ebler et al., 1993; Janabi-Sharifi and Press, 2005; Kang and Lee, 2008; Lee et al., 2008; Lin, 2003; Okada and Sakamoto, 1998; Pagilla et al., 2007; Sakamoto and Fujino, n.d.; Sakamoto, 1999; Song and Sul, 2000) worked on tension control. In control theory, there are two approaches for the tension control of web. First, is mathematical modelling of the system and applying conventional control and second is the optimization or tuning regulator techniques. For mathematical modelling and conventional control, a highly precise model of the system is required. Modelling error between a system's mathematical model and the real world system, parameter variations, assumptions and the external disturbances in the practical control are the factors that have to be taken into account for highly regulated tension (Janabi-Sharifi and Press, 2005). Pagilla et al. used PI Control for a model based decentralized control with assumption that there is no slip between rolls and ignoring time variant factor of diameter of rolls (Pagilla et al., 2007). Liu and Davison described Control approaches for MIMO systems (Liu and Davison, 2003). Pagilla et al. and Kang et al. modelled the system considering it nonlinear and time variant but assumed that there is no slip between nip rolls and web materials and the idle rollers have no rotational inertia (Chen et al., 2004; Kang and Lee, 2008). Sakamoto and Fujino developed a mathematical model and performed PI control (Sakamoto and Fujino, n.d.). Ebler et al. performed a tension control comparison between load cells and dancers systems (Ebler et al., 1993). Dwivedula et al. presented a comparative study of active and passive dancers (Dwivedula et al., 2006). Lin developed an observer based tension control for friction and inertia compensation (Lin, 2003). Okada and Sakamoto simulated an adaptive fuzzy based control on a model (Okada and Sakamoto, 1998). Sakamoto estimated the interaction between different spans for tension control for a decentralized control scheme (Sakamoto, 1999). Valenzuela, et al(Valenzuela, 2003), used estimation techniques and a dancer system to control web tension in a paper-processing machine. Mcdow and Rahn (McDow and Rahn, 1998) proposed an adaptive web tension control using dancer system showing significant reduction of error. Dancer modelling and effects of active and passive dancers have been studied under different control algorithms in Refs. (Dwivedula et al., 2006; Pagilla et al., 2003).

PID control once tuned has constant parameters thus a critically damped system can go into unstable oscillation once any disturbance arises. Atherton and Majhi presented the limitations of PID controller (Atherton and Majhi, 1999). Tran and Choi (K. Choi et al., 2009; K.-H. Choi et al., 2010; Tran et al., 2011a, 2011b) used genetic algorithm to tune the back-stepping algorithm for web tension control for printed electronics. Ponniah et al. tried to reduce the tension disturbances produced by gravure offset printer using fuzzy logic (Ponniah et al., 2013). Fuzzy controller can perform better as the membership functions can be quantified in a nonlinear way by the expert opinion but fuzzy controller is a pre-tuned system which limits its capabilities. The fuzzy control is equivalent to feed forward neural networks (Li and Chen, 2000). This gives a clear advantage to back propagation artificial neural networks (BPN) over the fuzzy control scheme. Wang et al. simulated a neural networks control for tension control for a single span R2R system compared with conventional PID control (Wang et al., 2004).

The web tension of a three span R2R system is controlled by applying regularized back propagation artificial neural networks (BPN) with variable learning rate (VLR). BPN with VLR offers a MISO control system that has the ability of auto tuning. The auto tuning takes care of time variant nature of R2R system. The inputs of BPN are tension from load cells, position and speed from encoders and roll diameters measured by ultrasonic sensors. An active dancer system is integrated in printing span to enhance the printing span web tension. The coupling between spans is minimized by introducing inputs of one span to next span. The VLR BPN control is implemented on web tension control on a three span R2R system. An active dancer system is integrated in printing span to enhance the web tension control. This self-learning algorithm provides a solution to the web tension control of multispan R2R system for printed electronics.

R2R system used during the experiments is shown in Figure 3-4. This R2R system has an unwinder, infeed, outfeed and rewinder spindles connected to servomotors housed in an industrial machine frame. There are many idle rolls helping in guiding the web. Load cells are used to measure the tension in the spans. Ultrasonic sensors provide the diameter of the unwinder and rewinder rolls. An active dancer system is used. The web (PET) unwinds at unwinder and is passed through a load cell and idle rolls to the infeed comprising of first span, where span is a web length between two adjacent driven rolls. From infeed the web passes through a load cell and a lateral web control unit to gravure offset printer and from gravure offset printer through a load cell to the outfeed. The web from the outfeed passes through a load cell and a lateral web control and is rewound on the rewinder making it the last span. Figure 3-5 shows the web path through the R2R system.

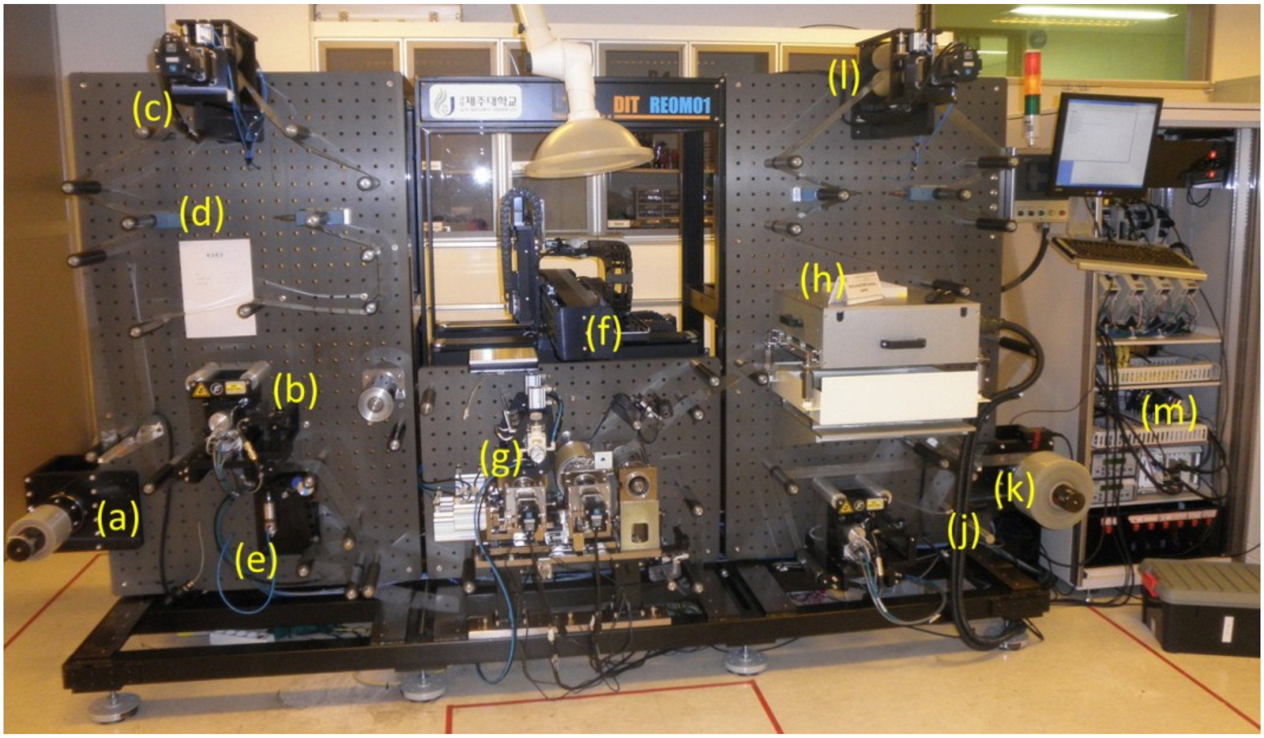

Figure 3-4: R2R system where a) unwinder, b) lateral control unit, c) infeeder, d) load cell, e) active dancer system, f) electrohydrodynamic printing system, g) gravure offset printing system, h) infrared drying system, j) ultrasonic sensor, k) rewinder l) outfeeder m) controls and drives

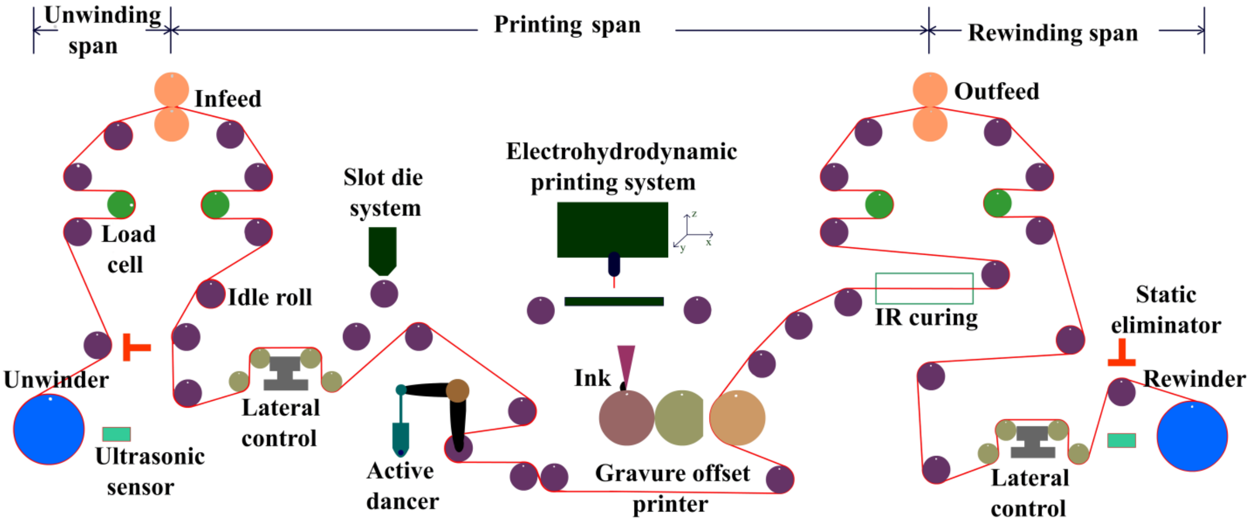

Figure 3-5: Path of web in the R2R system

PET substrate is elastic in nature so the printing was performed with low values of tension. If the printing is performed with high values of tension, it can cause shrinkage problems after its removal, which eventually causes failure of the device. The drying temperature of PET may be from 50 to 120 ^{o}C depending on the ink properties. The PET is dried in Infrared (IR) heating chamber. The temperature changes causes variations in strain, Young's Modulus and thermal coefficient in this part of the PET (Lee et al., 2008). This causes the web to surpass its yield strength and enter into the plastic region hence causing permanent failure. Ultimately, the tension was kept low at 0.56% of the yield strength, which is 5 N for the above-mentioned reasons.

A dancer system was designed to regulate tension in the web. The dancer system was integrated in the process span as shown in Figure 3-6. The dancer system was designed in an L-Shape link as shown in Figure 3-6(a). A pneumatic cylinder was the prime mover of this dancer system. The cylinder produces a proportional pressure from 0 to 800 kPa to the input voltage range which is from 0 to 10 VDC. A potentiometer was attached to know the position of dancer. The rotation of dancer on its pivot is of 5.6° which gives 2.60 V to 3.25 V signal range for the complete movement of dancer. A spring was attached to the dancer so that in the absence of applied pneumatic pressure the dancer should remain in its initial or zero position. The dancer system, components and free body diagram of dancer is shown in Figure 3-6(b) and Figure 3-6(c) respectively.

As shown in Figure 3-6(c) the spring system tends to bring the dancer system to its initial position while prime mover pneumatic cylinder moves the dancer in opposite direction. The movement in dancer system from initial position by cylinder generates potential energy in spring. By controlling the position of dancer, web tension in the process span was regulated.

The control of dancer was done in two step where in first step position of dancer is estimated which would be required to overcome web tension error using load cells and other related inputs. This estimated position of dancer was used as a pre-set to apply a position control on dancer using the position feedback by potentiometer. Hence, the web tension control was achieved by using an active dancer.

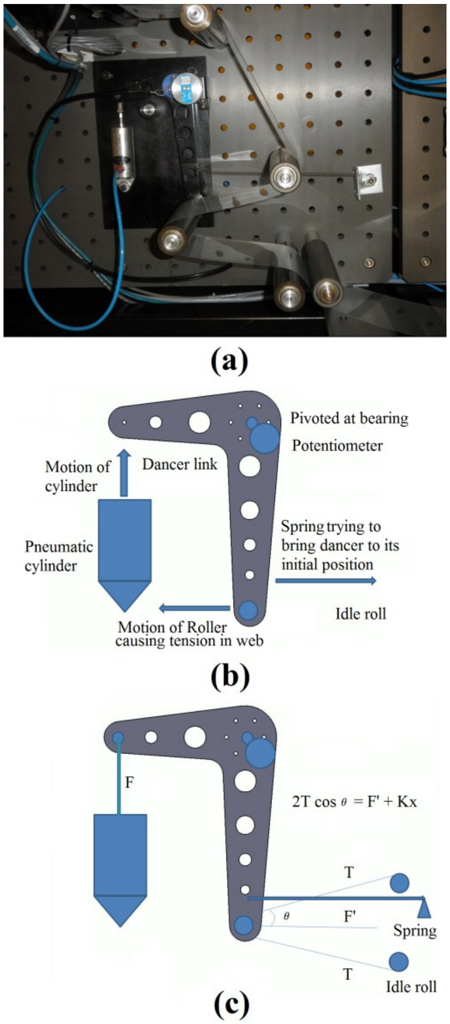

Figure 3-6: Dancer system design for R2R system a) actual hardware, b) parts of dancer system, c) free body diagram

Four Magpowr CL250 Cantilevered load cells were used to measure web tension in the spans. Two Magpowr US-2 Ultrasonic Sensors were used to measure the diameter of the unwinder and rewinder rolls. Static eliminator bar of Exair model 7009 was used to eliminate static charges. National Instrument Analog to Digital Converter Modules were used to read the values of load cells and ultrasonic sensors. The Mitsubishi servo pack MRJ-2S-70A and motors HC-KFS-73 were used. The two Lateral Control units were connected to the PXI by Profibus interface that were responsible for the lateral control of web. A high voltage power supply for electrohydrodynamic printing (EHD) was controlled by PXI via USB. The electrical circuit diagram of the system is shown in the Figure 3-7. The rotational angle and speed of AC Servomotors was calculated from the incremental encoder pulses. A field-programmable gate array (FPGA) was used to find the motion and speed of all motors. A rugged PC-based platform (PXI) processes all the data of the artificial neural network, implemented to get the appropriate torque control signals for AC Servomotors. Pneumatic cylinder used for dancer system is Fujikura BF FCS-25-26-S1. A potentiometer J50S 20K is used to know the position of the dancer. A National Instruments 16 bit analog to digital (ADC) converter was used to measure the potentiometer signal for the position of the dancer.

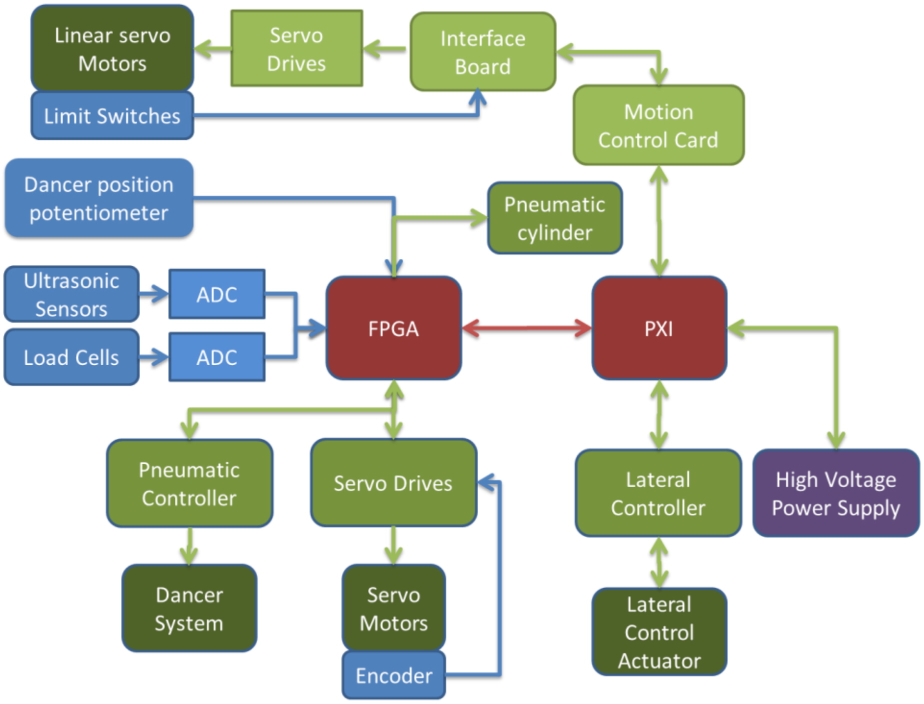

Figure 3-7: Electrical connection diagram of R2R system

National Instrument Laboratory Virtual Instrumentation Engineering Workbench (LabVIEW 8.6) was used to program the FPGA and PXI. Hardware Interfacing, code compilation, large libraries and parallel programming are the key features of LabVIEW. Multitasking in LabVIEW enables the users to make different control loops.

The web tension control was achieved by deploying artificial neural networks control algorithm. Unwinder, Outfeeder and Rewinder servomotors were made to run in tension control while the infeeder was made to run as the master velocity control of the system. The inputs of BPN of one span were used for the BPN of next span to minimize the interaction between the spans. This control scheme is shown in the Figure 3-8 where 'TA' is tension output from control to servomotor, 'VA' is the master control velocity, 'V' is the velocity of servomotor, 'E' is encoder count, 'T' is the tension measured by load cell in Newtons and 'U' is the roll diameter measured in centimetres by ultrasonic sensor. P1 is position feedback of dancer from potentiometer installed on the dancer system. PS is the estimated position of dancer by neural networks. PR1 is the position control single to the pneumatic cylinder. The speed of the web is controlled by the master velocity control motor. All other motors were set to match the speed while keeping the web at the prescribed tension of 5 N.

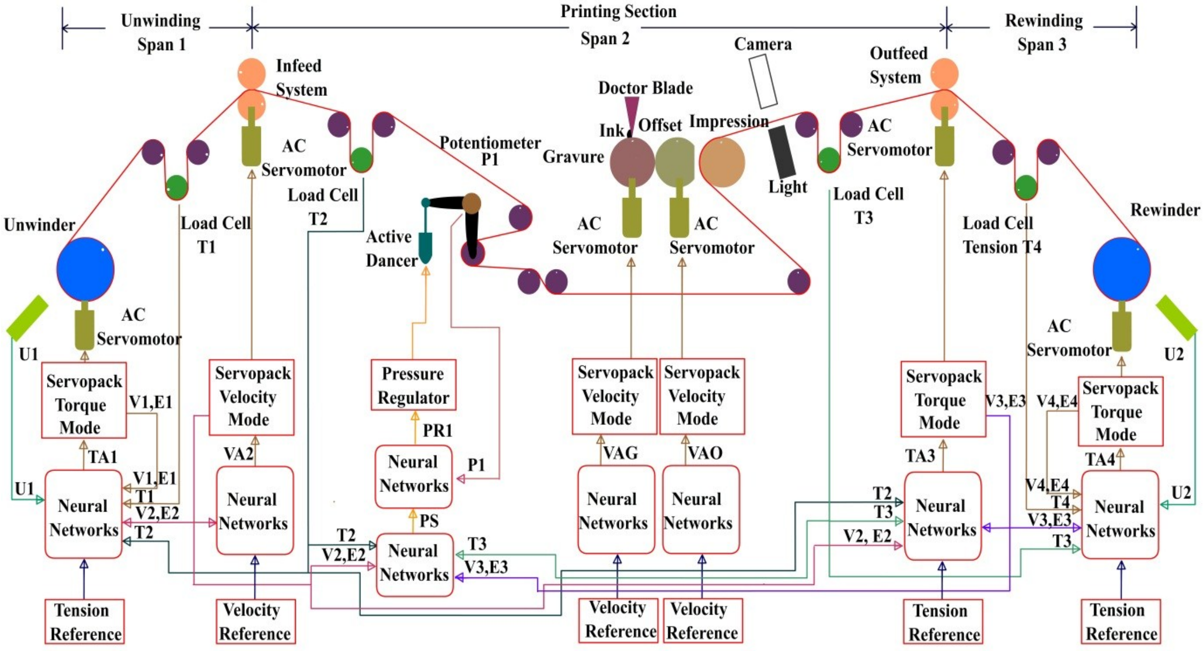

Figure 3-8: Control schematic diagram of R2R system

Artificial neural network can also be called as neural network (NN). NN are nonlinear and adaptive systems, hence NN can take care of the disturbances and time variant characteristics of the R2R system. NN consists of networks of artificial neurons in which the data flows through and their weights are changed to reduce the root mean square of error during the learning phase. A single neuron is presented in Figure 3-9 in which the inputs are multiplied by the weights, the product is added to bias and resultant is subjected to activation function where an activation function is the mathematical formulation that is used to calculate the output of a neuron.

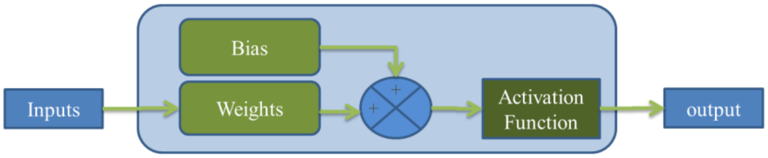

Figure 3-9: Structure of a single neuron

The input of NN is scaled to be within 0.1 to 0.9 to get the maximum efficiency of back propagation method. NN is designed in layers. First layer is called the input layer and last is called the output layer. In-between layers are termed as the hidden layers. Figure 3-10 shows the layers of a NN. A single neuron in a layer is also called a node. Its output is given by equation

$$a_j^{(l)} = f\left(W_j^{(l-1)} a_j^{(l-1)} + b_j^l\right) \tag{3-1}$$

Where 'f' is the activation function, '$W_j^{(l-1)}$' are the weights, 'b_j^l' is bias, '$a_j^{(l-1)}$' is the input of neuron 'j' of layer 'l'.

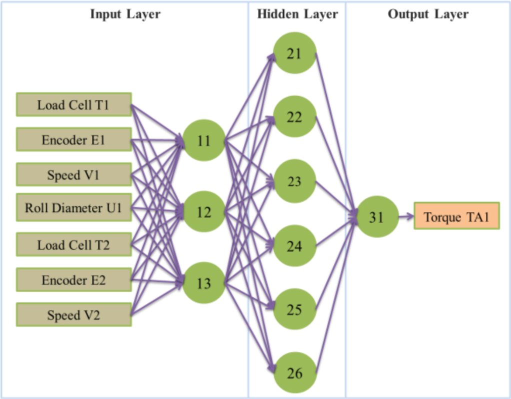

Figure 3-10: Neural networks layer architecture

For R2R system the inputs of the NN control are the feedback from load cells, roll diameter at the winder and unwinder, position from encoder pulses of servomotors and velocity of servomotors calculated from the encoder counts. The position from encoder counts, velocity calculation of the motors and load cells calibration was performed in FPGA. For first layer with input 'x' the output becomes

$$a_j^{(1)} = f\left(W_j^{(1)}x + b^1\right) \tag{3-2}$$

Same activation function must be used on all nodes in a layer but different activation functions can be used for different layers. Sigmoid activation function was employed in this system. Sigmoid activation function is a nonlinear function as shown in equation (2-3). A non-linear activation function allows the network to compensate for the non-linearity present within the system (Li and Chen, 2000).

$$f(x) = \frac{1}{1 + e^{-x}} \tag{3-3}$$

The derivative of equation (2.3) is as follows

$$\frac{d}{dt} f(x) = f'(x) = f(x).(1 - f(x)) \tag{3-4}$$

'z^l' is the intermediate value in a neuron before the activation function is applied. So for the first layer 'z^l' is described by the following equation

$$z^{(1)} = W^{(1)}x + b^1 \tag{3-5}$$

When the activation function is applied then the output of the neuron is readily available and is given as equation (2)

$$a_j^{(1)} = f\left(z^{(1)}\right) \tag{3-6}$$

In Feedforward neural networks the data flow is one directional that is from the input layer to next layers so the process completes at the output layer. There is no loop or feedback of data flow. A well-tuned feedforward system acts like a fuzzy system (Li and Chen, 2000) and can handle non-linear systems as well but as the weights of the system remains constant, for a time variant system the weights working for one instant may not perform well under other. For a three layer NN, as presented in Figure 3-10, the output of first layer is given by equation (3-6). Following the same sequence, the output at last layer i.e. 3rd layer is stated as

$$a_j^{(3)} = f\left(z^{(3)}\right) \tag{3-7}$$

The output equation for feedforward neural networks shown equation (3-8) can be expanded into

$$a_j^{(3)} = f^3\left(W^{(3)} f^2\left(W^{(2)} f^1\left(W^{(1)} x + b^1\right) + b^2\right) + b^3\right) \tag{3-8}$$

A Backpropagation neural network (BPN) is the method of feedback system or loop in NN. This process (Werbos, 1990) has two steps, the first step calculates the error from the desired output to the actual output and then keeps on calculating the error for each neuron in the NN and the second step updates the weights for all the neuron according to that error. The BPN scheme is shown in Figure 3-11.

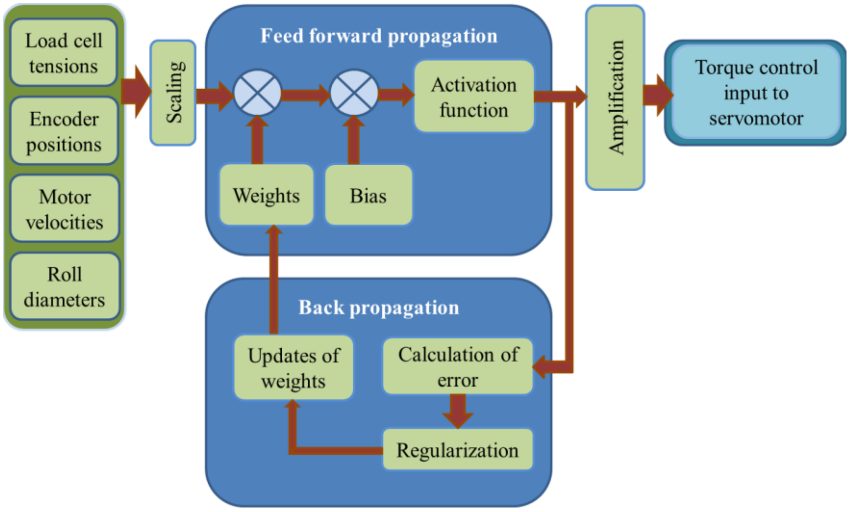

Figure 3-11: Neural network programming design

Calculation of error starts from the difference between the desired output value of the system from training set 'y_j' and the value of output layer 'a_j^l'. The error is represented by '$\delta_j^{(l)}$' where 'δ' is the error in layer 'l' and at neuron (node) 'j'

For the NN shown in Figure 2-6, the error 'δ_j^3' of output layer is

$$\delta_j^{(3)} = y_j - a_j^{(3)} \tag{3-9}$$

After the output layer the error is calculated back from output layer to input layer, layer by layer, thus the error is propagating back from last layer to the first layer.

$$\delta_j^{(l)} = \left(W^{(l)}\right)\delta^{(l)} * f'\left(z^{(l)}\right) \tag{3-10}$$

$$f'\left(z^{(l)}\right) \;= a_j^{(l)} * \left(1 - a_j^{(l)}\right) \tag{3-11}$$

$$\delta_j^{(l)} = \left(W^{(l)}\right)\delta^{(l)} * a_j^{(l)} * \left(1 - a_j^{(l)}\right) \tag{3-12}$$

The error in second and first layer for NN in Figure 3-10 is given in equation (3-13) and (3-14) respectively.

$$\delta_j^{(2)} = \left(W^{(2)}\right)\delta^{(3)} * a_j^{(2)} * \left(1 - a_j^{(2)}\right) \tag{3-13}$$

$$\delta_j^{(1)} = \left(W^{(1)}\right)\delta^{(2)} * a_j^{(1)} * \left(1 - a_j^{(1)}\right) \tag{3-14}$$

Training is the process of updating weights. Initially the system is started by random values of weights and bias values between 0 and 1. With BPN the weights are auto tuned which makes BPN capable of dealing with time variant nature of any system. After each feedforward networks output, error value for each neuron is calculated. These error values are used to update the weights so the root mean square error is minimized.

$$W_{New}^{(l)} = W^{(l)} + \alpha\left(a_j^{l-1}\delta_j^{(l)}\right) \tag{3-15}$$

Here '$\delta_j^{(l)}$' is Error and 'α' is learning rate which is the ratio effecting the speed and quality of learning. After first cycle of tuning, all weights are updated so that for the next tuning the system can start with weights closer to the actual converging weights (Lari-Najafi et al., 1989) instead of random values.

Constant learning rate consumes more training cycles. In addition, the constant learning rate has to be optimized because if the learning rate is high the system may oscillate and become unstable while a low learning rate causes may cause the system to converge after a long time thereby increasing the rise time.

For decreasing the rise time a variable learning rate (VLR) approach (Amini, 2008) is adopted. The learning rate is proportional to the error between the user prescribed value and the system output. When the error is large the learning rate is higher than optimum value so that the system can train itself faster but for a smaller error the learning rate stays at the optimum value. The learning rate 'α' is presented as:

$$\alpha = \begin{cases} 0, & -b \ge E \ge b \\ \alpha_{opt}, & -c \ge E \ge -b \\ & b \ge E \ge c \\ \left|\alpha_{opt} \times E\right|, & -d \ge E \ge -c \\ & c \ge E \ge d \\ \alpha_{Max}, & otherwise \end{cases} \qquad (3\text{-}16)$$

Where E is the error, 'α_{opt}' is optimized learning rate, 'α_{Max}' is maximum limit for learning rate and error margin ranges b, c and d are shown in Figure 3-12.

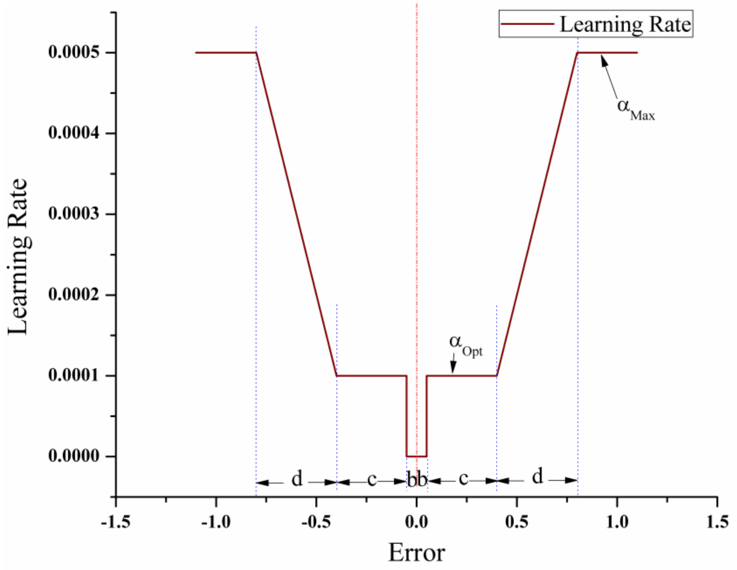

Figure 3-12: Limits set on variable learning rate corresponding to error

R2R has a complex system model and in initial training BPN tries to memorize the data rather than learning from the trend. This makes the system to perform well on training data but on unseen data, the system will have poor predictive performance. This state is known as overfitting. As a remedy, limits are applied for the training of system so that after getting a suitable accuracy the training procedure stops. Regularization term has been added to overcome the overfitting problem. So with regularization term the weight update equation become

$$W_{New}^{(l)} = W^{(l)} + \alpha\left(a_j^{l-1}\delta_j^{(l)}\right) + \lambda W^{(l)} \tag{3-17}$$

Where 'λ' is the regularization parameter which is a penalty on the weights and hence keeps the NN out of over fitting.

Different configurations of neural networks layer structures were used to control R2R system. Final configuration is shown in Figure 3-10, which has three layers. First layer has three neurons and seven inputs. Second layer has six neurons and last layer has one neuron. Regularized VLR BPN is applied on the R2R system for tension and velocity control in a fashion described in Figure 3-11. Experimental Parameters for R2R system control using regularized variable learning rate backpropagation neural networks are shown in Table 3-1.

Table 3-1: Experimental Parameters for R2R system control using regularized variable learning rate backpropagation neural networks

Parameter	**Value**
Web Width	120 mm
Web Thickness	0.5 mm
Reference Tension	5 N
Master Control Speed	2.4 m/min
Optimized Learning Rate	1E -4
Optimized Regularization Rate	1E -4
Learning Rate Error Margins	± 0.05
Maximum Learning Rate	1E -3
Diameter of Infeed Roll	80 mm
Control loop time	1 ms

Step response study is a universal method to compare different control systems, it provides data such as overshoot, undershoot, settling time etc. The steps of 5, 10, 15 N tension were chosen because 5 N is the minimum possible tension on the machine and step sizes smaller than 5N did not produce significant difference between the response of the two control systems (i.e. PID and BPN). The tension changes in static mode form 5 N to 10 N, 15 N and back in BPN control are shown in Figure 3-13 and Figure 3-14 shows the PID tension control with step response in static mode form 5 to 10 and 15 N and back.

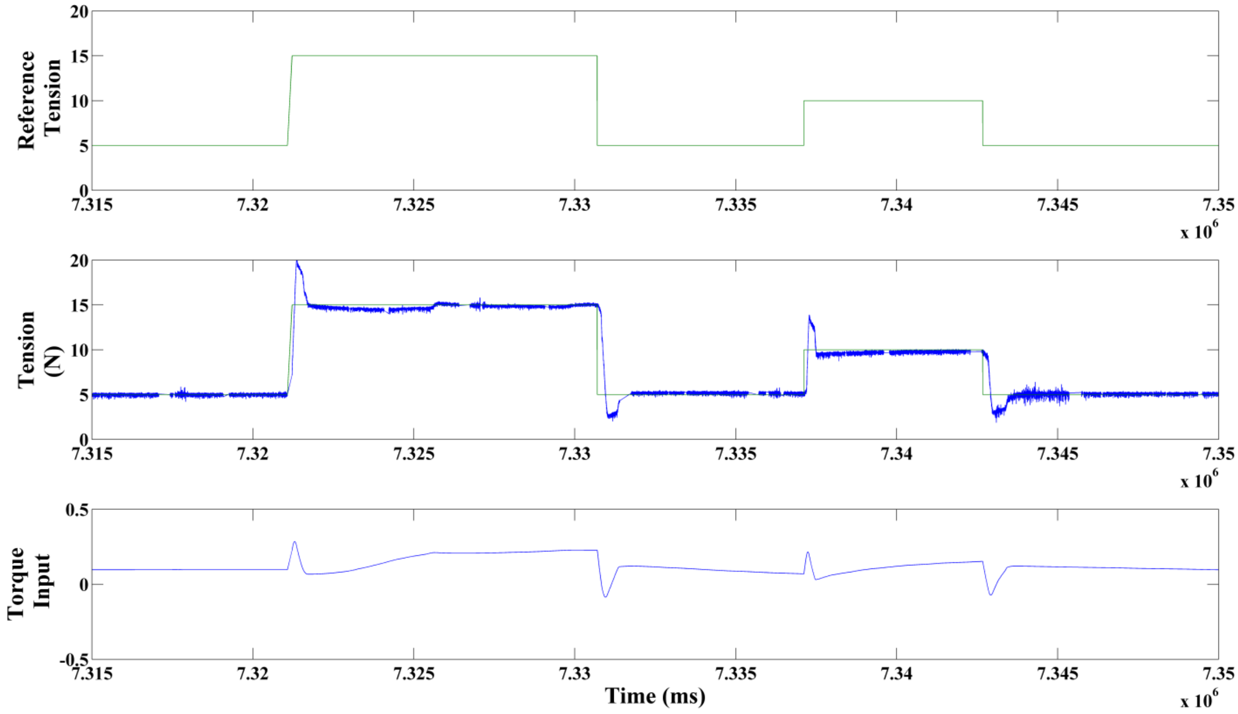

Figure 3-13: BPN web tension control of R2R system where reference tension is changed from 5 N to 10, 15 N and back in static mode

In dynamic mode where the master velocity control of the system is set at 2.4 m/min tension changes from 5 to 10 N, 15 N and back controlled by BPN are presented in Figure 3-15. A step response change in master velocity control of R2R system is shown in Figure 3-16. Here the speed of system was varied from 0.72 m/min to 1.2 m/min in a step form. The tension was kept constant at 5 N.

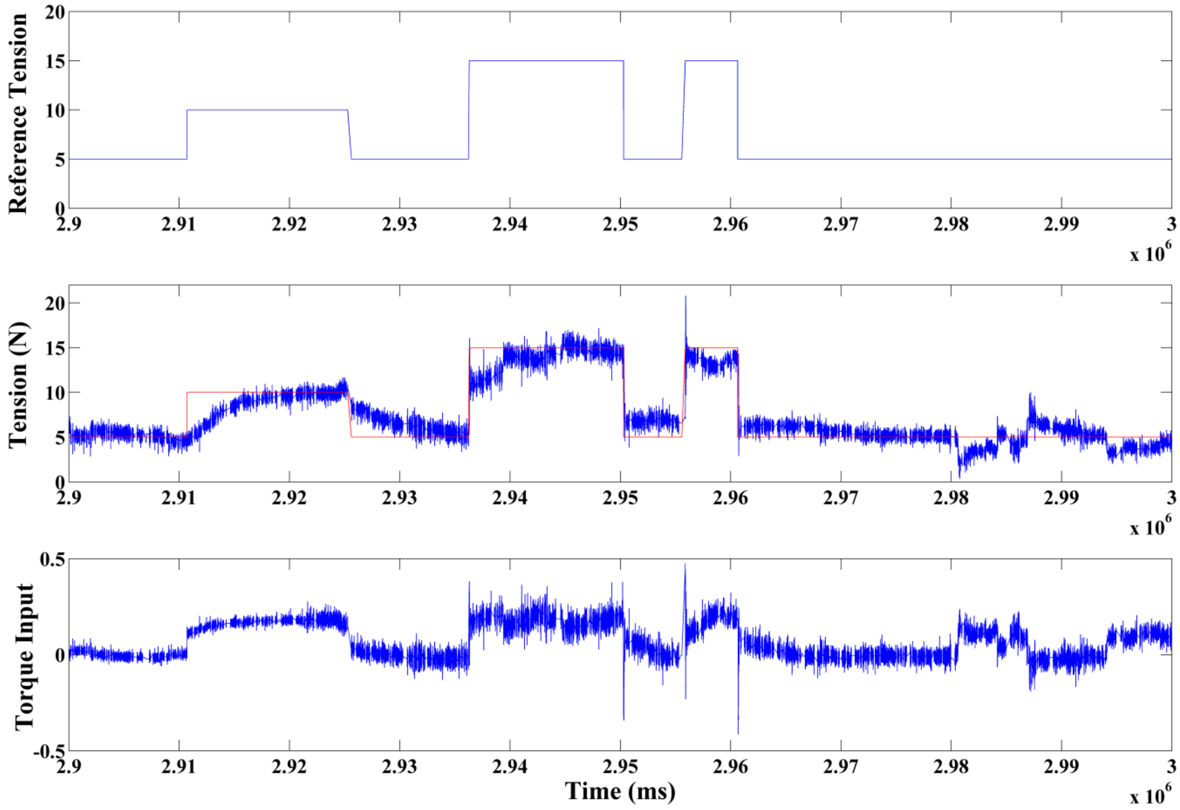

Figure 3-14: PID web tension control of R2R system where reference tension is changed from 5 N to 10, 15 N and back in static mode

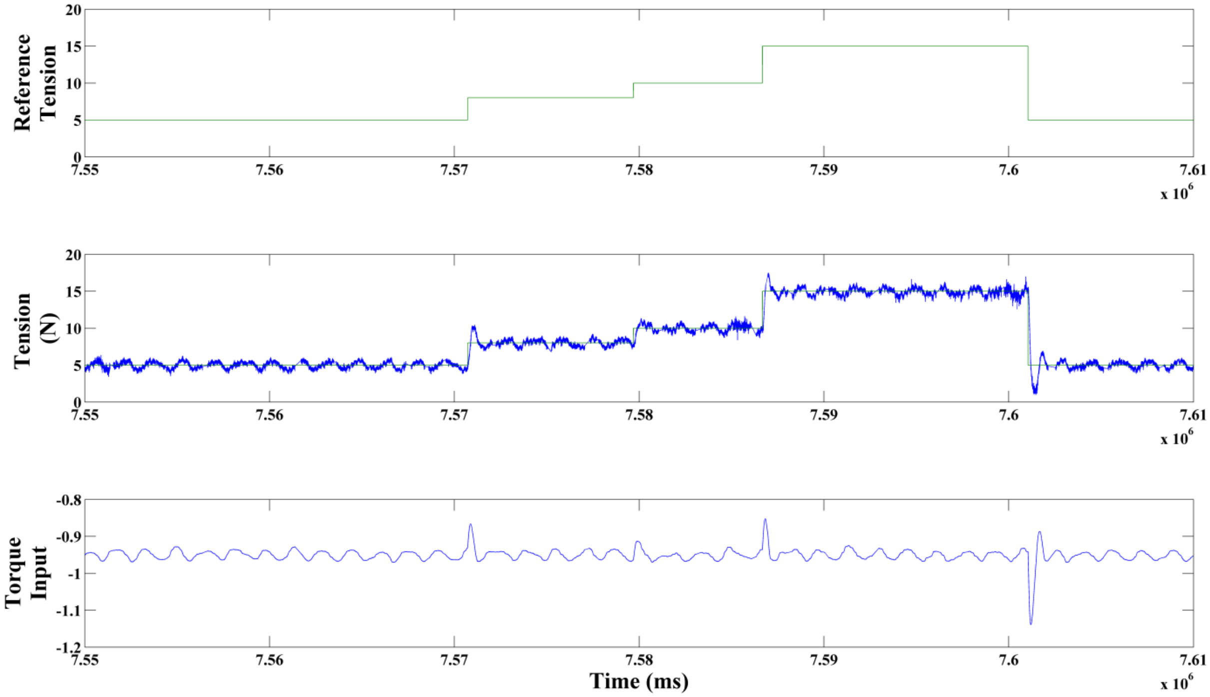

Figure 3-15: BPN web tension control of R2R system where reference tension is changed from 5 N to 10, 15 N and back in dynamic mode with master velocity control set at 2.4 m/min

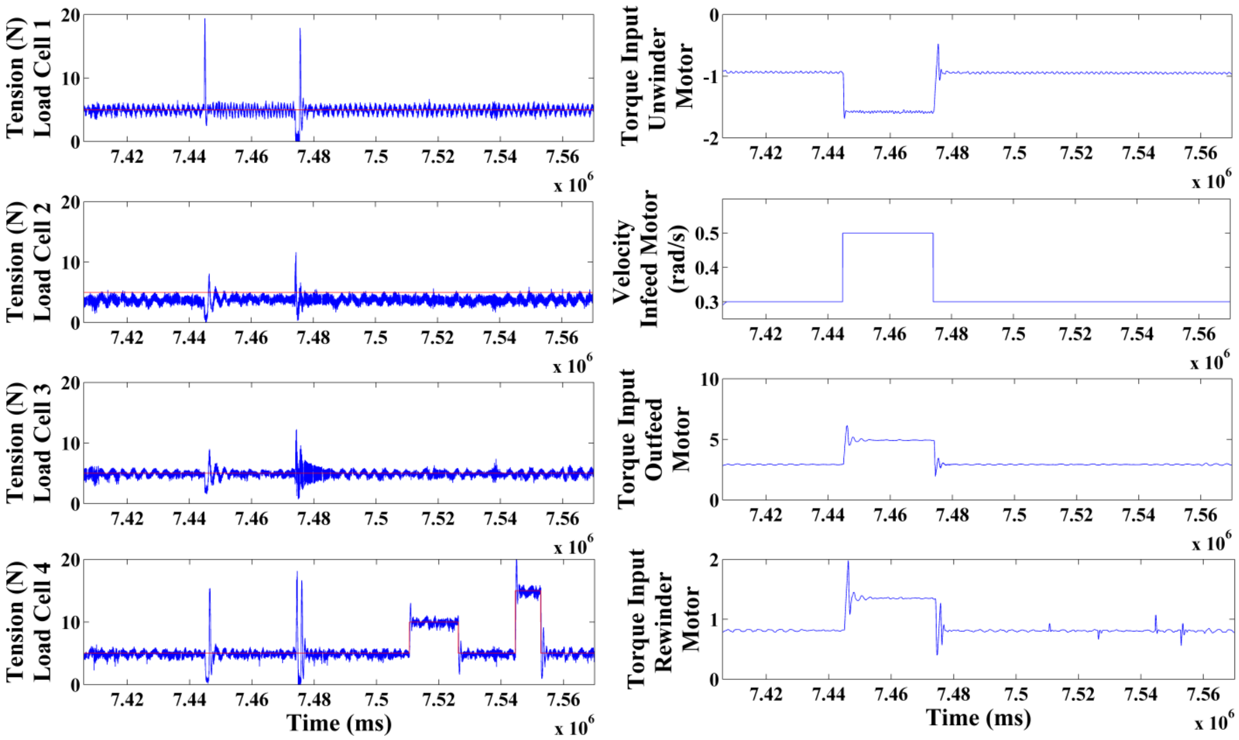

Figure 3-16: BPN web tension control of R2R system where speed of system is changed form 0.72 m/min to 1.2 m/min in a step form

The position control is very important aspect for a dancer system control. Position control of dancer was achieved where dancer is moved from 0° to 5.6° by feedback from potentiometer in range of 2.60 V to 3.25 V. The position control of dancer system using regularized backpropagation neural networks is shown in Figure 3-17.

The PID response in second span was much better than first and third span as in second span the time variant nature of R2R system does not come into play as shown in Figure 3-18. The time variant behaviour of R2R system is shown in Figure 3-19 where the changing diameters of unwind and rewind rolls give a corresponding change in BPN outputs to cater for the changing roll diameters of rewind and unwind rolls. Here it can be seen that in second span, the torque for the outfeed motor remains the same, as it has no effect of changing roll diameters.

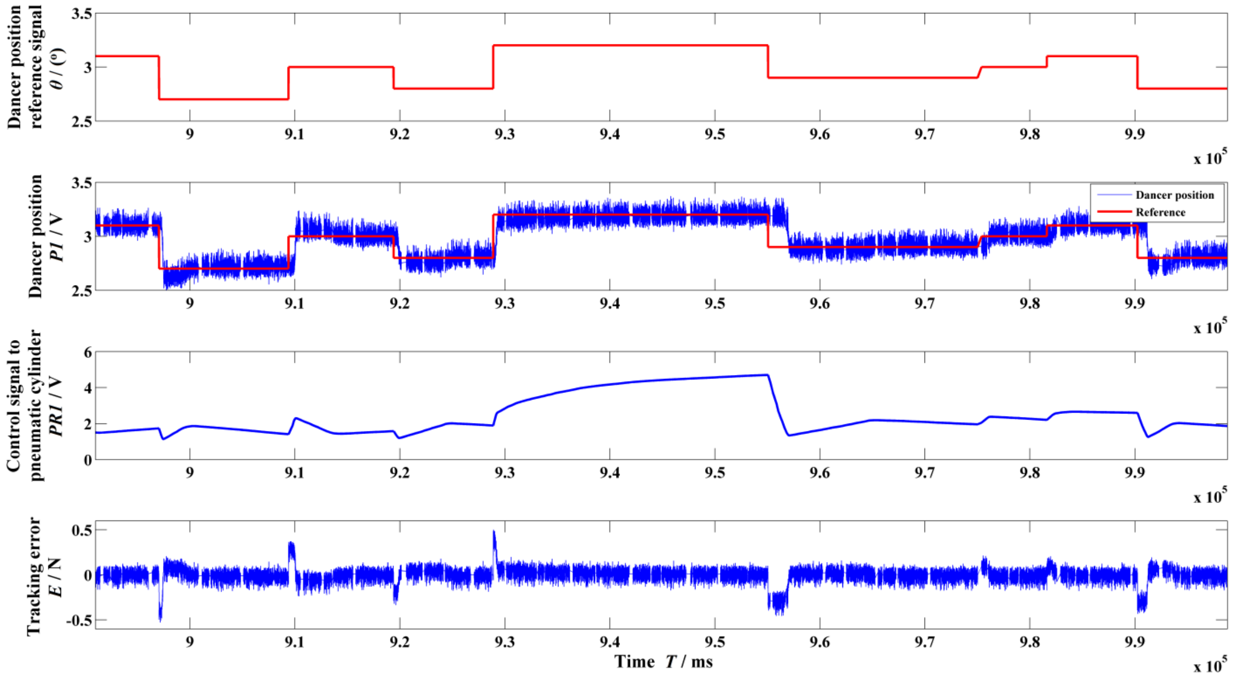

Figure 3-17: Position control in dancer system

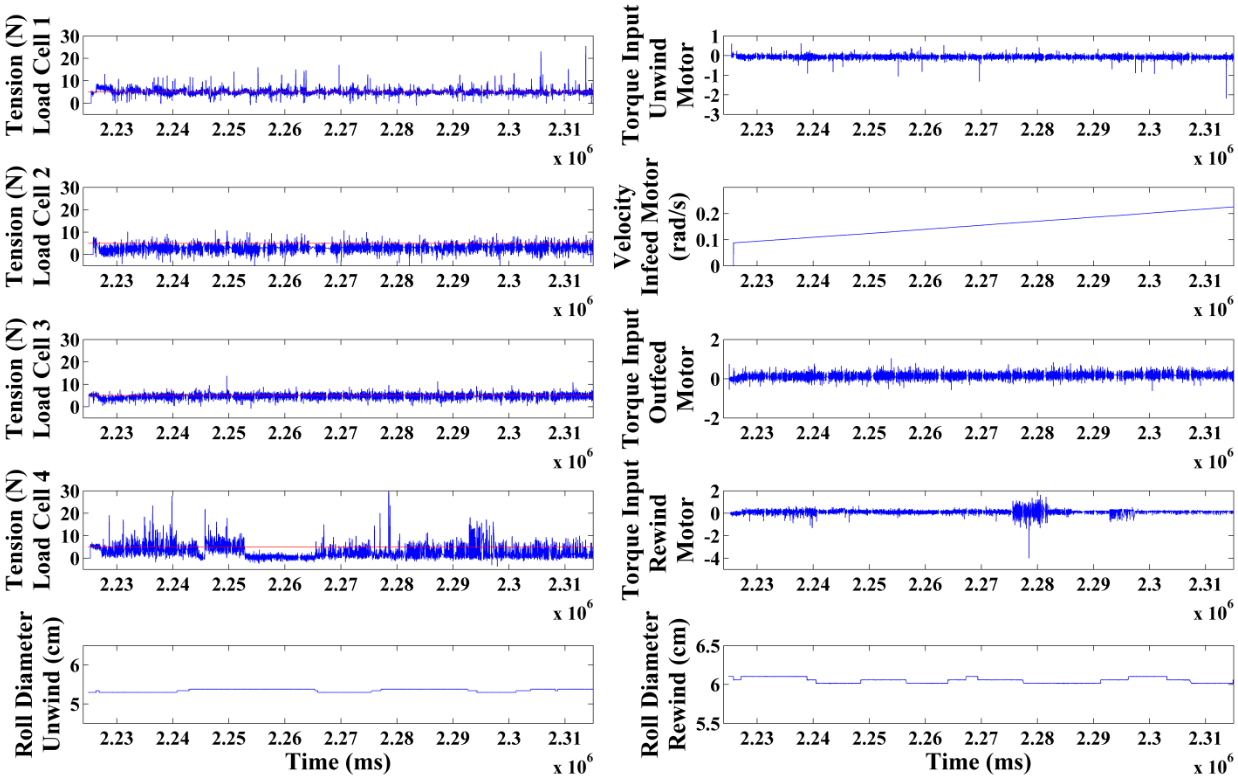

Figure 3-18: PID web tension control of R2R system where reference tension is 5 N and master velocity control of system is increasing

When PID control is compared to BPN control in step response of tension changes, BPN offers better compensations to step responses of tension from 5 to 10 N and 15 N as shown in Figures 3-13 and 3-14. If the sensitivity of PID is increased in this static mode than PID control goes in oscillation in dynamic mode. BPN is offering a good sensitivity in static mode without going into oscillation in dynamic mode as shown in Figure 3-15 and 3-16. In order to make the system sensitive for controlling web tension at a low value of 5 N, a high learning rate has been used in VLR BPN. The use of the high learning rate is the main cause of the spikes in initial tension during step changes.

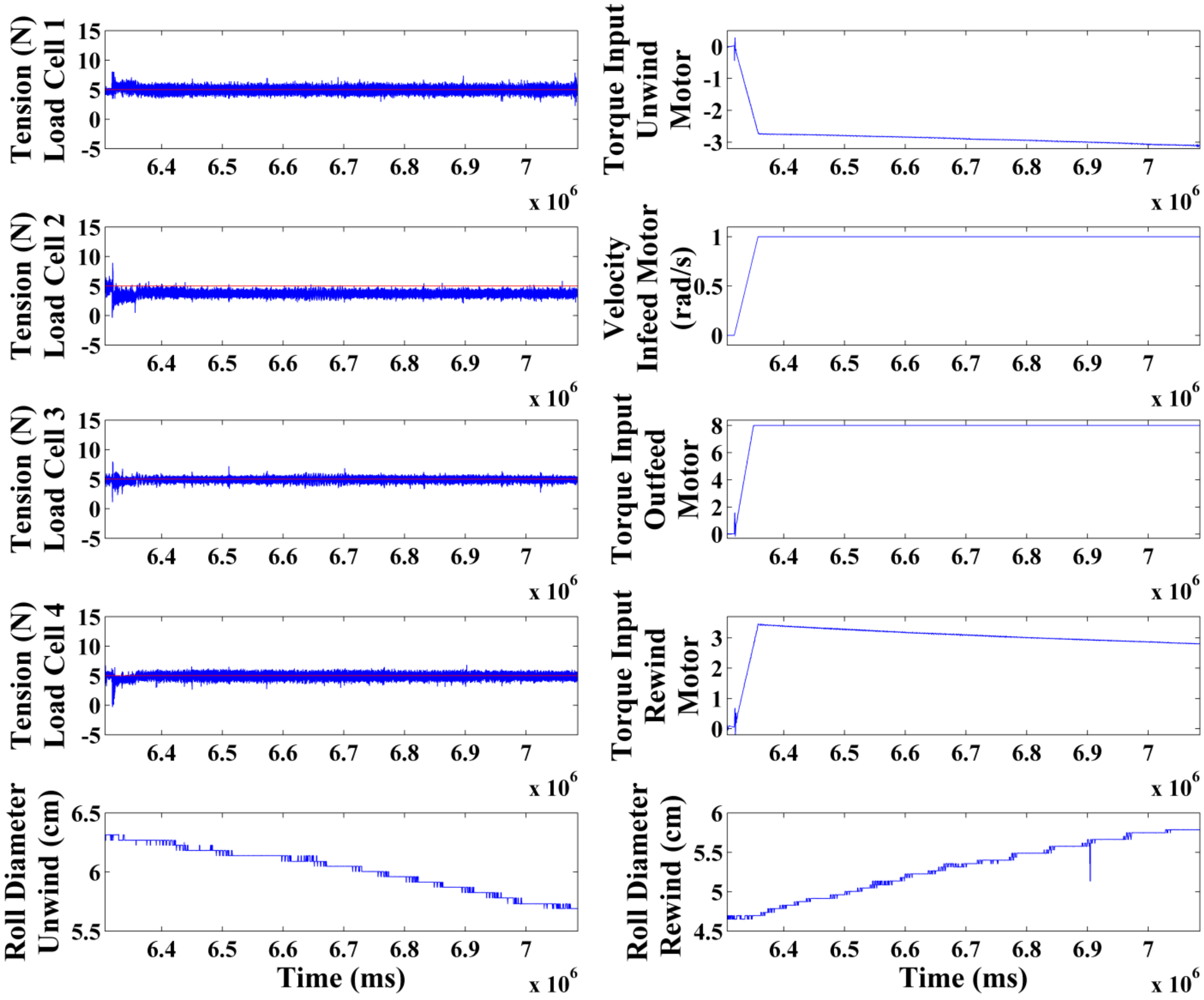

Figure 3-19: R2R system with master velocity control increasing from 0 to 2.4 m/min using BPN control scheme. The changing roll diameter causes the corresponding change in the torque input of the unwind and rewind motors is shown where dancer system is not active

Web tension controlled by PID control is shown in Figure 3-18. Here PID seems to be seen struggling to maintain the tension control on a very low value of 5 N tension. There are many spikes of more than 10 N. These figures show that BPN offers better control with multi-inputs and online tuning as compared to conventional PID control.

In steady state form the second load cell (T2) show web tension around 3.7 N on a system where dancer system is not active as shown in Figure 3-19. To enhance this web tension dancer system was activated. Figure 3-20 shows the web tension control with the active dancer. Figure 3-21 shows the input output of the dancer.

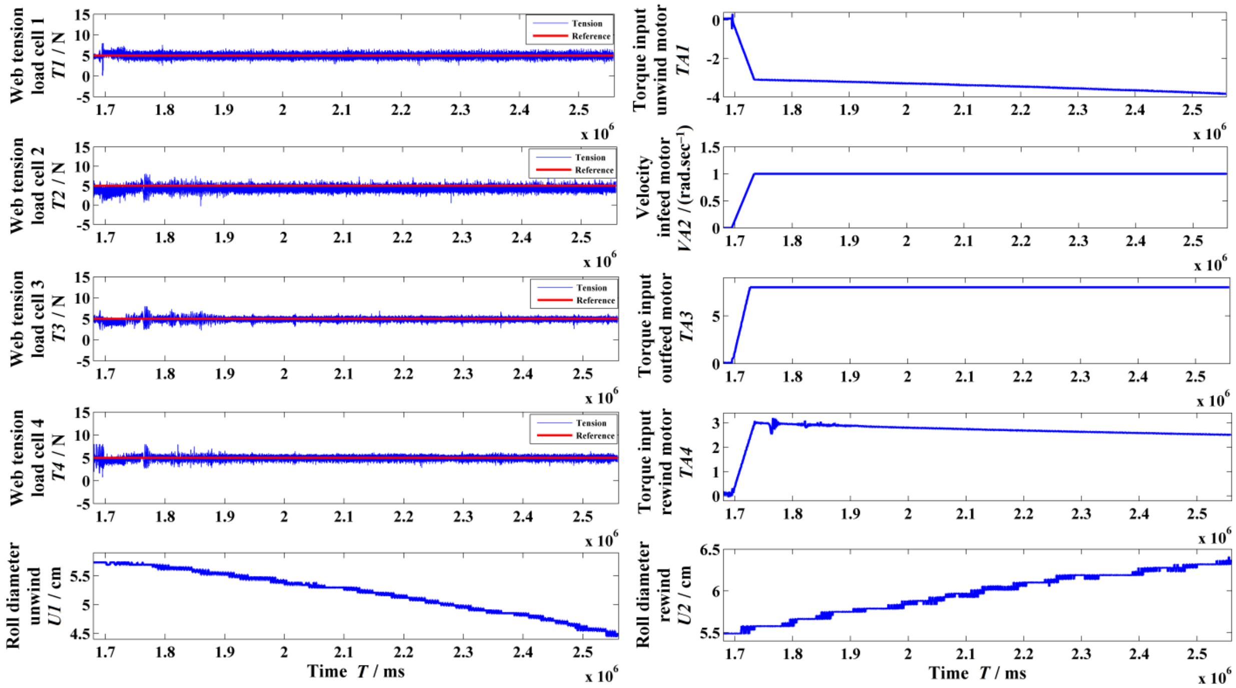

Figure 3-20: Web tension control of R2R system with active dancer system

Comparison of Figure 3-19 and 3-20 shows that in second span, in load cell 2, the web tension was improved from 3.75 N to 4.75 N. The web tension regulations under change of master speed control form 0 to 2.4 m/min. The overshoot was less than ±2.5 N and steady state error was within ±1 N where load cells have a signal noise of ±0.7 N. Overall control loop cycle was less than 1 millisecond.

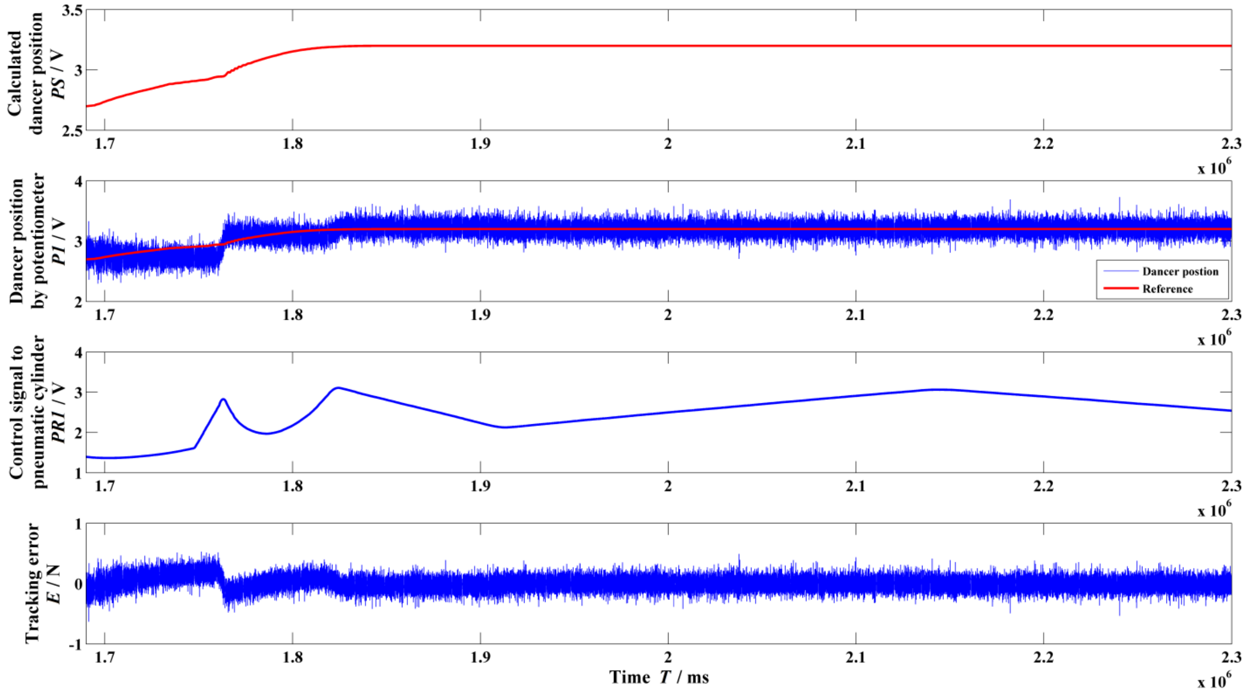

Figure 3-21: Input output of dancer system during integrated web tension control of R2R system

Web tension control of a multispan R2R system for printed electronics is achieved by applying regularized VLR on BPN. An optimum neural network layer scheme for this task has been found which has three layers and ten neurons. The BPN has MIMO interface, nonlinear activation functions and auto tuning scheme. The MIMO system is controlled by decentralized MISO scheme. The nonlinearity of interaction of spans is minimized with introducing multiple inputs from the corresponding interacting spans and nonlinear activation functions. The auto tuning of weights cater for the time variant nature of the system. The steady state error of second span is within +1 N where the load cells noise is +0.7 N. The introduction of dancer system helped in the enhancement of web tension in second span. Hybrid system of active dancer and load cells used for accurate web tension control in process span web tension regulation of ± 1 N is achieved. Nonlinear R2R system is catered by nonlinear activation functions and training of neural network. The system has rise-time of 150 ms and settling time of 0.5 s. Highly regulated web tension provides a base for registration control in printed electronics. The experimental result of regularized variable learning rate using backpropagation neural networks control scheme gives fast auto tuning while avoid system instability hence giving a solution for a R2R system for printed electronics.

3.2.2 Electrohydrodynamics Printing System

In electronics industry, lines and pattern of selected materials are required for device fabrication. The conventional electronics manufacturing systems based on lithography are quite complicated. They are time consuming and require long series of steps like masking, etching, electroplating etc. All of these steps depend on control of temperature and pressure yet these processes are not so efficient in material utilization. The throughput limitations, lack of continuous processing, rigid substrates and use of corrosive chemicals make the conventional electronic devices fabrication techniques expensive (Choi et al., 2011). Printed electronics has shown potential to be effective and economical in recent years through the commercial systems like thermal and piezoelectric inkjet printers. Inkjet printers are scalable for batch and large scale processing and provide flexibility to print any kind of pattern in a plane without wasting the expensive material, ink. The ink is pushed electrostatically or pneumatically through the nozzle to form a pattern also called a print. Commercial inkjet printers however had their share of problems, e.g. low ejection frequencies, limited applicable viscosities, thermal problems, nozzle clogging, nozzle size, and inability to make a smaller drop than their nozzle diameter (Kim et al., 2012). Electrohydrodynamic (EHD) printing is achieved by pulling out functional ink from the nozzle and use of electric field to overcome the liquid surface tension. Therefore, this pulling of ink is in contrast to previous inkjet printer designs where ink is pushed out. EHD printing is one-step device printing technique with capacity to process a broad range of solution-based materials in terms of viscosity and conductivity. EHD is performed under ambient temperature and pressure conditions (A. Khan et al., 2011) and provides more throughput and speed than other inkjet techniques (Pikul et al., 2011). EHD printing is useful in many applications (Yang and Rida, 2007) and has created newer opportunities by printing biological materials (K. Kim et al., 2010). EHD printing can be performed in continuous (Khan et al., 2012; Rahman et al., 2012b) and drop-on-demand (DOD) (D. S. Kim et al., 2011; Lee et al., 2012; Mishra et al., 2010; Rahman et al., 2012a, 2011) approach.

An electronic device may comprise of many layers of thin films and patterns. Inkjet printer or gravure offset printer can print patterns while micro gravure, slot die can make thin films. The electrohydrodynamic printing system can print patterns as well as it can make thin films (Duraisamy et al., 2013, 2012a) by atomization (ESD) of charged droplets. Multiple passes, solution concentration, solvent and standoff distance can easily control the thickness of thin films.

Here in this work, electrohydrodynamics was used to spray for the fabrication of thin films so the EHD will not be discussed in detail although the setup and phenomena of both ESD and EHD are the same. The major difference between spray and printing is the standoff distance. In case of printing the standoff distance is small, while for spray its more larger. The setup used for ESD spray was developed in lab as shown in Figure 1-7. A metallic nozzle with internal diameter of 110 μm was attached to the EHD head (K. H. Choi et al., 2009). This head was attached to a head-holder that could move along all three axes. The linear servomotors of head-holder were controlled by LabVIEW program. This program was made to move head-holder using coordinate points stored in a text file in lines and arcs. NI motion controller (NI-PXI-7340) was placed in PXI (NI-PXI-8110). The motion controller card used CW7764YS3 as interfacing board. The head was connected to variable air pressure pump through a Teflon tube. The flow of ink through the nozzle was optimized by controlling the pressure. Functional ink was injected in the head by the help of a syringe. A function generator (Hewlett Packard 33120A, 15 MHz) was connected to an oscilloscope (Hewlett Packard 54602B, 150 MHz) and high voltage power supply (TREK 610E) which can supply up to 10 kV. This high voltage source was connected to the nozzle and stage was grounded. A high-speed camera (Sony XC-HR50) was connected to a computer to observe the EHD phenomena at the meniscus. A light source (IDT LED1) was placed across nozzle for lighting purposes.

This EHD system was installed on a R2R system to make devices at a mass scale as shown in Figure 3-4 where unwinder, infeeder, lateral control unit, dancer system, gravure offset printer, pressure pump, EHD system, high speed camera, oscilloscope, high voltage amplifier, function generator, infrared drier, outfeeder, unwinder, PXI, and motor drives are shown. The path of the web is shown in Figure 3-22. The electrical connections of sensors and actuators of R2R system with the controlling FPGA and PXI are shown in Figure 3-7. The control schematic diagram showing the web tension control by regularized variable learning rate back propagation artificial neural networks is shown in Figure 3-23. The tension control of R2R system was described Section 3.2.1. In EHD printing, the R2R system was working in a sequence that after each print the web moved and made space on PET substrate for a new print. The time scheme of moving substrate and EHD printing on R2R system are shown in Figure 3-24 where; T_r is the uniform acceleration time, T_m is the uniform velocity time and T_f is the uniform deceleration time for PET movement at 5 N web tension control. The printing time T_p is the time, when EHD printing is performed on static PET under effect of web tension of 5 N. These times and web speed were translated into microns in the main program for spray of inks.

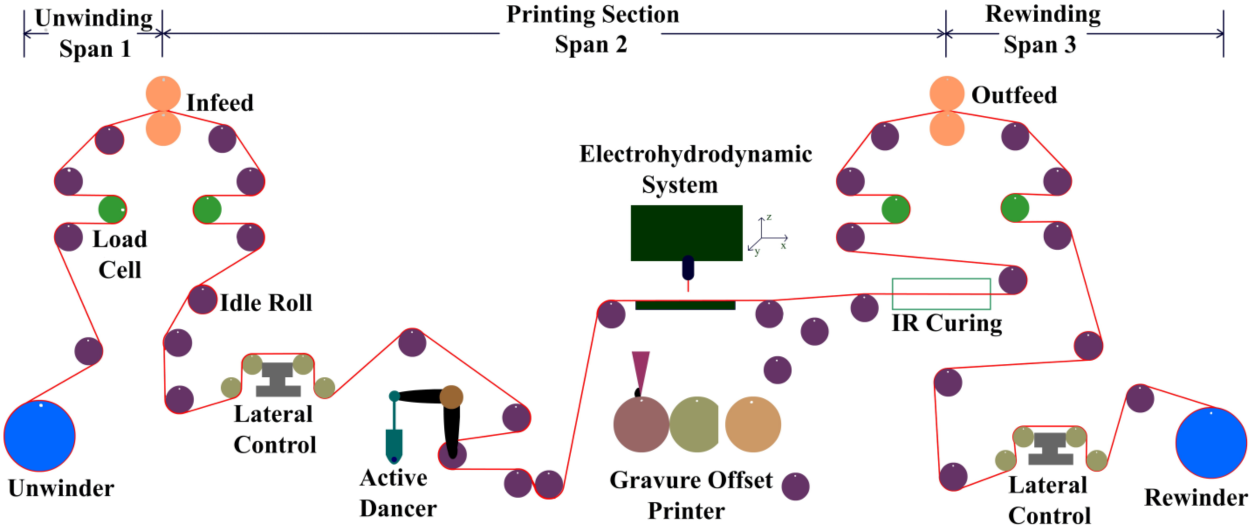

Figure 3-22: Web path on R2R system for printing by electrohydrodynamics system

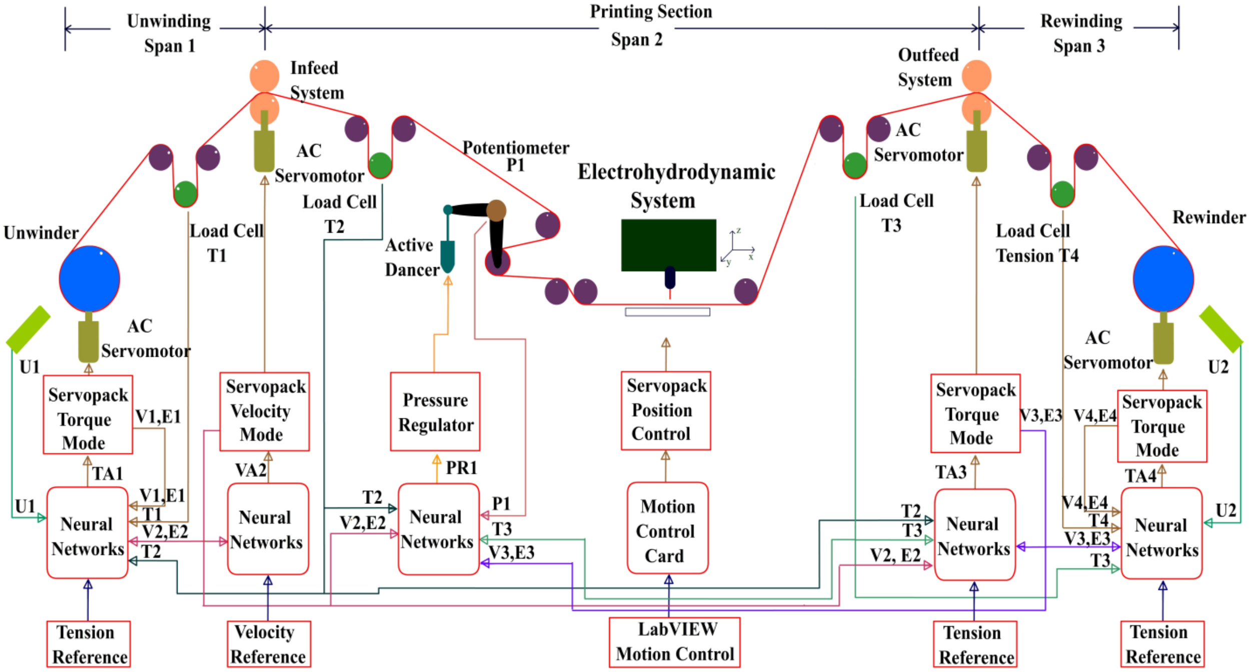

Figure 3-23: Control schematic diagram for R2R system with electrohydrodynamic printing system

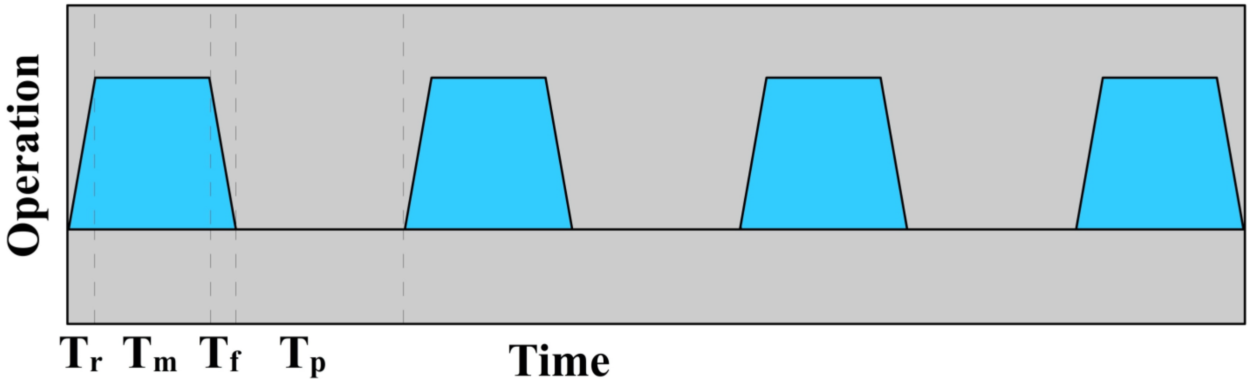

Figure 3-24: Timing diagram for printing and motion on a R2R system

At initial flow rate, drops of larger diameter than the nozzle orifice were generated where this phenomena is known as dripping mode in electrohydrodynamics. When a DC voltage was applied the frequency of generation of these drops increased while their size decreased. The size of droplets decreased proportionally with flow rate. The generation of these droplets is called micro dripping. Further increase in voltage resulted in the spindle mode in which meniscus was broken in larger droplet with satellite droplet known as unstable cone jet. After unstable cone jet mode, further increase of voltage brought the meniscus in the stable cone jet mode. The flow rate, electric field and nozzle diameter of setup while conductivity, viscosity and surface tension of ink were the important operating parameters of electrohydrodynamics phenomena as explained in previous work (Choi et al., 2011). Figure 3-25 accounts for the different modes of electrohydrodynamics phenomena. As electrohydrodynamics pulled the ink instead of pushing, unlike inkjet printer, so it produced patterns of smaller sizes.

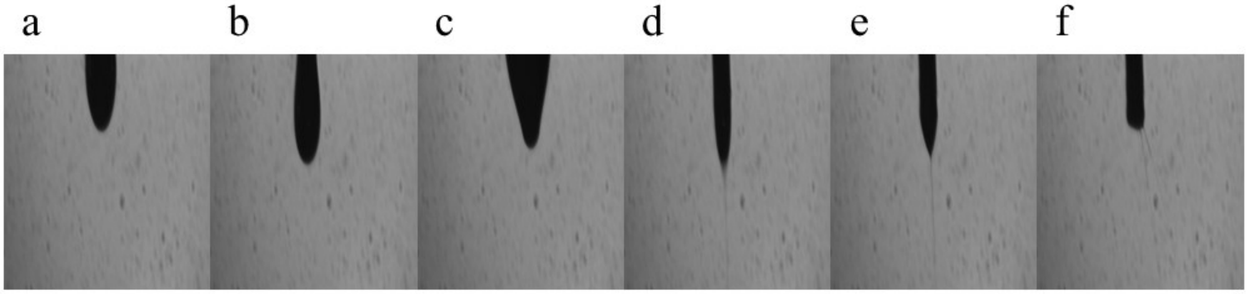

Figure 3-25: Different modes of electrohydrodynamics phenomena. a) nozzle, b) dripping, c) micro dripping, d) unstable cone jet, e) stable cone jet, f) multi cone jet

3.2.3 Gravure Offset Printing System

The printed electronics market is challenging the conventional electronics device manufacturing systems. Printed electronics systems with contact and non-contact printing systems, have advantages of low cost, high speed, simple fabrication on flexible and large area substrates (Perelaer et al., 2010) whereas high integration density and short switching times are the points that printed electronics is yet to achieve (Arias et al., 2010). The noncontact printing system like inkjet or micro dispenser systems have lower throughput and thickness requires proportional larger number of passes (Choi et al., 2012c; A. Khan et al., 2011). Comparing among contact printing systems, the gravure offset printer offers high resolution and larger production volume in a less complicated manufacturing process than that of screen printer (Lahti et al., 1999; Pudas et al., 2004a, 2004b).

Printed electronics needs to move into R2R system fabrication to attain the mass production to cope with the market demand and price reduction. Many researchers have worked on web tension control (Choi et al., 2013; K.-H. Choi et al., 2010; Ponniah et al., 2013; Tran et al., 2013, 2011a, 2011b). Web tension control in the web defines thickness and roughness of printed patterns (Lee et al., 2010). The performance of electronics devices depend on the thickness and roughness of printed patterns (Wang et al., 2011).

The R2R system is discussed in Section 3.2.1. The motor of infeeder was run in speed control mode matching the speed of gravure offset printer motor (Ponniah et al., 2013). The web tension was controlled at a low value of 5 N. The control scheme of R2R system is shown in Figure 3-8.

The gravure offset printer consisted of three rolls as shown in Figure 3-26. AC servomotors drive gravure roll and offset roll while impression roll was idle. Ink was put on the gravure roll which had engraves. When the gravure roll is driven, all ink except that in engraves was removed by doctor blade. The ink was pulled out from gravure roll by PDMS on offset roll and the pattern width and thickness depended on the width and depth of cells of engraves (Sung et al., 2010). The patterns were transferred from offset roll to PET substrate as the surface energy of PET surface is more than the PDMS of offset roll (Pudas et al., 2004a, 2004b). A cleaning roll removed any traces of leftover ink from offset roll. After printing of pattern using gravure offset printer the PET substrate passed through an infrared (IR) drier. Later the patterns are cured in oven.

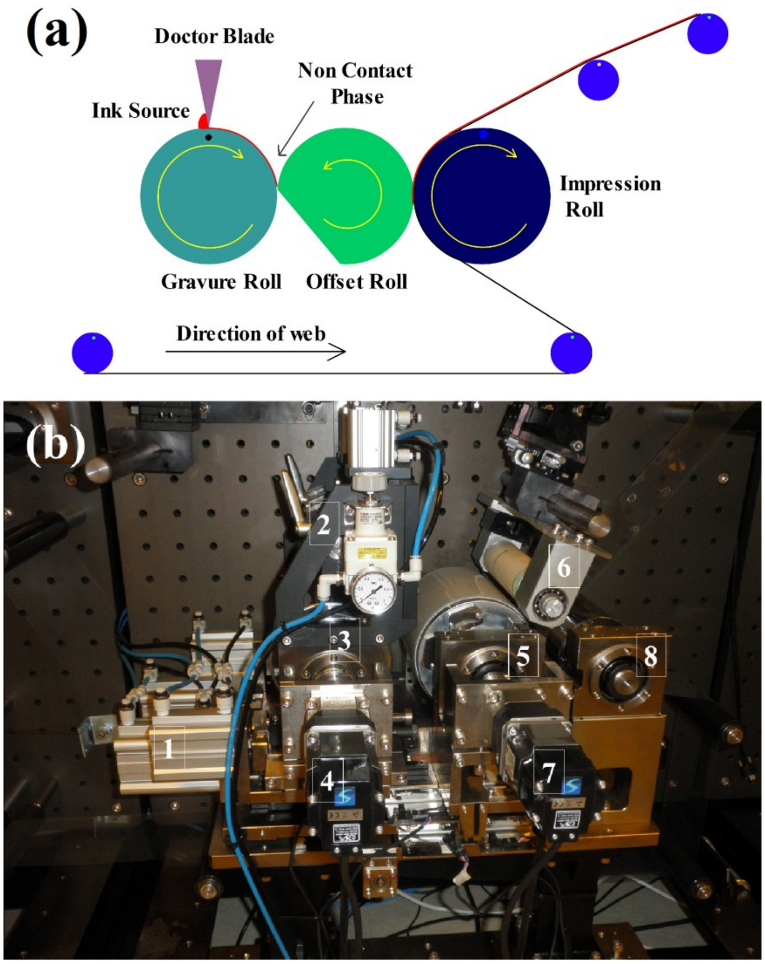

Figure 3-26: Gravure offset printing system a) schematic diagram of system, b) gravure offset system

3.3 Characterization Equipment

Surface morphologies of thin films were analysed by (FE-SEM) (JEOL JSM-7600F, Japan). This system was operated at accelerating voltage of 5 kV. The QDs ink was analysed by high-resolution transmission electron microscopy (HRTEM, JEOL JEM 2100). The thickness of thin film was measured by thin film thickness measuring reflectometer (K-MAC ST4000-DLX). The crystal structure of ZnO-Graphene QDs was verified by XRD analysis which was performed by Rigaku D/MAX 2200H, Bede Model 200 system. This system used Cu-Kα radiations (λ=1.054

nm). The X-ray generation was carried out at voltage of 40 kV with 30 mA current. The diffraction intensity was measured at a scan resolution of 0.2^{o} with the range of 0-80o in the 2θ range. For chemical composition, XPS analysis was performed by using Axis Ultra DLD (Kratos. Inc) with Monochromatic Al Kα (1486.6 eV) X-ray source. The base pressure was kept at 5.0×10^{-9} Torr. The pass energy for survey scan was 160 eV with step size of 1 eV/step while pass energy for narrow scan was 40 eV step size of 0.05 eV/step. Photoluminance (PL) of QDs ink was observed by photoluminescence spectroscopy (Perkin Elmer LS-55) with 365 nm excitation wavelength. The optical properties were studied using ultraviolet/ visible spectrometer (Shimadzu UV-3150) within visible colour range 300-800 nm. The electrical characterization of H-LED devices was performed by semiconductor device analyser (Agilent B1500A) with current resolution of 1 fA. A probe station (MST8000C) was used to place the samples during electrical performance analysis. The HOMO and LUMO values of the QDs were determined from the cyclic voltammetry (CV) for which a three electrode electrochemical cell was used with a potentiostat (VSP, Bio-Logic). We used a glassy carbon disk as a working electrode, a Pt wire as a counter electrode, and a Ag/0.01 M AgNO3 + 0.1 M tetrabutylammonium hexafluorophosphate (TBAPF6) acetonitrile (Ag/Ag+) as a reference electrode. The CV measurements were made from -2.0 V to 1.7 V at a scan rate of 20 mV/s. The luminance of the H-LED devices was measured by Lux meter (Minolta LS-100). The Commission International d'Eclairage (CIE) coordinates (x,y) were also obtained by lux meter. The electroluminance (EL) of devices was measured by calibrated spectrometer (Avantes AvaSpec-ULS2048 StarLine Versatile Fiber-optic).

4. Fabrication of OLEDs

4.1 Substrate cleaning

ITO coated glass and PET substrates of the layer thickness of 100 nm and resistivity of 15 Ω/□ were cleaned with acetone, and then with isopropanol for 15 minutes using bath sonication. After cleaning, the substrates were rinsed with deionized water and dried in air at room temperature. The substrates were placed under UV light for 40 seconds to remove any organic contaminations.

4.2 Fabrication of OLEDs by Spin Coating

Following devices were fabricated by spin coating technique.

OLED SC-A: ITO/PEDOT:PSS/MEH-PPV/Al

OLED SC-B: ITO/PEDOT:PSS/MEH-PPV/(ZnO-Graphene QDs)/Al

OLED SC-C: ITO/PEDOT:PSS/(CdSe/ZnS QDs)/Al

4.2.1 OLED SC-A

The device structure is shown in Figure 4-1. The anode was ITO coated PET. The hole transport layer was of conductive polymer PEDOT:PSS and emissive layer was of conjugate polymer MEH-PPV. Aluminium was the reflective cathode of OLED.

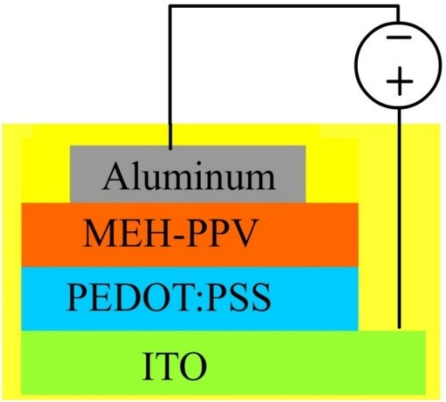

Figure 4-1: Device structure of OLED SC-A

PEDOT:PSS was coated onto a previously cleaned ITO coated glass substrate. The resistivity of ITO coated glass with film thickness of 100 nm was 15 Ω/□. The PEDOT:PSS ink was spin coated onto the ITO coated glass substrate at rpm of 1500 for 30 seconds. The thin film was dried in oven at 100 °C for 30 mins. The MEH-PPV ink was deposited onto the dried PEDOT:PSS thin film by spin coating at 1500 rpm for 30 seconds. This thin film was dried at 100 °C for 30 mins. The aluminium electrode was deposited by thermal evaporation of 100 nm thickness. The device with the active area of 0.64 cm^2 was made at deposition pressure of 10^{-6} torr and deposition rate 3 Å/s. Finally, the device was encapsulated in cavity-formed encapsulation glass. An ultraviolet (UV) epoxy binder was used to seal the glass and substrate. The fabrication process is shown in Figure 4-2.

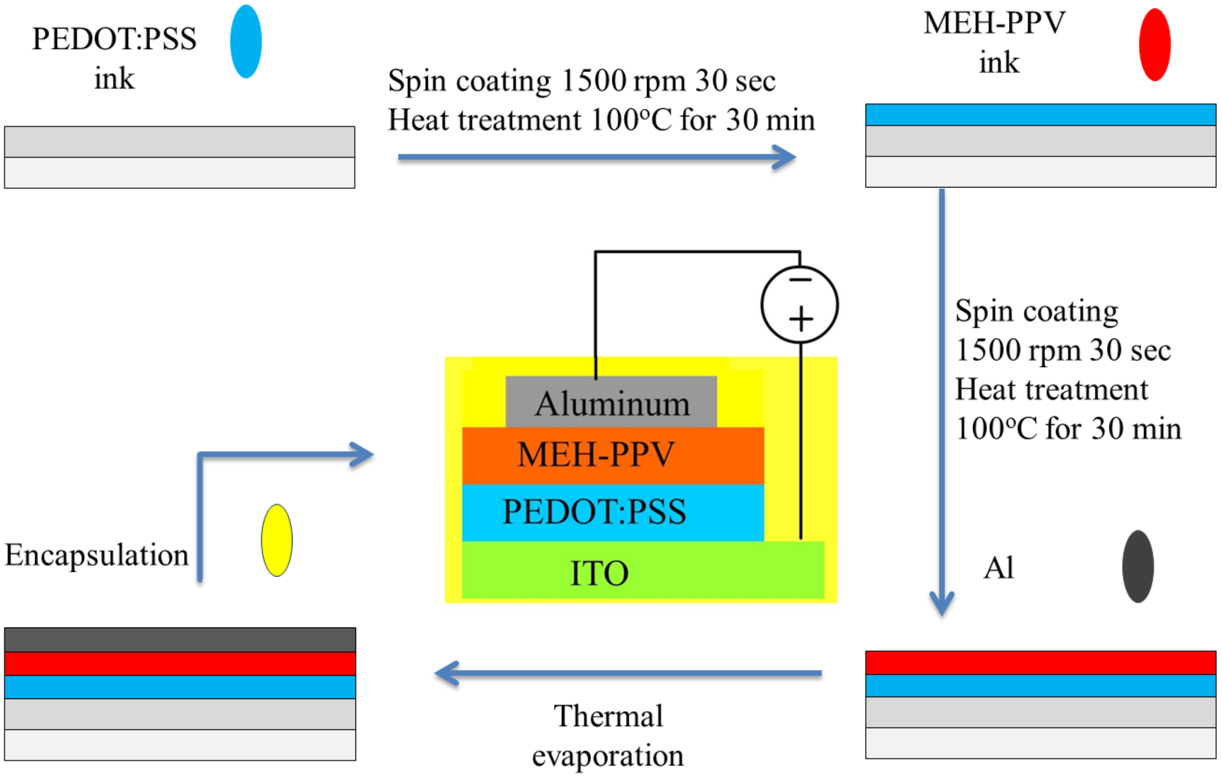

Figure 4-2: Fabrication process of OLED SC-A

4.2.2 OLED SC-B

The device structure is shown in Figure 4-3. The anode was ITO coated PET. The hole transport layer was of conductive polymer PEDOT:PSS and emissive layer was of conjugate polymer MEH-PPV. ZnO-Graphene QDs were used here as the electron transport layer. Aluminium was the top electrode of OLED.

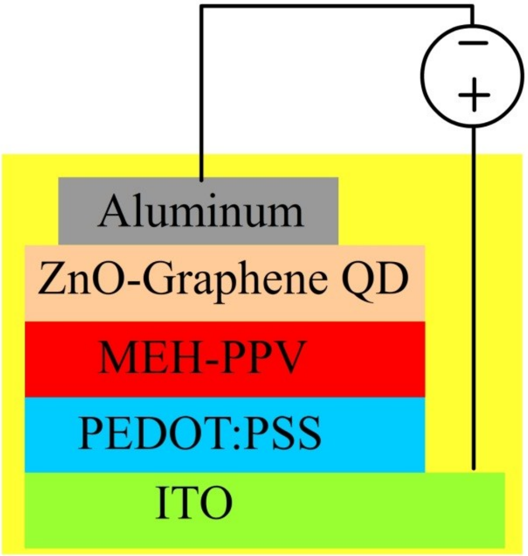

Figure 4-3: Device structure of OLED SC-B

PEDOT:PSS was coated onto a previously cleaned ITO coated glass substrate. The resistivity of ITO coated glass with film thickness of 100 nm was 15 Ω/□. The PEDOT:PSS ink was spin coated onto the ITO coated glass substrate at rpm of 1500 for 30 seconds. The thin film was dried in oven for 100 ^{o}C 30 mins. The MEH-PPV ink was deposited onto the dried PEDOT:PSS thin film by spin coating at 1500 rpm for 30 seconds. This thin film was dried at 100 ^{o}C for 30 mins. ZnO-Graphene QDs were spin coated at 3000 rpm for 30 seconds onto the dried thin film of MEH-PPV. The aluminium electrode was deposited by thermal evaporation of 100 nm thickness. The device with the active area of 0.64 cm^2 was made at deposition pressure of 10^{-6} torr and deposition rate 3 Å/s. Finally, the device was encapsulated in cavity-formed encapsulation glass. An ultraviolet (UV) epoxy binder was used to seal the glass and substrate. The fabrication process is shown in Figure 4-4.

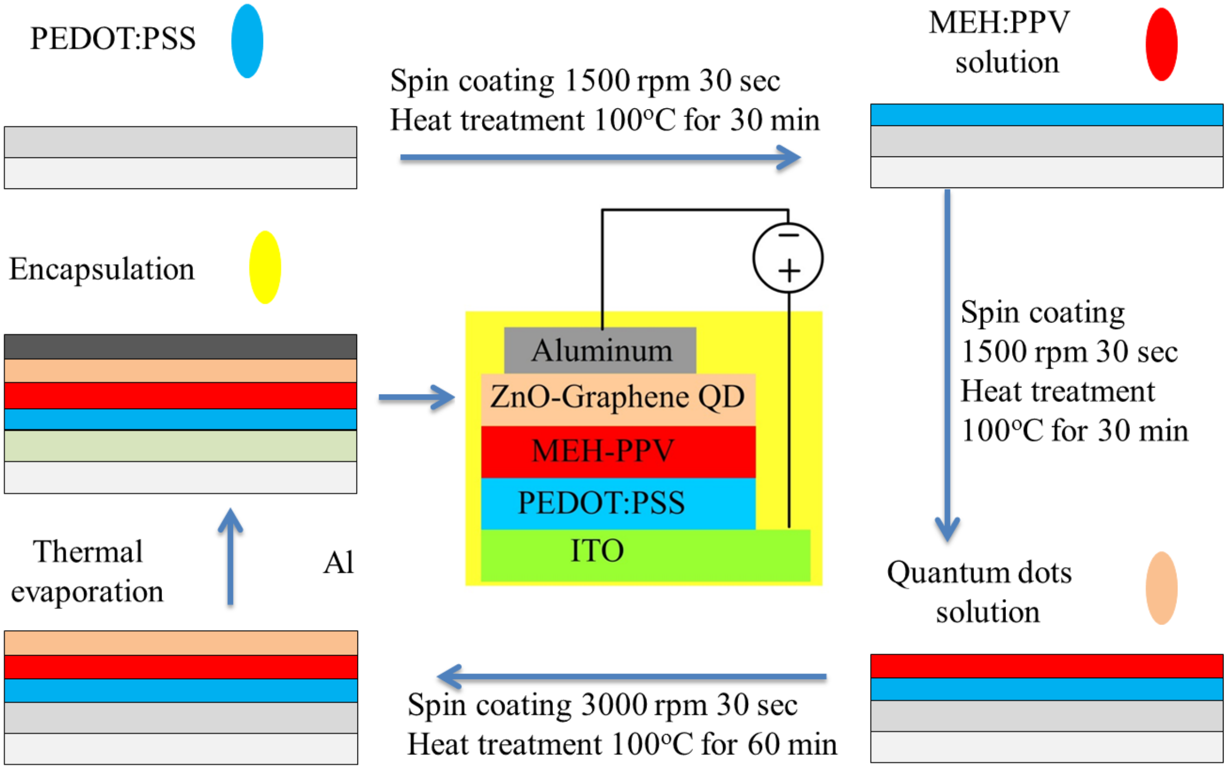

Figure 4-4: Fabrication process of OLED SC-B

4.2.3 OLED SC-C

The device structure is shown in Figure 4-5. The anode was ITO coated PET. The hole transport layer was of conductive polymer PEDOT:PSS and emissive layer was of CdSe/ZnS QDs. Conjugate polymer of MEH-PPV was used here as the electron transport layer. Aluminium was the top electrode, reflective cathode of OLED.

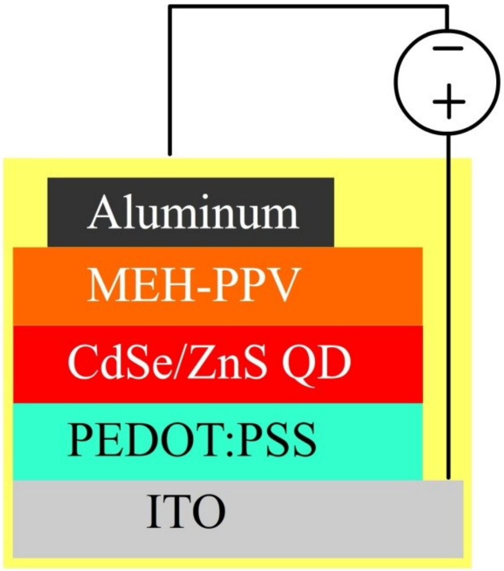

Figure 4-5: Device structure of OLED SC-C

PEDOT:PSS was coated onto a previously cleaned ITO coated glass substrate and PET substrates. The resistivity of ITO coated glass and PET substrate with film thickness of 100 nm was 15 Ω/□. The PEDOT:PSS ink was spin coated onto the ITO coated glass substrate at rpm of 1500 for 30 seconds. The thin film was dried in oven for 100 ^{o}C for 30 mins. CdSe/ZnS QDs were deposited onto dried PEDOT:PSS layer by spin coating at 2000 for 30 seconds. The MEH-PPV ink was deposited onto the dried QDs thin film by spin coating at 1500 rpm for 30 seconds. This thin film was dried at 100 ^{o}C for 30 mins. The aluminium electrode was deposited by thermal evaporation of 100 nm thickness. The device with the active area of 0.64 cm^2 was made at deposition pressure of 10^{-6} torr and deposition rate 3 Å/s. Finally, the device was encapsulated in cavity-formed encapsulation glass. An ultraviolet (UV) epoxy binder was used to seal the glass and substrate. The fabrication process is shown in Figure 4-6.

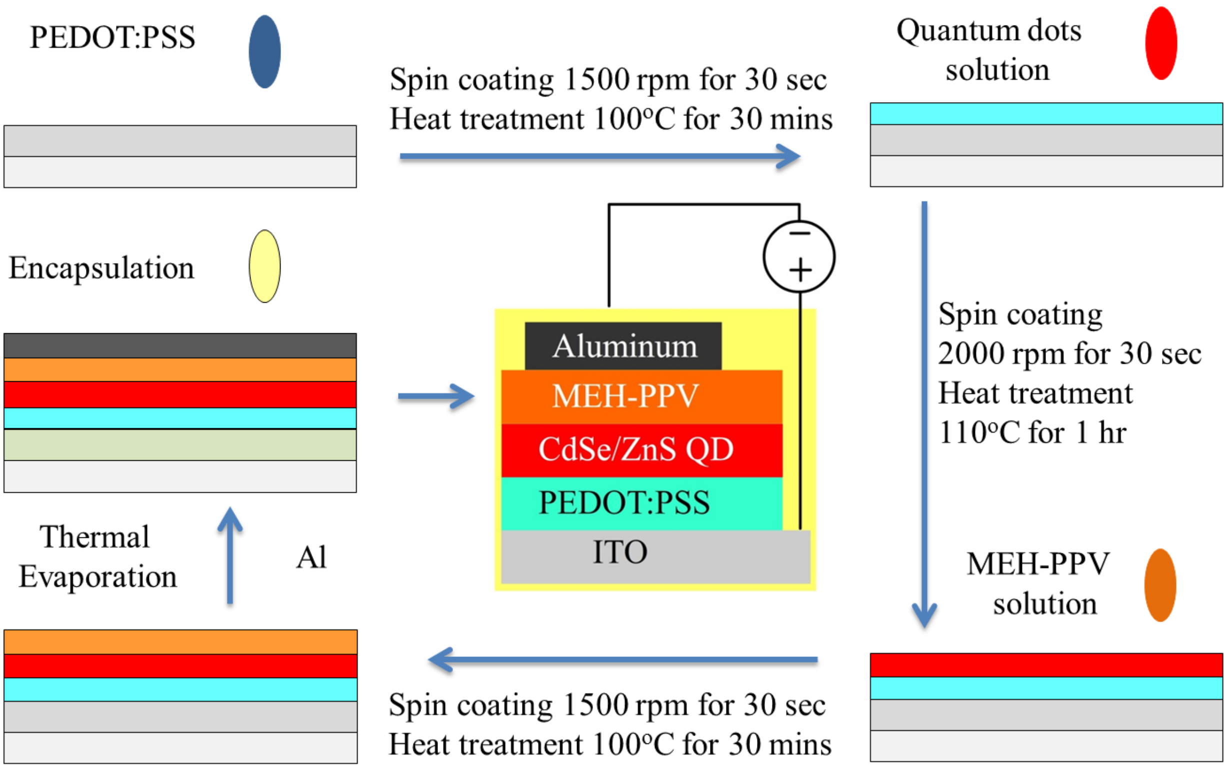

Figure 4-6: Fabrication process of OLED SC-C

4.3 Fabrication of OLEDs by Electrohydrodynamics Spray Process

Following devices were fabricated by electrohydrodynamics spray process.

OLED ESD-A: ITO/PEDOT:PSS/MEH-PPV/Al

OLED ESD-B: ITO/PEDOT:PSS/(CdSe/ZnS QDs)/Al

OLED ESD-C: ITO/PEDOT:PSS/MEH-PPV/Ag

4.3.1 OLED ESD-A

The device structure is shown in Figure 4-7. The anode was ITO coated PET. The hole transport layer was of conductive polymer PEDOT:PSS and emissive layer was of conjugate polymer MEH-PPV. Aluminium was the top electrode of OLED.

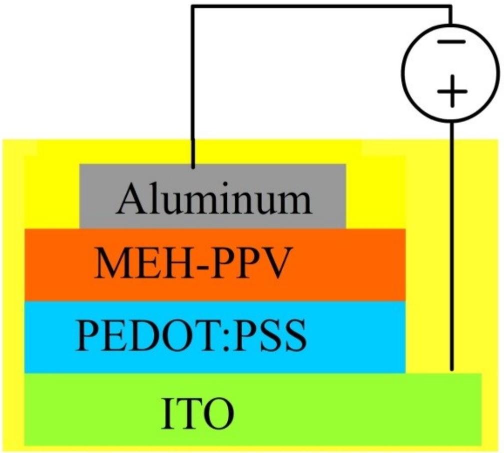

Figure 4-7: Device structure of OLED ESD-A

PEDOT:PSS was sprayed on a cleaned ITO coated PET using the ESD system described in section 2.2.1. After the spray of PEDOT:PSS the thin film was dried in oven at 100 ^{o}C for 30 mins. The parameters for the spray of PEDOT:PSS are mentioned in Table 4-1.

Table 4-1: Process parameters of ESD deposition of PEDOT:PSS

Properties	**Value**
Standoff distance	25 mm
Flow rate	1500 µl/hr
Voltage	5.63 kV
nozzle	210 µm
Speed	3 mm/sec
No of passes	4

The MEH-PPV was sprayed on a dried PEDOT:PSS thin film using the ESD system described in section 2.2.1. Different recipes of inks for MEH-PPV spray were used as shown in Table 4-2. After the spray of MEH-PPV the thin film was dried in oven at 100 ^{o}C for 30 mins. The parameters for the spray of MEH-PPV are mentioned in Table 4-3. After drying the thin film, the aluminium electrode was deposited by thermal evaporation of 100 nm thickness. The device with the active area of 0.64 cm^{2} was made at deposition pressure of 10^{-6} torr and deposition rate 3 Å/s.

Finally, the device was encapsulated by flexible epoxy. The fabrication process is shown in Figure 4-8.

Table 4-2: MEH-PPV inks for spray

Inks Ratio		**Spray ability**
MEH-PPV	**DMF**	
3 (0.5 %)	1	No
1 (0.5 %)	1	No
1 (0.5 %)	3	No
3 (0.3 %)	1	Yes

Table 4-3: Process parameters of ESD deposition of MEH-PPV

Properties	**Value**
Standoff distance	10 mm
Flow rate	200 µl/hr
Voltage	3.81 kV
nozzle	310 µm
Speed	3 mm/sec
No of passes	4

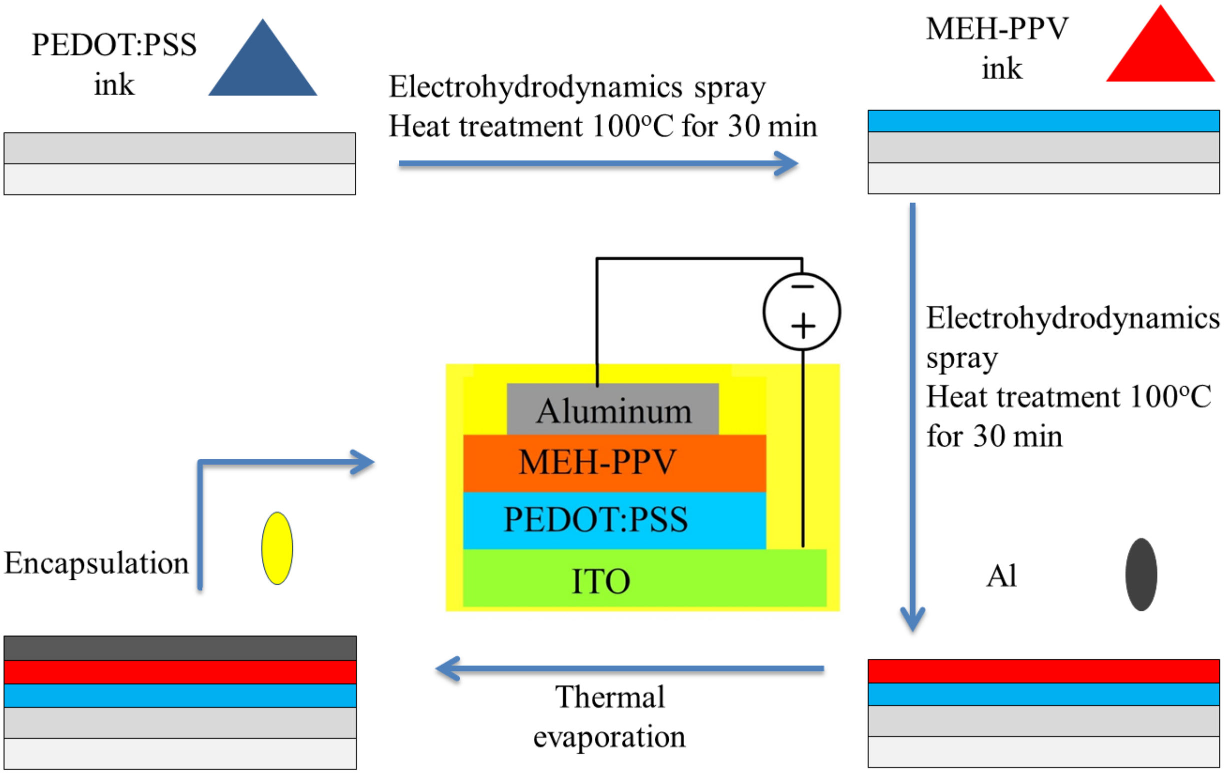

Figure 4-8: Fabrication process of OLED ESD-A

4.3.2 OLED ESD-B

The device structure is shown in Figure 4-9. The anode was ITO coated PET and glass. The hole transport layer was of conductive polymer PEDOT:PSS and emissive layer was of CdSe/ZnS QDs. The conjugate polymer MEH-PPV was used as electron transport layer. Aluminium was the reflective cathode of OLED.

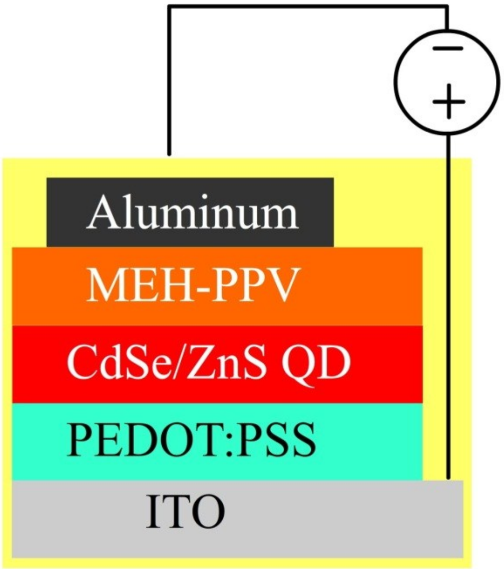

Figure 4-9: Device structure of OLED ESD-B

PEDOT:PSS was spin coated on a cleaned ITO coated PET and glass at 1500 rpm for 30 sec. The thin film of PEDOT:PSS was dried in oven at 100 °C for 30 mins. The CdSe/ZnS QDs were sprayed on a dried PEDOT:PSS thin film using the ESD system described in section 2.2.1. After the spray of QDs the thin film was dried in oven at 110 °C for 60 mins. The parameters for the spray of QDs are mentioned in Table 4-4. After drying the thin film, MEH-PPV was spin coated onto the QDs. The MEH-PPV thin film was dried at 100 °C for 30 mins. The aluminium electrode was deposited by thermal evaporation of 100 nm thickness. The device with the active area of 0.64 cm^2 was made at deposition pressure of 10^{-6} torr and deposition rate 3 Å/s. Finally, the device was encapsulated by flexible epoxy. The fabrication process is shown in Figure 4-10.

Table 4-4: Electrohydrodynamics spray parameters for CdSe/ZnS QDs

Properties	**Value**
Standoff distance	6 mm
Flow rate	150 µl/hr
Voltage	2.8 kV
nozzle	110 µm
Speed	3 mm/sec
No of passes	2

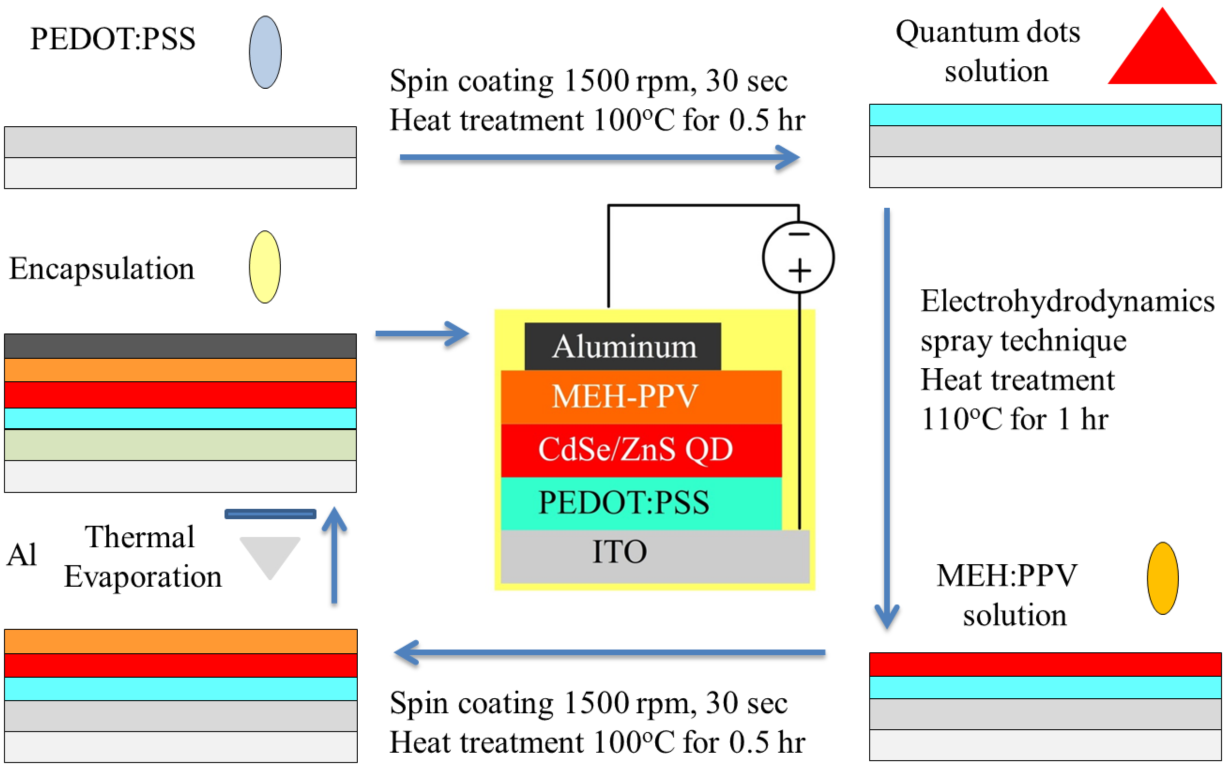

Figure 4-10: Fabrication process of OLED ESD-B

4.3.3 OLED ESD-C

The device structure is shown in Figure 4-11. The anode was ITO coated PET. The hole transport layer was of conductive polymer PEDOT:PSS and emissive layer was of conjugate polymer MEH-PPV. Silver was the reflective cathode of OLED.

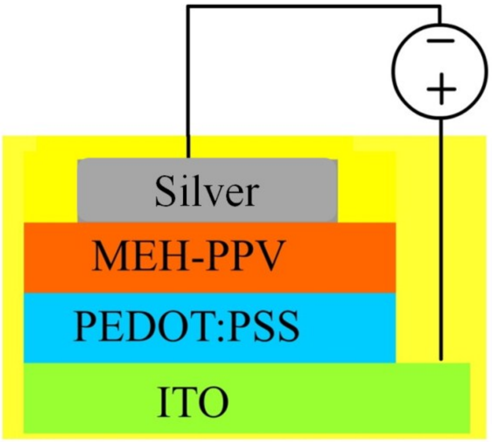

Figure 4-11: Device structure of OLED ESD-C

PEDOT:PSS was sprayed on a cleaned ITO coated PET using the ESD system described in section 2.2.1. After the spray of PEDOT:PSS the thin film was dried in oven at 100 ^oC for 30 mins. The parameters for the spray of PEDOT:PSS are mentioned in Table 4-5. PEDOT:PSS ink modified by adding DMF and Triton was used for this spray explained in section 2.3.2.

Table 4-5: Process parameters of ESD deposition of PEDOT:PSS

Properties	**Value**
Standoff distance	10 mm
Flow rate	1300 µl/hr
Voltage	5.63 kV
nozzle	210 µm
Speed	3 mm/sec
No of passes	4

The MEH-PPV was sprayed on a dried PEDOT:PSS thin film using the ESD system described in section 2.2.1. After the spray of MEH-PPV the thin film was dried in oven at 100 ^oC for 30 mins. The parameters for the spray of MEH-PPV are mentioned in Table 4-6. MEH-PPV ink with addition of ZnO nanoparticles was used as mentioned in Section 2.3.2. After drying the thin film, the silver electrode was printed by gravure offset printer. The gravure offset printing on R2R system is discussed in Section 3.2.2. The patterns were thermally treated at 100 ^oC for 1 hr. The parameters of silver ink are mentioned in Table 4-7. The active area of printed electrodes was 0.144 cm^2. Finally, the device was encapsulated by flexible epoxy. The fabrication process is shown in Figure 4-12.

Table 4-6: Process parameters of ESD deposition of MEH-PPV

Properties	**Value**
Standoff distance	13 mm
Flow rate	1200 µl/hr
Voltage	8.4 kV
nozzle	110 µm
Speed	3 mm/sec
No of passes	4

Table 4-7: Parameter of silver paste used in gravure offset printing

Parameter	Value
Material	Silver nanoparticles
Concentration	70 ~ 80 %
Viscosity	10,000 to 30,000 mpa
Curing temperature	100 °C
Curing Time	1 hr

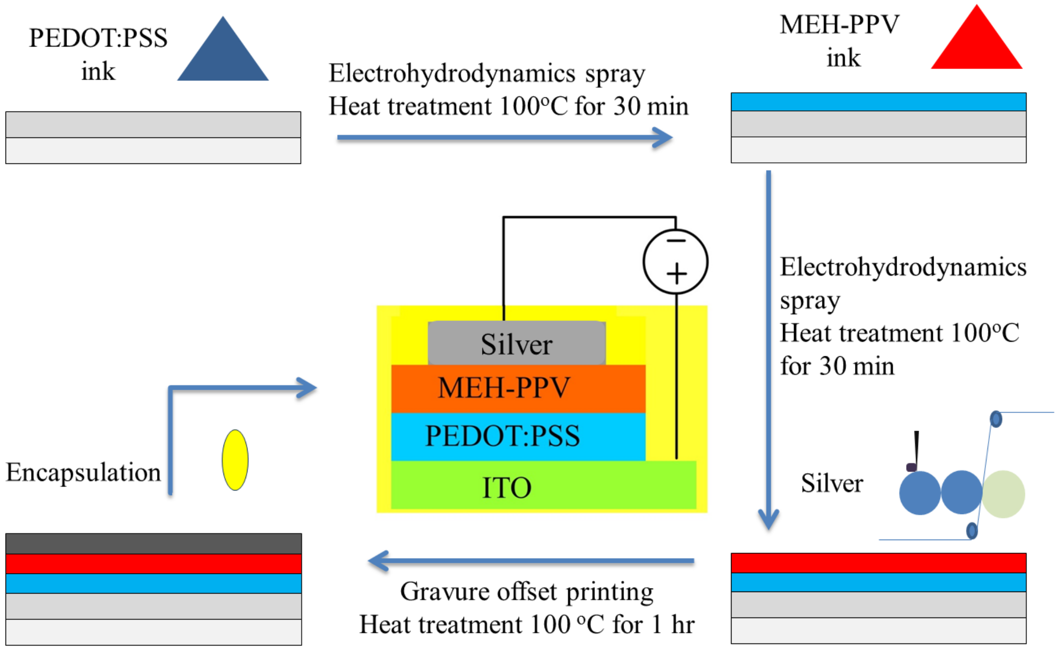

Figure 4-12: Fabrication process of OLED ESD-C

5. Results and Discussion

5.1 Electrohydrodynamics Spray

CdSe/ZnS QDs

An operating envelope at different flow rates was explored by experimentation. The operating envelope of CdSe/ZnS QDs is shown in Figure 5-1. To find the optimized thickness to of the emissive layer for H-LED device application, the standoff distance was varied from 10 mm to 5 mm. With the decrease of standoff distance, a decrease in the spray area was observed; hence, the thickness of the emissive layer was increased. The layer thickness change with respect to change in standoff distance is presented in Table 5-1.

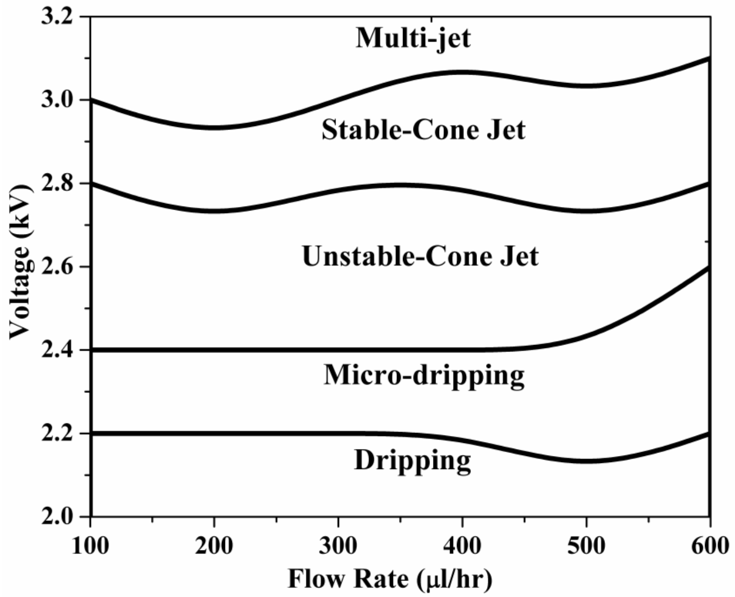

Figure 5-1: Working Envelop of CdSe/ZnS QDs at different flow rates

Table 5-1: Thickness of thin layer of CdSe/ZnS QDs at different standoff distance

Standoff Distance (mm)	**Thickness of CdSe/ZnS QDs layer (nm)**
10	183
9	225
8	262
6	350
5	1156

5.2 Material / Thin Films Analysis

5.2.1 Surface Morphology

The surface morphology of thin film coated by spin coating was observed. The FE-SEM images of PEDOT:PSS, MEH-PPV and ZnO-Graphene QDs are shown in Figure 5-2, 5-3 and 5-3 respectively. These layers were found to be densely packed and continuous. The layer defects like pores or craters were not observed. The layers were satisfactory for diode application. The QDs spin coated on polymer matrix of PEDOT:PSS layer were well dispersed. The average thickness of PEDOT:PSS, MEH-PPV and ZnO-Graphene QDs thin layers coated on bare glass substrate came out to be around 100 nm, 50 nm and 120 nm respectively measured by non-destructive thin film reflectometer measurement system. Each measurement was taken by averaging the thickness of the thin film noted at ten different points.

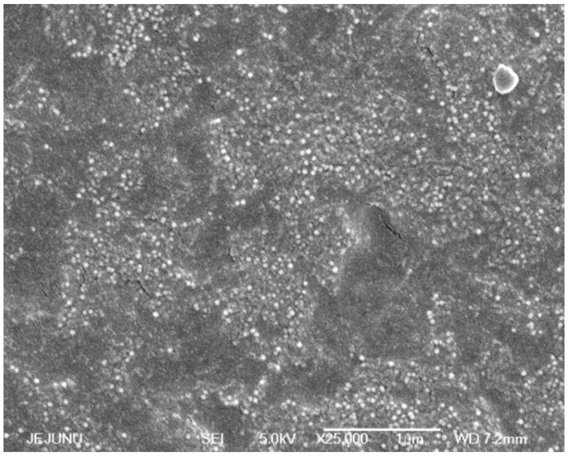

Figure 5-2: FE-SEM image of PEDOT:PSS thin film fabricated by spin coating

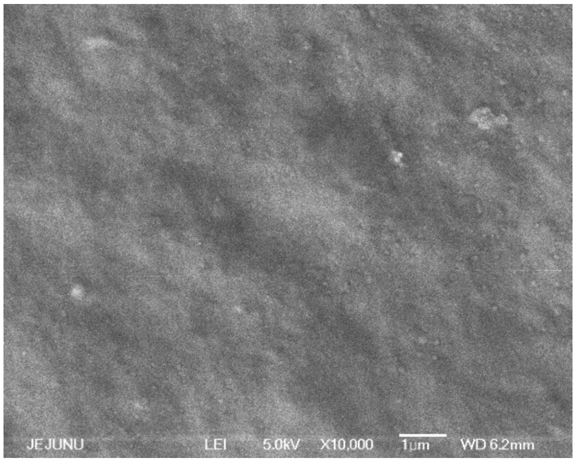

Figure 5-3: FE-SEM image of MEH-PPV thin film fabricated by spin coating

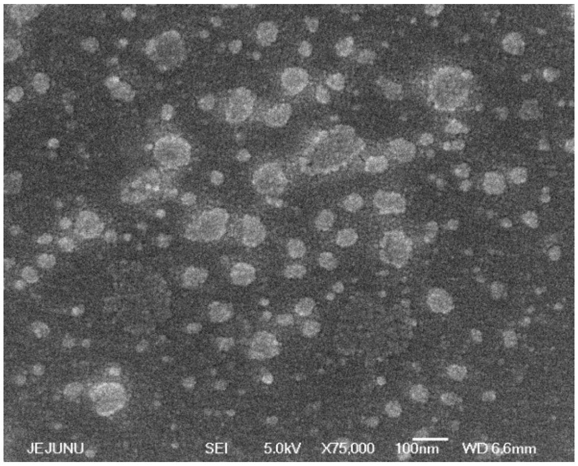

Figure 5-4: FE-SEM image of ZnO-Graphene QDs thin film fabricated by spin coating

The surface morphology of thin layers fabricated by electrohydrodynamics spray technique of PEDOT:PSS, MEH-PPV and silver are shown in Figure 5-5, 5-6 and 5-7 respectively. The coated layers were non-porous, homogenous, and densely packed. No defects like crakes or craters were observed in thin films. The average thickness of PEDOT:PSS and MEH-PPV on bare glass substrate came out to be around 100 nm and 120 nm respectively measured by non-destructive thin film reflectometer measurement system. Each measurement was taken by averaging the thickness of the thin film noted at ten different points. The pattern height of silver pattern deposited by gravure offset printer was measured by 3D scanning system. The average width of pattern was found out to be 210 μm and thickness of pattern was 195 nm.

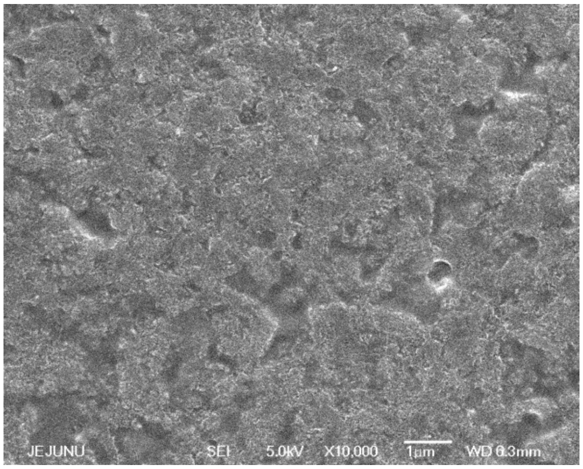

Figure 5-5: FE-SEM image of PEDOT:PSS thin film fabricated by electrohydrodynamics spray

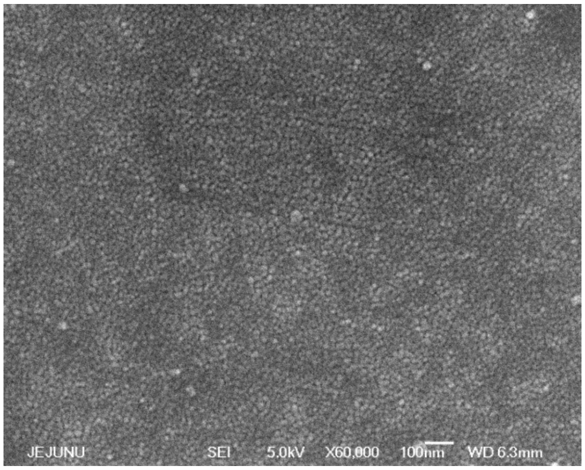

Figure 5-6: FE-SEM image of MEH-PPV thin film fabricated by electrohydrodynamics spray

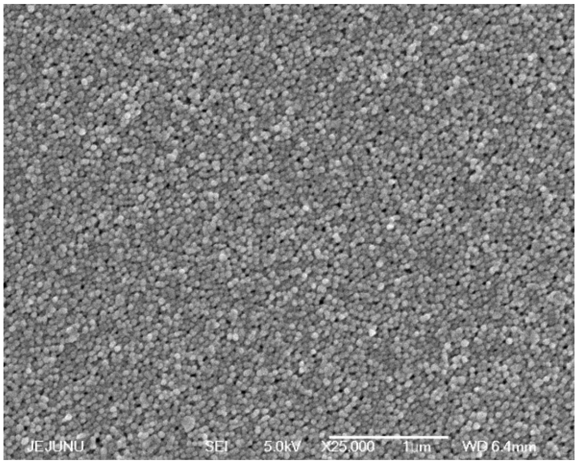

Figure 5-7: FE-SEM image of silver pattern fabricated by gravure offset printing

5.2.2 Quantum Dots Analysis

Structural integrity of CdSe/ZnS QDs was investigated by TEM analysis. The TEM image of CdSe/ZnS QDs is shown in Figure 5-8. The average particle size of CdSe/ZnS QDs was about 6.5 to 8 nm. The lattice spacing of CdSe/ZnS QDs was 0.4 nm.

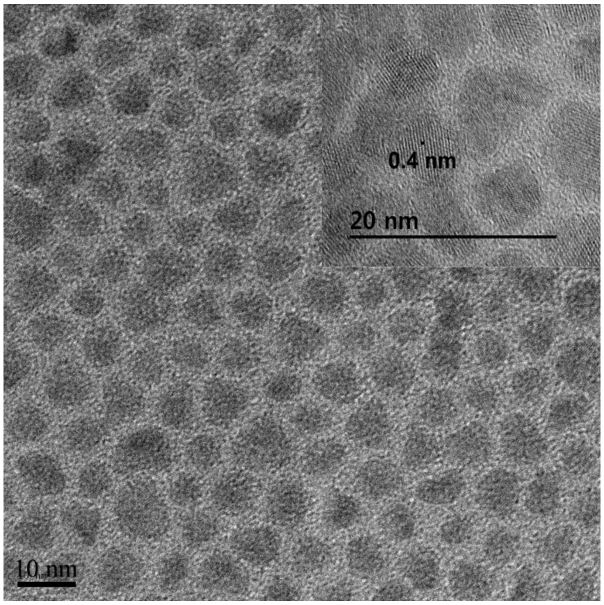

Figure 5-8: HR-TEM image of CdSe/ZnS QDs with lattice spacing of 0.4 nm

5.2.3 Compositional Analysis

The XRD analysis of ZnO-Graphene QDs layer spin coated on bare glass substrate is shown in Figure 5-9. The (100), (002), (101) and (102) peaks confirmed the presence of ZnO. The broadening of ZnO peaks in XRD was the result of the small size of QDs. The average size of ZnO particles was calculated by Scherrer equation.

$$\tau = \frac{K\lambda}{\beta \cos\theta} \tag{5-1}$$

Where 'τ' was mean size, 'λ' was X-ray wavelength which in this case was 0.15406 nm, 'β' was the line broadening at half of maximum intensity (FWHM). The approximate size of ZnO QDs was calculated around 4.32 nm. Graphene broad peaks were observed at 25.8^o and 43.5^o.

The chemical composition of ZnO-Graphene QDs was verified by XPS analysis. The XPS spectra of ZnO-Graphene QDs spin coated on bare glass substrate is shown in Figure 5-10. The XPS survey spectra of ZnO-Graphene QDs showed peaks of zinc, carbon and oxygen. The carbon C 1s peak was observed at 286.0 eV. The carbon spectra can be de-convoluted into four different carbon bonding groups. sp^2 carbon (C-C at 286.0 eV), C-O bond (286.3 eV), C=O bond (288.8 eV), O-C=C bond (290.2 eV)(Ding et al., 2013; Song et al., 2012; Umar et al., 2005). Here it can be seen that the C-C bonds of graphene had high intensity while O-C=O bond of graphene with ZnO were also present. This showed that graphene sheets were covering ZnO QDs and O-C=O bond of carbon were the bond between the oxygen of ZnO and carbon atoms at the edges of graphene sheets. Oxygen 1s peak was detected at 533.5 eV. Zinc peaks were detected at 1046.2 eV and 1023.16 eV.

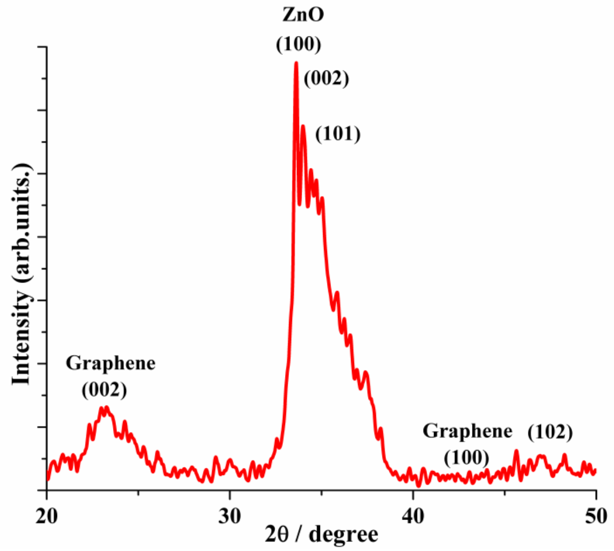

Figure 5-9: XRD analysis of ZnO-Graphene QDs

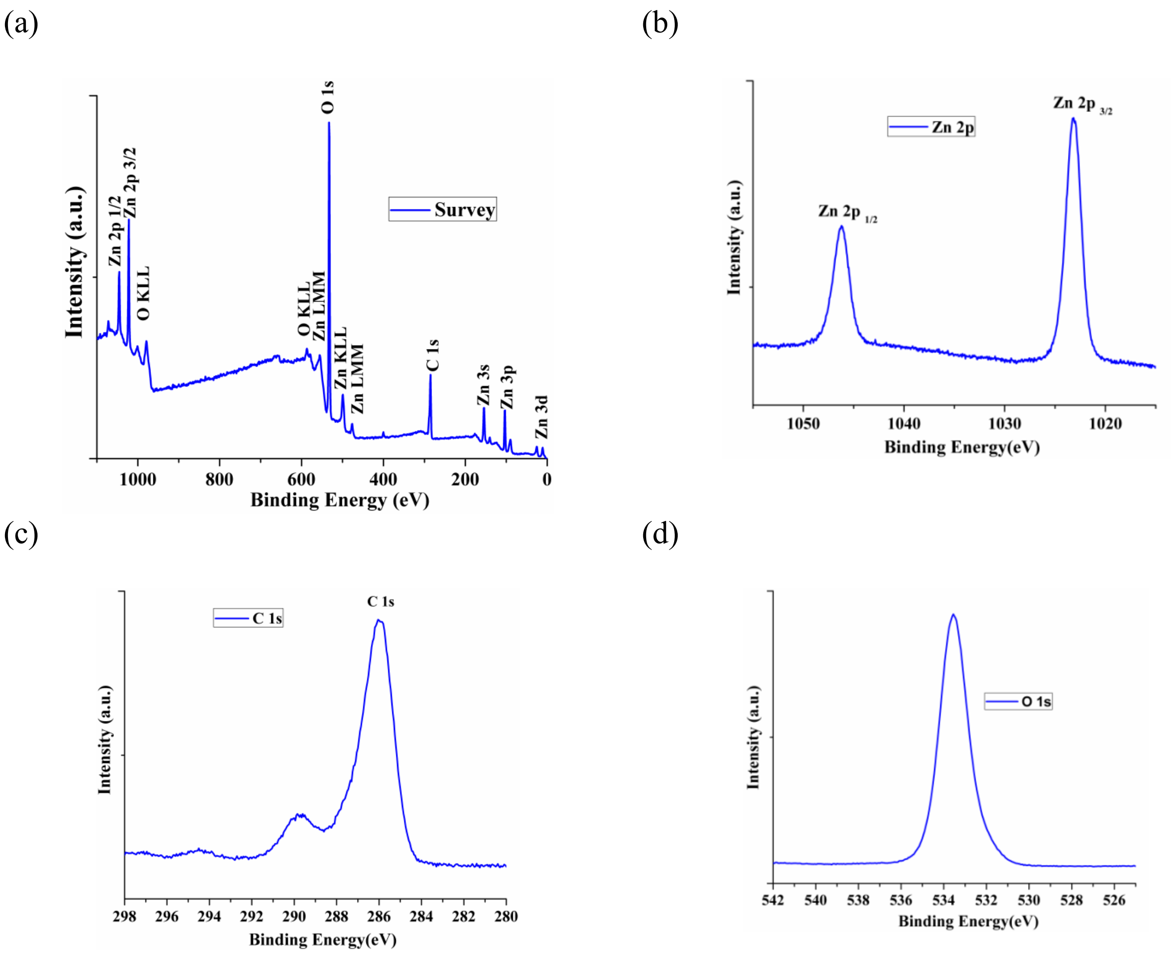

Figure 5-10: XPS analysis of ZnO-Graphene QDs a) survey, b) peaks of zinc, c) carbon, d) oxygen

5.2.4 Optical Analysis

The absorbance spectra of PEDOT:PSS, QDs and MEH-PPV layers spin coated on bare glass substrate are shown in Figure 5-11. The absorption spectrum of ZnO-Graphene QDs showed no absorbance in visible range. The light emitted by the device was by MEH-PPV layer. The direct energy band gap of QDs was calculated using absorbance spectrum 3.7 eV using the following equation.

$$\alpha h\nu = E_D\left(h\nu - E_g\right)^{1/2} \tag{5-2}$$

Where 'α' is the optical absorption, 'E_g' is band gap energy, 'E_D' is a constant, '$h\nu$' is the photon energy. To find the direct band gap energy, $(\alpha h\nu)^2$ was calculated and was plotted as a function of photon energy. The linear portions of absorbance were extrapolated to the X-axis to get the approximate direct energy band gap of ZnO-Graphene QDs which was found out to be 3.7 eV as shown in Figure 5-12. In literature, the reported HOMO and LUMO of ZnO are 7.6 eV and 4.2 eV respectively which give the direct band gap energy of 3.4 eV (Zhang et al., 2010). The reported band gap energy of graphene is 4.4 eV (Son et al., 2012). The blended direct band gap was higher because the band gap increases by decreasing particle size(Bera et al., 2010).

Photoluminescence (PL) of MEH-PPV and ZnO-Graphene QDs spin coated on bare glass substrate are shown in Figure 5-13. The MEH-PPV PL spectra confirms with already reported values (Rosa-Fox, 1999). The PL of ZnO-graphene QDs shows the presence of both graphene at 448 nm (Gan et al., 2013) and ZnO with peaks at 503 nm and 700 nm (Hazra et al., 2013; Sharma et al., 2010) respectively.

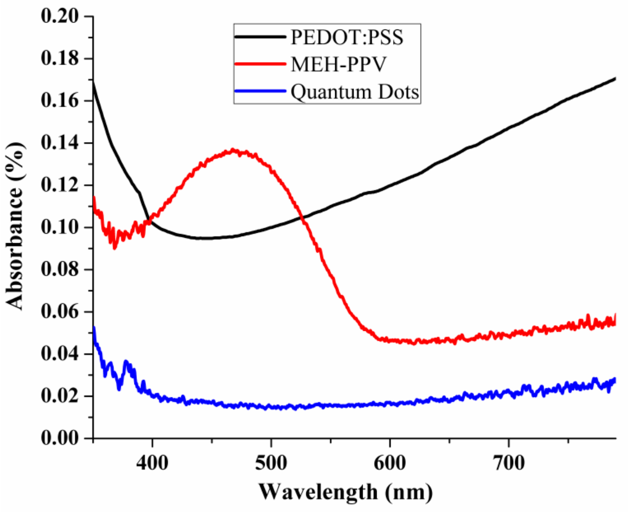

Figure 5-11: Absorbance spectra of spin coated PEDOT:PSS, MEH-PPV and ZnO-Graphene QDs

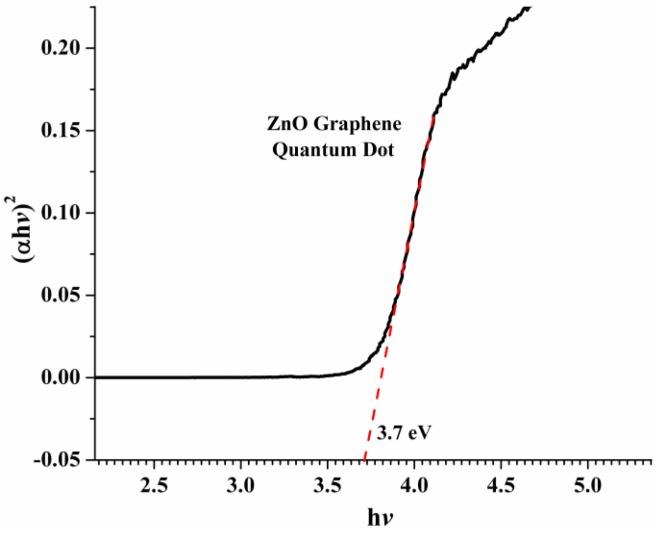

Figure 5-12: Energy band gap of ZnO-Graphene QDs

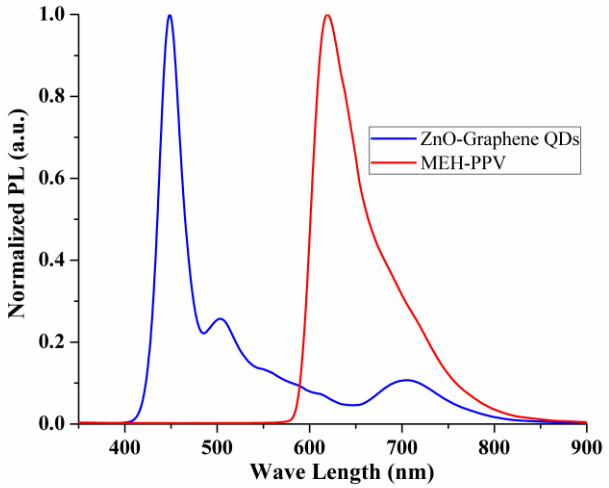

Figure 5-13: Photoluminescence of ZnO-Graphene QDs and MEH-PPV

The normalized photoluminance intensity (PL) of CdSe/ZnS QDs solution and absorbance spectrum of CdSe/ZnS QDs layer is shown in Figure 5-14. The CdSe/ZnS QDs showed a single narrow peak at 634 nm. In visible light spectrum, this wavelength lies in red color region. The absorbance spectrum of CdSe/ZnS QDs layer corresponds to the reported values in literature (Mason et al., 2011; Yildiz and Raymo, 2006).

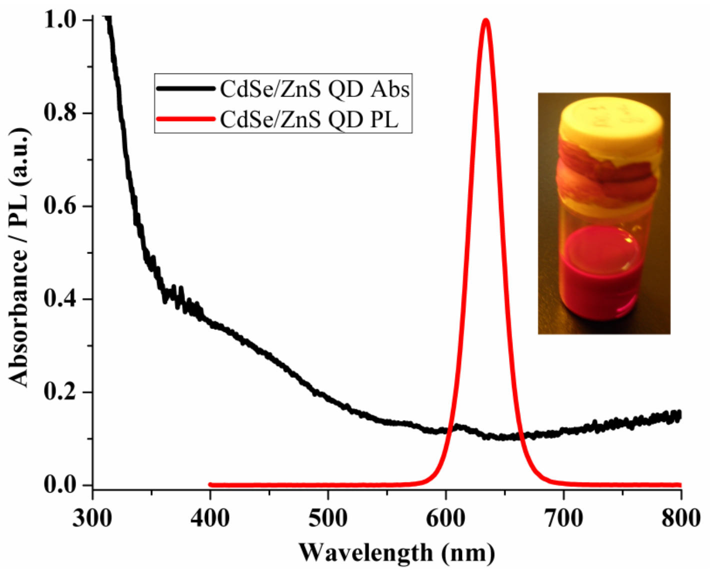

Figure 5-14: Photoluminescence and absorbance spectra of CdSe/ZnS QDs

5.3 Device Characterization

5.3.1 Electrical Analysis

The electrical characterization (I-V) of three OLEDs without QDs is shown in Figure 5-15. Here the devices SC-A and ESD-A had same device structure while they were fabricated by spin coating and electrohydrodynamics spray respectively. The spin coated device showed higher current densities. The device with silver top electrode printed by gravure offset printer showed current density of 15 mA/cm^2. The active area of this device was 0.144 cm^2.

The I-V analysis of three OLEDs with QDs is shown in Figure 5-16. Here the devices SC-C and ESD-B had same device structure while they were fabricated by spin coating and electrohydrodynamics spray respectively. The spin coated device showed higher current densities. The device with ZnO-graphene QDs as electron transport layer showed current density of 48 mA/cm^2. The turn on voltage of this device was 3.5 V while all other devices had turn on voltage of 4.5 V.

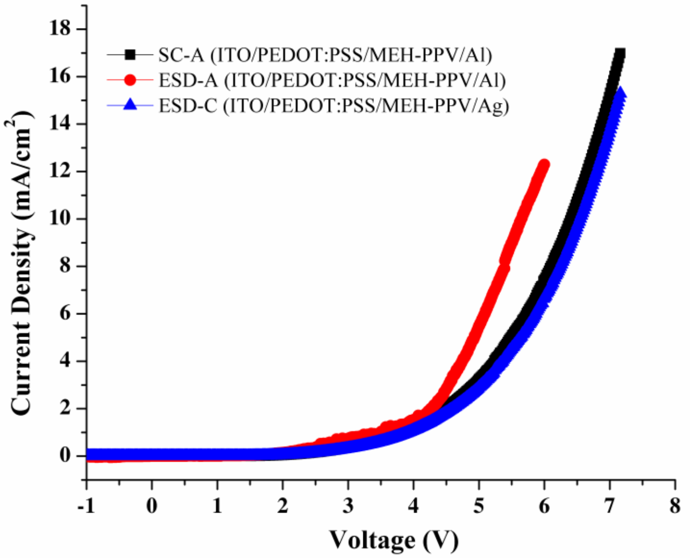

Figure 5-15: I-V analysis of OLEDs without QDs

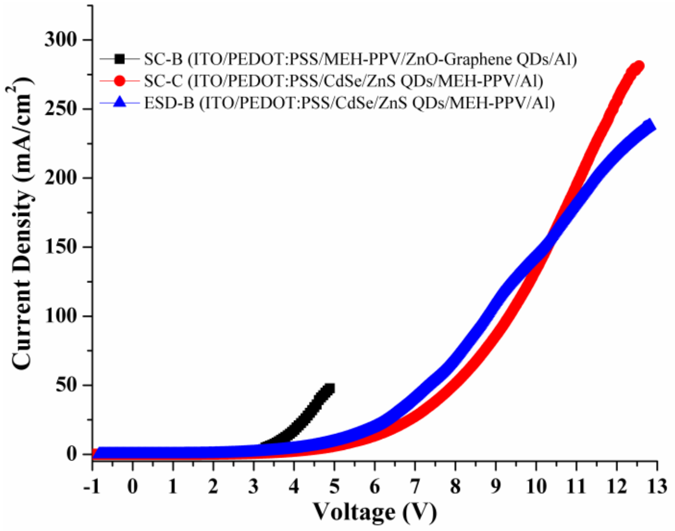

Figure 5-16: I-V analysis of OLEDs with QDs

During the fabrication of OLED device (ESD-B) by ESD spray the number of passes were optimized. The I-V analysis of devices (ESD-B) at different number of passes is shown in Figure 5-17. Here it can be seen that with 2 passes a good electrohydrodynamic spray was achieved.

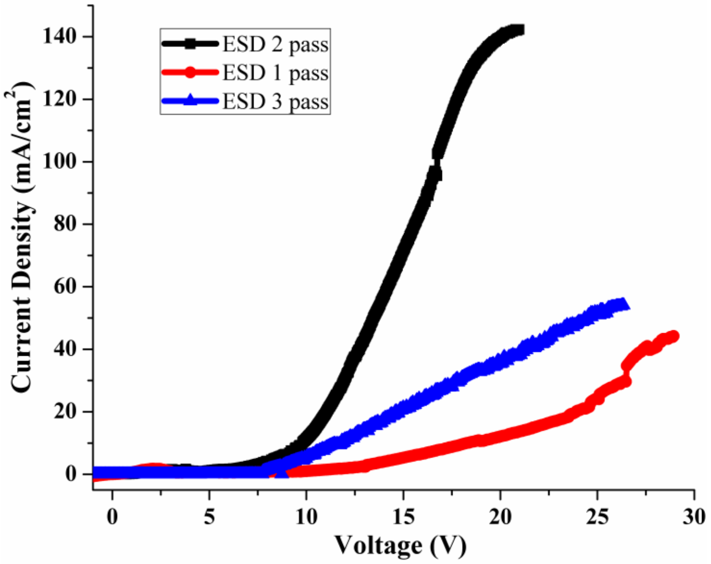

Figure 5-17: I-V analysis of CdSe/ZnS QDs OLEDs at different number of spray passes of ESD

The current density with respect to voltage of OLED (ESD-B) devices on glass substrates at different standoff distances and PET substrate at 6 mm standoff distance are shown in Figure 5-18. Here it can be seen that device (ITO/PEDOT:PSS/QDs/MEH-PPV/Al) shows non-ideal, schottky diode behavior with hopping charge transport mechanism (Houtepen, 2007). The current density of OLED increased with the decrease of standoff distance. The decrease of standoff distance increased the film thickness as area of spray was reduced. At the standoff distance of 6 mm, highest current density was achieved but further decreasing the standoff distance to 5 mm, wetting in electrohydrodynamics atomization observed. In wetting phenomena, wet film on substrate was observed instead of a semi-dry film after performing EHDA as droplet falls on substrate before they are properly atomized into micron-sized particles. This wetting caused the thin layer thickness to jump from 350 nm to 1156 nm and hence a thick layer of QDs by wetting was achieved which showed reduced current.

The flexible device was fixed in a lab made motorized cyclic bending fixture by which the device was tested at 5 mm radius of curvature. The I-V measurement was performed after number of bending as shown in Figure 5-19. The organic layers did not show any degradation while lower current densities were attributed to the brittle nature of ITO (Chen et al., 2002).

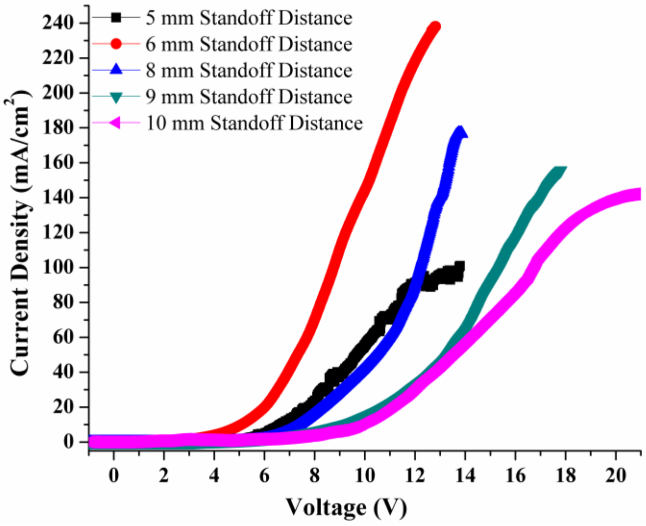

Figure 5-18: I-V analysis of CdSe/ZnS QDs OLEDs at different standoff distance of ESD-B

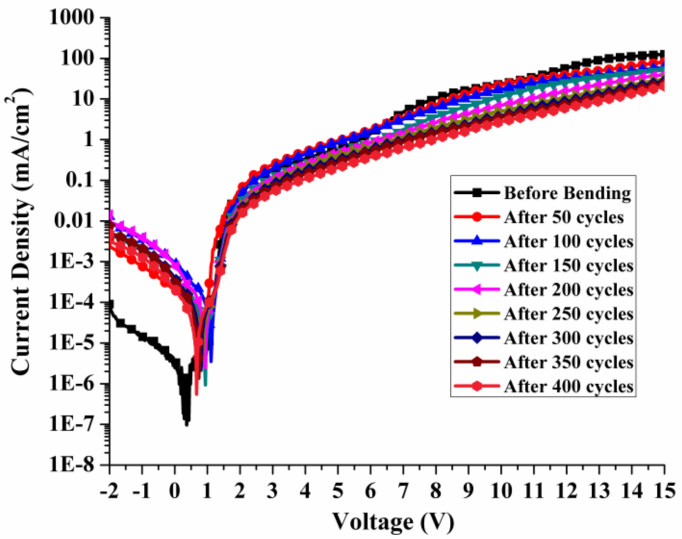

Figure 5-19: I-V curves of flexible OLED ESD-B after cyclic bending testing

The energy level diagrams of all fabricated OLEDs are shown in Figure 5-20. The highest occupied molecular orbital (HOMO), lowest unoccupied molecular orbitals (LUMO) of ITO (Son et al., 2012), PEDOT:PSS (Khillan et al., 2005), MEH-PPV (Alam and Jenekhe, 2002) and ZnO-graphene QDs (Mustapha and Fekkai, 2011; Nguyen et al., 2013; Son et al., 2012). were taken from the literature while the HOMO & LUMO values of CdSe/ZnS QDs were measured by cyclic voltammetry. The HOMO and LUMO of CdSe/ZnS QDs were found out to be -5.785 eV and -3.555 eV respectively with energy band gap of 2.23 eV.

The PEDOT:PSS with high work function of -5.1 eV transports the holes into emissive layer from ITO with work function of 4.7 eV. The low work function cathode provides the electrons. In the device SC-B ZnO-Graphene the IV of this device shows lower leakage current density. This lower leakage current shows the better mobility of holes in the device. The QDs organic diode showed the turn-on voltage reduction from 4.5 V to 3.02 V. The current density increased from 16 mA/cm^2 to 47.7 mA/cm^2 which attributed to the enhancement of electronic properties by ZnO-Graphene QDs.

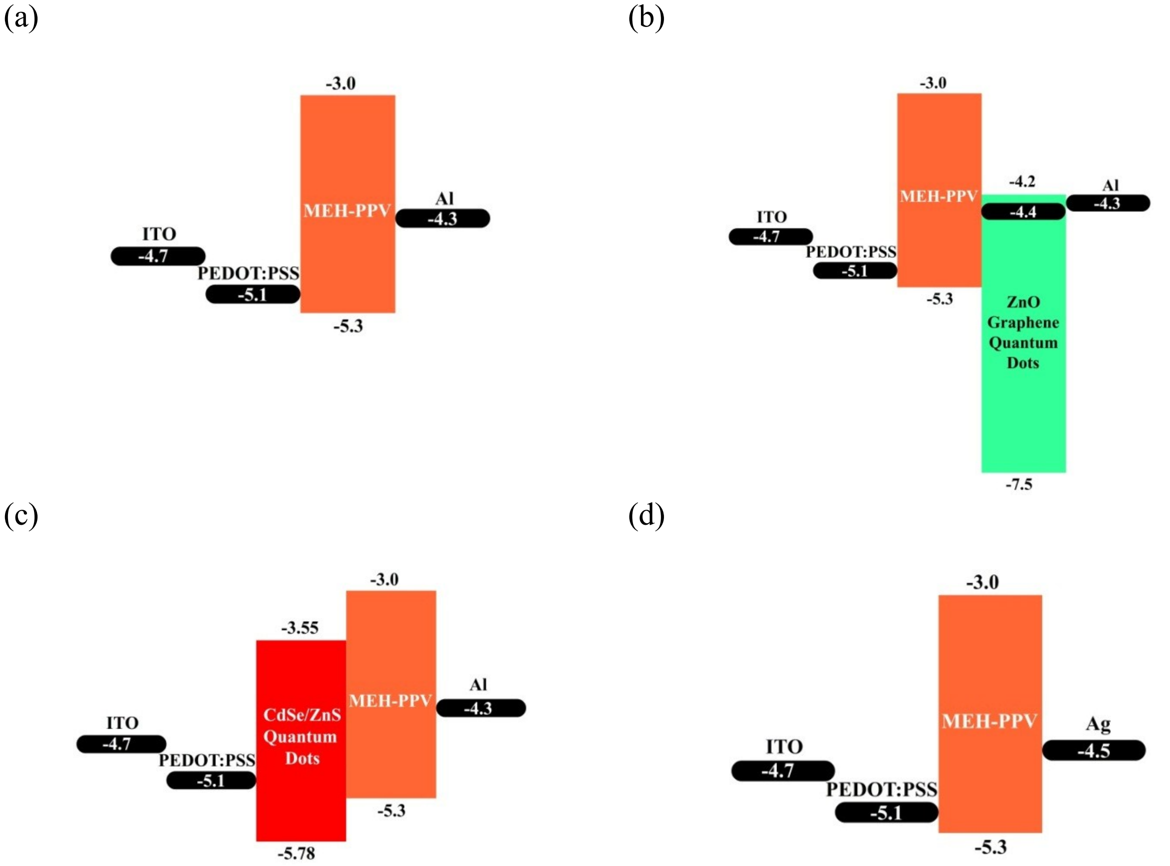

Figure 5-20: Energy level diagram of OLEDs. a) SC-A and ESD-A, b) SC-B, c) SC-C and ESD-B, d) ESD-C

5.3.2 Electroluminescence Analysis

The electroluminescence spectrum of OLED with MEH-PPV as emissive layer is shown in Figure 5-21. Figure 5-22 shows the electroluminescence spectrum of OLED with CdSe/ZnS QDs as emissive layer on glass and PET substrates. This electroluminance intensity at the wavelength

634 nm showed that the achieved luminescence of the device was by QDs layer and MEH-PPV acted as electron transport layer and was not involved in any emission of light.

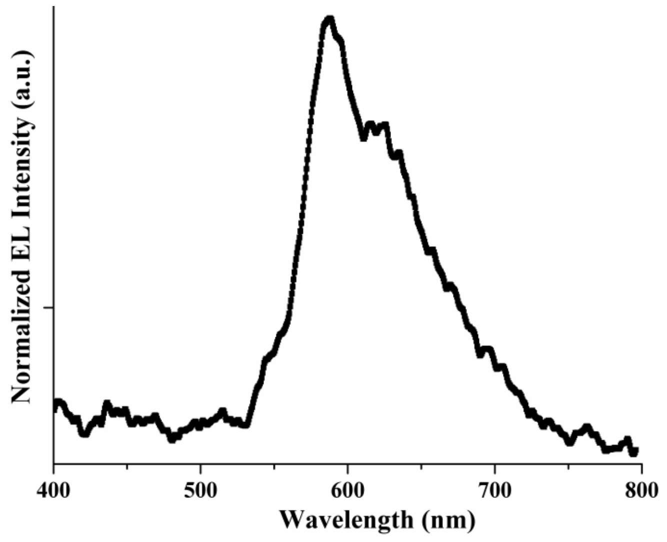

Figure 5-21: Electroluminescence of OLEDs with MEH-PPV as emissive layer

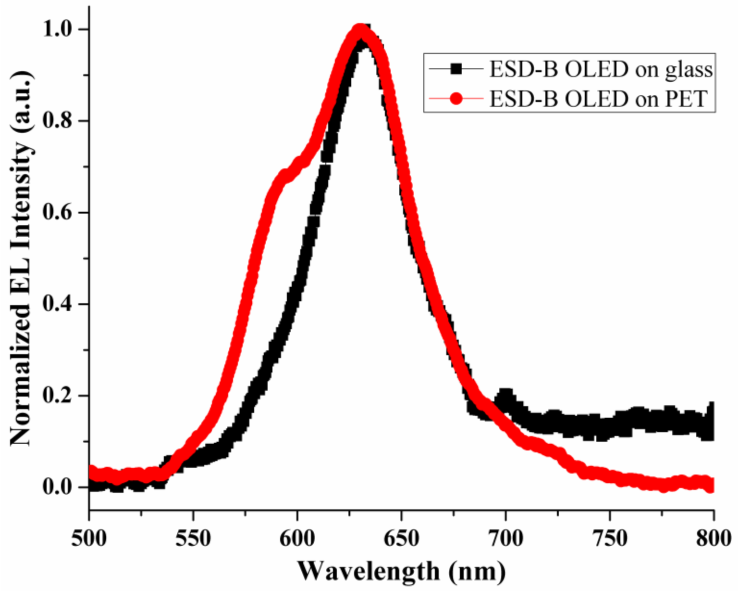

Figure 5-22: Electroluminescence of OLEDs with CdSe/ZnS QDs as emissive layer

The luminescence of OLEDs is shown in Figure 5-23. Luminescence was measured by lux meter. The maximum luminescence was observed by the device SC-C which had the device structure ITO/ PEDOT:PSS/ CdSe/ZnS QDs/ Al fabricated by spin coating technique. This device had also shown maximum current density. The device ESD-B showed more uniform lighting, which had the same device structure but the QDs layer was fabricated by ESD technique.

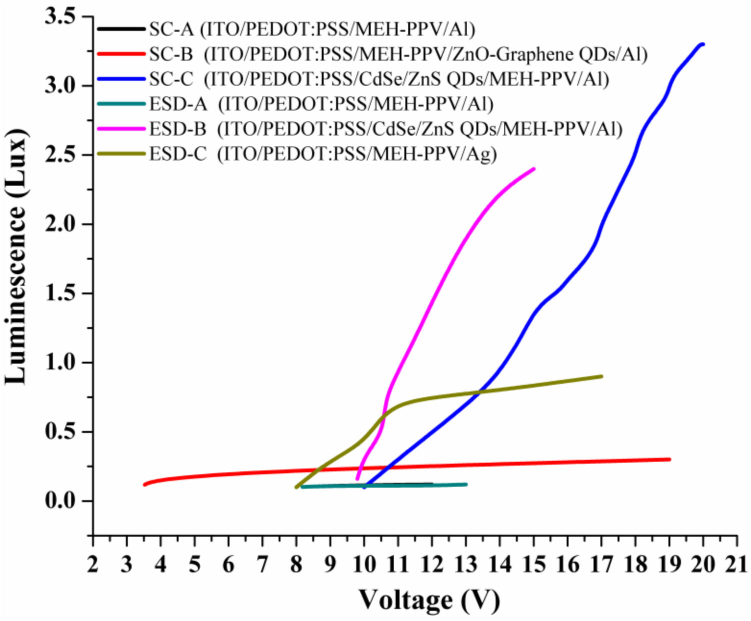

Figure 5-23: Luminescence of OLEDs

Different number of passes optimized the spray of CdSe/ZnS QDs. The comparison of different passes is shown in Figure 5-24. The ESD of QDs with two passes gave better results.

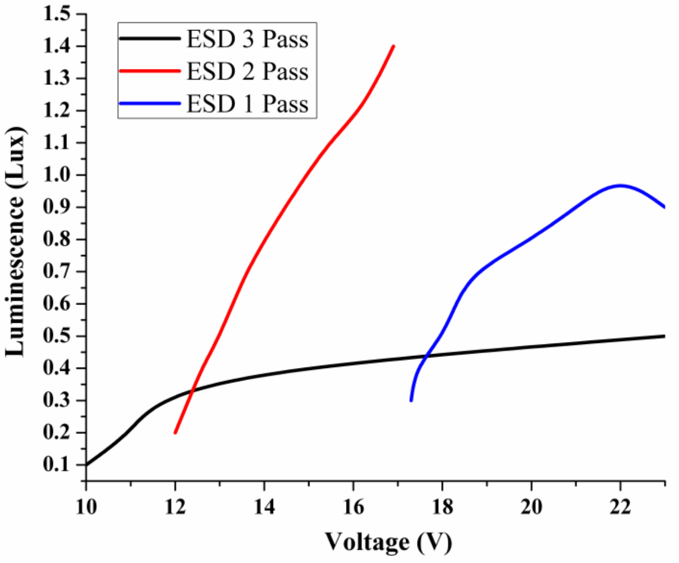

Figure 5-24: Luminescence of OLEDs ESD-B with different number of passes

The standoff distance was also a contributing factor for the thickness of CdSe/ZnS QD layer. The standoff distance was varied and output luminescence of device was measured as shown in Figure 5-25. The CdSe/ZnS QD at the standoff distance of 6 mm showed maximum luminescence that verifies the I-V characterization. The luminescence decreases at 5 mm standoff distance as wetting phenomena occurred at this distance. The wetting of substrate happens when the droplets from the con jet do not have enough distance for the evaporation of the solvent to ensue. The luminescence of OLED ESD-B on glass substrate and PET substrate is shown in Figure 5-26.

The Commission International d’Eclairage (CIE) coordinates (x,y) were also obtained by lux meter are shown in Figure 5-27 on CIE chromaticity chart with black dots show the ESD-B, green dots show ESD-C, white dots show SC-C, blue dots show SC-A, SC-B, ESD-A OLEDs.

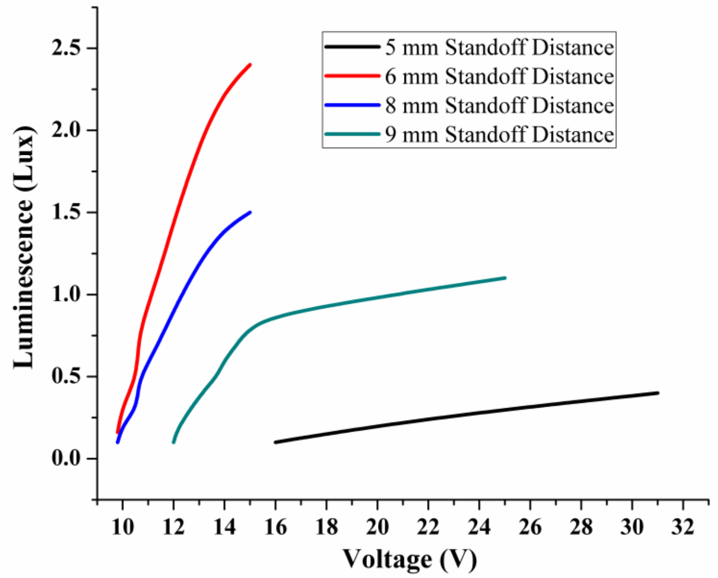

Figure 5-25: Luminescence of OLEDs ESD-B with different standoff distances

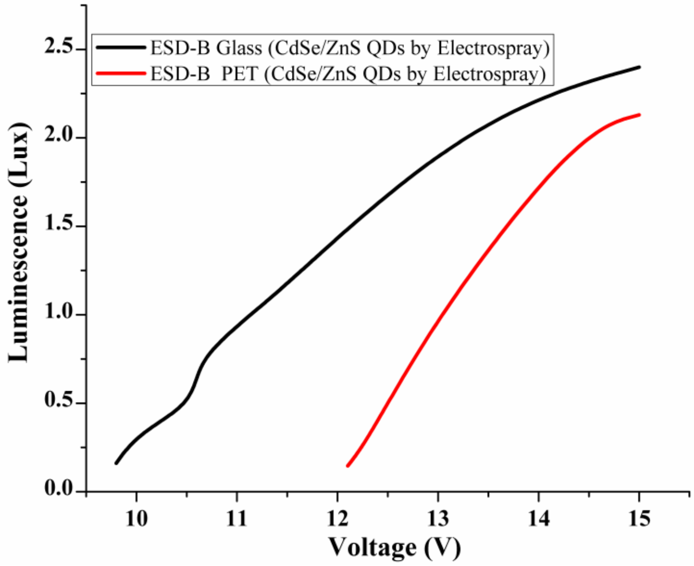

Figure 5-26: Luminescence of OLEDs ESD-B on glass and PET substrate

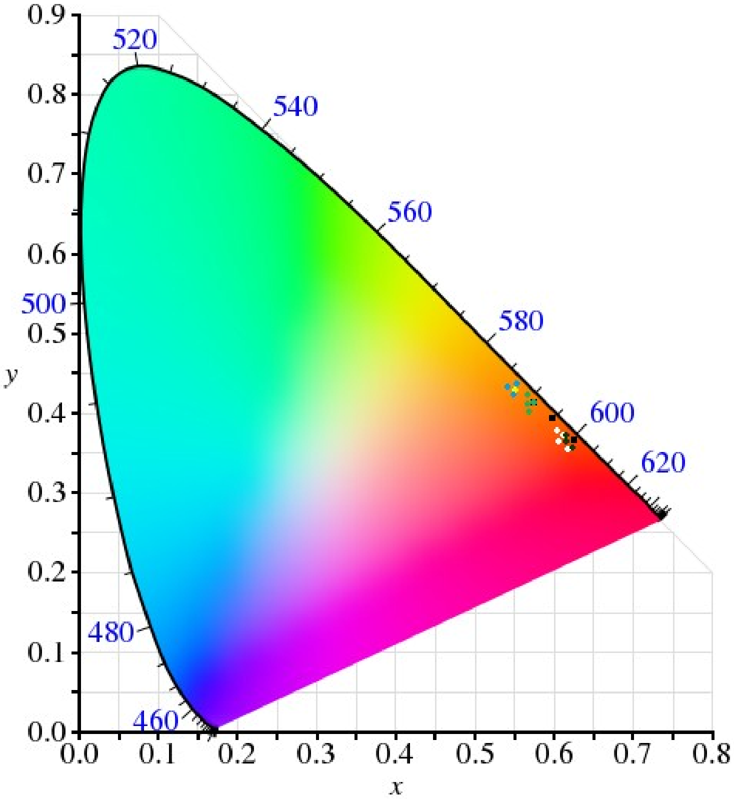

Figure 5-27: CIE color coordinates of OLEDs. Black dots show the ESD-B, green dots show ESD-C, white dots show SC-C, blue dots show SC-A, SC-B, ESD-A

5.4 Discussion

Here the conventional spin coating scheme is compared with the electrohydrodynamics spray deposition technique. The OLEDs fabricated by the spin coating technique produce comparatively better results than those of ESD. The spin-coated devices had better current densities and luminescence as shown in Table 3-8. However spin coating has many disadvantages such as wastage of costly material, unsuitability for large area substrates, lower throughput and difficulties in thickness control of nano-scale thin films.

Electrohydrodynamics spray deposition technique showed comparable results as presented in Table 5-2. The ESD process is continues and a R2R processing system is used to fabricate the OLEDs. The ESD process is a single step process and it is applicable on large area substrates using different materials. There are no materials wastages in ESD process, which makes it an inexpensive and alternative of classical spin coating. Solution concentration, standoff distance, spray time, ink flow rate and nozzle diameter can easily control the thickness of thin films. The electrohydrodynamics process gives clear advantages over the classical spin coating technique in terms of price, mask free and continuous fabrication on large scale using various substrates for OLEDs device applications as shown in Table 5-3.

Table 5-2: Comparison of fabricated OLEDs

Title	**SC-A**	**SA-B**	**SA-C**	**ESD-A**	**ESD-B**	**ESD-C**
Device Structure	ITO/ PEDOT:PSS / MEH-PPV/ Al	ITO/ PEDOT:PSS/ MEH-PPV/ ZnO Graphene QDs/ Al	ITO/ PEDOT:PSS/ CdSe/ZnS QDs/ MEH-PPV/ Al	ITO/ PEDOT:PSS/ MEH-PPV/ Al	ITO/ PEDOT:PSS/ CdSe/ZnS QDs/ MEH-PPV/ Al	ITO/ PEDOT:PSS/ MEH-PPV/ Ag
Fabrication Process	spin coated	spin coated	spin coated	ESD	ESD	ESD
Max Current Density	16.98 mA/cm^2 at 7 V	47.74 mA/cm^2 at 4.89 V	281.25 mA/cm^2 at 12.55 V	12.30 mA/cm^2 at 6 V	238.08 mA/cm^2 at 12.8 V	15.29 mA/cm^2 at 7.16 V
Turn on Voltage	4.5 V	3.02 V	3.93 V	4.3 V	3.26 V	4.61 V
Max Luminescence	0.12 lux at 12 V	0.3 lux at 19 V	3.3 lux at 20 V	0.12 lux at 13 V	2.4 lux at 15 V	0.9 lux at 17 V

Table 5-3: Comparison of fabrication processes

Properties	**Spin Coating**	**Electrohydrodynamics Spray**
Large area substrates	No	Yes
Ink wastage	Significant	None
Ink preparation	Simple	Moderate
Roll-to-Roll system Compatible	No	Yes
Ambient Conditions	Yes	Yes
Cost	Moderate	Low
Masking Required	Yes	No
Throughput	Low	Moderate

6. Conclusions and Future Work

6.1 Conclusions

The organic light emitting diodes (OLEDs) have out preformed the inorganic light emitting diodes. OLEDs have bright future for the next generation display and lighting applications. Conventional solution based OLEDs are fabricated using spin coating technique. The spin coating technique has disadvantages that are wastage ink, difficulties to control thickness at nano-scale, and inability of material deposition on large area substrates.

The fabrication of organic light emitting diode by printed electronics approaches has been achieved using electrohydrodynamics spray deposition. OLEDs were fabricated by both spin coating and electrohydrodynamics spray deposition and the processes have been compared.

The experimental hardware of a three span R2R system is described. Web tension control of a multispan R2R system for printed electronics is achieved by applying regularized variable learning rate on back propagation neural networks. The MIMO system is controlled by decentralized MISO scheme. The nonlinearity of interaction of spans is minimized by introducing multiple inputs from the corresponding interacting spans and nonlinear activation functions. The auto tuning of weights cater for the time variant nature of the system. The steady state error of second span is within ±1 N where the load cells noise is ±0.7 N. The system has rise time of 150 ms and settling time of 0.5 s. A dancer system is added to enhance the web tension control in printing span from 3.75 N to 4.75 N. The results give fast auto tuning while avoid system instability hence giving a solution for a R2R system for printed electronics.

The electrohydrodynamics spray deposition technique is used for the spray of PEDOT:PSS, CdSe/ZnS QDs and MEH-PPV inks. MEH-PPV and PEDOT:PSS ink have been tailored to fit the inks for electrohydrodynamics deposition. ZnO nanoparticles are added to the MEH-PPV ink to remove the electrospinning phenomena form electrohydrodynamics spray deposition.

The OLEDs have been compared on the bases of their fabrication methods. Electrohydrodynamics spray deposition samples have comparable current densities and luminescence to the spin coated samples but also electrohydrodynamics deposition technique is applicable for large area substrates and is process-able on a R2R system without any ink losses. The mass scale fabrication of OLED is achieved by electrohydrodynamics spray deposition with gravure offset printing of silver top electrodes on OLED.

The electrohydrodynamic spray deposition provides the mass scale printing of OLEDs that can satisfy the future demands of efficient displays and lighting at lower price.

6.2 Future Work

The transparent electrode is a key feature of OLEDs function. Many researchers have focused on the suitable replacement of ITO as it has many disadvantages as discussed in section 4.1. Silver nanowires, carbon nanotubes, and conducting polymer are in competition with ITO but still their conductivity does not match with ITO. An ITO free OLED fabricated by R2R system is an interesting topic for future research. It would be interesting to see the blend of AgNW and CNT as transparent electrode. Pressing the thin film of CNT and AgNW at pressure to make smooth film with better conductivity would be interesting. Development of solution based low work function electrode would be another interesting topic of research.

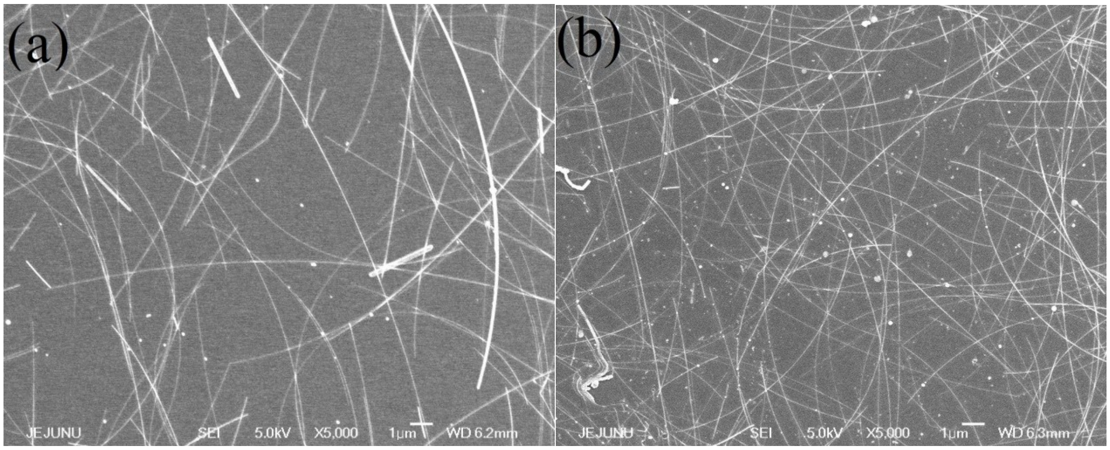

Figure 6-1: Transparent electrode a) AgNW, b) CNT and AgNWs

REFERENCES

Aernouts, T., Vanlaeke, P., Geens, W., Poortmans, J., Heremans, P., Borghs, S., Mertens, R., Andriessen, R., Leenders, L., 2004. . Thin Solid Films 451-452, 22–25.

Alam, M.M., Jenekhe, S. a., 2002. . Chem. Mater. 14, 4775–4780.

Amini, J., 2008. . J. Sci. Iran. Electr. Comput. … 15, 558–567.

Arias, A.C., MacKenzie, J.D., McCulloch, I., Rivnay, J., Salleo, A., 2010. . Chem. Rev. 110, 3–24.

Arshak, K., Velusamy, V., Korostynska, O., Oliwa-Stasiak, K., Adley, C., 2009. . IEEE Sens. J. 9, 1942–1951.

Ashizawa, S., Horikawa, R., Okuzaki, H., 2005. . Synth. Met. 153, 5–8.

Atherton, D.P., Majhi, S., 1999. 3843–3847.

Awais, M.N., Choi, K.H., 2013. . Jpn. J. Appl. Phys. 52, 05DA05 1–5.

Awais, M.N., Kim, H.C., Doh, Y.H., Choi, K.H., 2013a. . Thin Solid Films 536, 308–312.

Awais, M.N., Muhammad, N.M., Navaneethan, D., Kim, H.C., Jo, J., Choi, K.H., Duraisamy, N., 2013b. . Microelectron. Eng. 103, 167–172.

Bae, W.K., Kwak, J., Lim, J., Lee, D., Nam, M.K., Char, K., Lee, C., Lee, S., 2010. . Nano Lett. 10, 2368–73.

Bera, D., Qian, L., Tseng, T.-K., Holloway, P.H., 2010. . Materials (Basel). 3, 2260–2345.

Burroughes, J.H., Bradley, D.D.C., Brown, A.R., Marks, R.N., Mackay, K., Friend, R.H., Burns, P.L., Holmes, A.B., 1990. . Nature 347, 539–541.

Chang, C.-C., Pai, C.-L., Chen, W.-C., Jenekhe, S.A., 2005. . Thin Solid Films 479, 254–260.

Chen, B., Cui, T., Liu, Y., Varahramyan, K., 2003. . Solid. State. Electron. 47, 841–847.

Chen, C.-L., Chang, K., Chang, C.-M., 2004. . Appl. Math. Model. 28, 863–876.

Chen, Z., Cotterell, B., Wang, W., 2002. . Eng. Fract. Mech. 69, 597–603.

Cheng, H., Lin, K., Hsu, H.-C., Hsieh, W.-F., 2006. . Appl. Phys. Lett. 88, 261909.

Chin, Y.-M., Lin, J.-C., Lin, Y.-J., Wu, K.-C., 2010. . Sol. Energy Mater. Sol. Cells 94, 2154–2157.

Cho, K.-S., Lee, E.K., Joo, W., Jang, E., Kim, T., Lee, S.J., Kwon, S.-J., Han, J.Y., Kim, B.-K., Choi, B.L., Kim, J.M., 2009. . Nat. Photonics 3, 2–6.

Choi, K., Rahman, K., Muhammad, N.M., Khan, A., Kwon, K., Doh, Y., Kim, H., 2011. Electrohydrodynamic Inkjet – Micro Pattern Fabrication for Printed Electronics

Applications, in: Cui, P.B. (Ed.), Recent Advances in Nanofabrication Techniques and Applications. intechopen, pp. 1–22.

Choi, K., Thanh, T.T., Kim, D., 2009. A precise control algorithm for single-span roll- to-roll web system using the back-stepping controller, in: IEEE International Symposium on Industrial Electronics (ISlE. Seoul, pp. 1709–1714.

Choi, K., Zubair, M., Ponniah, G., 2013. . Proc. Inst. Mech. Eng. Part C J. Mech. Eng. Sci. 227, 2361–2376.

Choi, K.-H., Duraisamy, N., Muhammad, N.M., Kim, I., Choi, H., Jo, J., 2012a. . Appl. Phys. A 107, 715–722.

Choi, K.H., Khan, S., Dang, H.W., Doh, Y.H., Hong, S.J., 2010. . Jpn. J. Appl. Phys. 49, 05EC08.

Choi, K.-H., Mustafa, M., Ko, J.-B., Doh, Y.-H., 2012b. . Thin Solid Films 525, 40–44.

Choi, K.H., Rahman, A., Ko, J.B., Rehmani, A., Ali, A., Doh, Y.H., Kim, D.S., 2009. . Int. J. Adv. Manuf. Technol. 48, 165–173.

Choi, K.-H., Rahman, K., Khan, A., Kim, D.-S., 2012c. . J. Mech. Sci. Technol. 25, 3053–3062.

Choi, K.-H., Thanh, T.T., Su, Y.B., Kim, D.-S., 2010. . Int. J. Intell. Syst. Technol. Appl. 9, 300–315.

Cockrell, W.D., 1946. . AIEE Transsactions 65, 617–622.

Das, R., Harrop, P., 2009. Printed, Organic & Flexible Electronics Forecasts, Players & Opportunities 2009-2029.

Derivatives, H., Louis, J., Macdiarmid, A.G., 1977. . J. Chem. Soc. Chem. Commun. 16, 578–580.

Dickey, M.D., Raines, A., Collister, E., Bonnecaze, R.T., Sreenivasan, S. V., Willson, C.G., Raines, Æ.A., Bonnecaze, Æ.R.T., Willson, S.V.S.Æ.C.G., 2007. . J. Mater. Sci. 43, 117–122.

Dimitriev, O.P., Grinko, D. a., Noskov, Y.V., Ogurtsov, N. a., Pud, a. a., 2009. . Synth. Met. 159, 2237–2239.

Ding, J., Wang, M., Zhang, X., Ran, C., 2013. . RSC Adv. 3, 14073.

Duraisamy, N., Muhammad, N.M., Ali, A., Jo, J., Choi, K.-H., 2012a. . Mater. Lett. 83, 80–83.

Duraisamy, N., Muhammad, N.M., Hyun, M.T., Choi, K.H., 2013. . Mater. Lett. 92, 227–230.

Duraisamy, N., Muhammad, N.M., Kim, H.C., Jo, J.D., Choi, K.H., 2012b. . Thin Solid Films 520, 5070–5074.

Dwivedula, R. V., Zhu, Y., Ã, P.R.P., Pagilla, P.R., 2006. . Control Eng. Pract. 14, 409–423.

Ebler, N.A.N. a., Arnason, R., Michaelis, G., D'Sa, N., Sa, N.D., 1993. . IEEE Trans. Ind. Appl. 29, 727–739.

Forrest, S.R., 2003. . Org. Electron. 4, 45–48.

Friend, R.H., Gymer, R.W., Holmes, A.B., Burroughes, J.H., Marks, R.N., Taliani, C., Bradley, D.D.C., Lo, M., Salaneck, W.R., Santos, D.A. Dos, Bre, J.L., 1999. . Nature 397, 121–128.

Gan, Z., Wu, X., Zhou, G., Shen, J., Chu, P.K., 2013. . Adv. Opt. Mater. 1, 554–558.

Gañán-Calvo, A.M., Dávila, J., Barrero, A., 1997. . J. Aerosol Sci. 28, 249–275.

Garter, M., Scofield, J., Birkhahn, R., Steckl, a. J., 1999. . Appl. Phys. Lett. 74, 182.

Gasiorowski, J., Menon, R., Hingerl, K., Dachev, M., Serdar, N., Sariciftci, N.S., 2013. . Thin Solid Films 536, 211–215.

Goldys, E.M., Drozdowicz-Tomsia, K., Xie, F., Shtoyko, T., Matveeva, E., Gryczynski, I., Gryczynski, Z., 2007. . J. Am. Chem. Soc. 129, 12117–22.

Gu, Y., Kuskovsky, I.L., Yin, M., O'Brien, S., Neumark, G.F., 2004. . Appl. Phys. Lett. 85, 3833.

Günes, S., Neugebauer, H., Sariciftci, N.S., 2007. . Chem. Rev. 107, 1324–38.

Guo, C.X., Dong, Y., Yang, H. Bin, Li, C.M., 2013. . Adv. Energy Mater. 3, 997–1003.

Hagen, A., Steiner, M., Raschke, M., Lienau, C., Hertel, T., Qian, H., Meixner, A., Hartschuh, A., 2005. . Phys. Rev. Lett. 95, 197401.

Han, T., Lee, Y., Choi, M., Woo, S., Bae, S., Hong, B.H., Ahn, J., Lee, T., 2012. . Nat. Photonics 6, 105–110.

Hayati, I., Bailey, A., Tadros, T., 1986. . Nature 319, 41–43.

Hayati, I., Bailey, A.I., Tadros, T.H.F., 1987. . J. Colloid Interface Sci. 117, 205–221.

Hayden, H., Park, S., Zhirnov, V., Cavin, R., Kohl, P. a., 2010. . J. Nanoparticle Res. 12, 2335–2347.

Hazra, C., Sarkar, S., Meesaragandla, B., Mahalingam, V., 2013. . Dalton Trans. 42, 11981–6.

Heywang, G., Jonas, F., 1992. . Adv. Mater. 4, 116–118.

Houtepen, A., 2007. Charge injection and transport in quantum confined and disordered systems. Utrecht University, Nederlands.

Hsieh, C., 2009. OLED Lighting in 2009 and Beyond: The Bright Future Analysis. Taiwan.

Janabi-Sharifi, F., Press, A.I.N., 2005. . Control Eng. Pract. 13, 1–13.

Janata, J., Josowicz, M., 2003. . Nat. Mater. 2, 19–24.

Jetson, R., Yin, K., Donovan, K., Zhu, Z., 2010. . Mater. Chem. Phys. 124, 417–421.

Jonas, F., Schrader, L., 1991. . Synth. Met. 43, 831–836.

De Jong, M.P., van IJzendoorn, L.J., de Voigt, M.J. a., 2000a. . Appl. Phys. Lett. 77, 2255.

De Jong, M.P., van IJzendoorn, L.J., de Voigt, M.J. a., Jong, M.P. De, Ijzendoorn, L.J. Van, Voigt, M.J.A. De, 2000b. . Appl. Phys. Lett. 77, 2255.

Jönsson, S.K.., Birgerson, J., Crispin, X., Greczynski, G., Osikowicz, W., Denier van der Gon, a. ., Salaneck, W.., Fahlman, M., 2003. . Synth. Met. 139, 1–10.

Kang, C.C., Lee, B.B., 2008. MIMO Tension Modelling and Control for Roll-To-Roll Converting Machines, in: … the International Federation of Automatic Control, …. pp. 11877–11882.

Khaligh, H.H., Goldthorpe, I. a, 2013. . Nanoscale Res. Lett. 8, 235.

Khan, A., Rahman, K., Hyun, M.-T., Kim, D.-S., Choi, K.-H., 2011. . Appl. Phys. A 104, 1113–1120.

Khan, A., Rahman, K., Kim, D.S., Choi, K.H., 2012. . J. Mater. Process. Technol. 212, 700–706.

Khan, S., Doh, Y.H., Khan, A., Rahman, A., Choi, K.H., Kim, D.S., Hoi, Y., Hyun, K., Soo, D., 2011. . Curr. Appl. Phys. 11, S271–S279.

Khillan, R.K., Lvov, Y.M., Varahramyan, K., 2005. . IEEE Trans. Components Packag. Technol. 28, 748–753.

Kim, D.S., Khan, A., Rahman, K., Khan, S., Kim, H.C., Choi, K.H., 2011. . Mater. Manuf. Process. 26, 1196–1201.

Kim, D.S.D., Rahman, K., Khan, A., Choi, K.H., 2012. . Mater. Manuf. Process. 27, 1295–1299.

Kim, J.Y., Jung, J.H., Lee, D.E., Joo, J., 2002. . Synth. Met. 126, 311–316.

Kim, K., Lee, B.U., Hwang, G.B., Lee, J.H., Kim, S., 2010. . Anal. Chem. 82, 2109–12.

Kim, R.-H., Bae, M.-H., Kim, D.G., Cheng, H., Kim, B.H., Kim, D.-H., Li, M., Wu, J., Du, F., Kim, H.-S., Kim, S., Estrada, D., Hong, S.W., Huang, Y., Pop, E., Rogers, J.A., 2011. . Nano Lett. 11, 3881–6.

Kim, S.W., Yoo, H.S., Kwon, B.-H., Kang, D.S., Suh, M., Jeon, D.Y., 2010. . J. Soc. Inf. Disp. 18, 1104.

Kim, T.-H., Cho, K.-S., Lee, E.K., Lee, S.J., Chae, J., Kim, J.W., Kim, D.H., Kwon, J.-Y., Amaratunga, G., Lee, S.Y., Choi, B.L., Kuk, Y., Kim, J.M., Kim, K., 2011. . Nat. Photonics 5, 176–182.

Klekachev, A. V., Asselberghs, I., Kuznetsov, S.N., Cantoro, M., Mun, J.H., Cho, B.-J., Hotta, J., Hofkens, J., van der Veen, M., Stesmans, A.L., Heyns, M.M., De Gendt, S., 2012. Charge transfer effects in graphene-CdSe/ZnS quantum dots composites, in: Pribat, D., Lee, Y.-H., Razeghi, M. (Eds.), Proceedings of the SPIE. p. 84620L.

Koenig, J.L., Sutton, P.L., Cui, B.J., Wang, A., Edleman, N.L., Ni, J., Lee, P., Armstrong, N.R., Marks, T.J., 2001. . Adv. Mater. 13, 1476–1480.

Kulkarni, A.P., Tonzola, C.J., Babel, A., Jenekhe, S. a., 2004. . Chem. Mater. 16, 4556–4573.

Lahti, M., Leppavuori, S., Lantto, V., 1999. . Appl. Surf. Sci. 142, 367–370.

Lang, U., Naujoks, N., Dual, J., 2009. . Synth. Met. 159, 473–479.

Lari-Najafi, H., Nasiruddin, M., Samad, T., 1989. Effect of initial weights on back-propagation and its variations, in: Conference Proceedings., IEEE International Conference on Systems, Man and Cybernetics. IEEE, pp. 218–219.

Lee, C., Kang, H., Kim, C., Shin, K., 2010. . J. Microelectromechanical Syst. 19, 1243–1253.

Lee, C., Lee, J., Kang, H., Shin, K., 2009. . J. Mech. Sci. Technol. 23, 212–220.

Lee, C., Lee, J., Kim, H., Shin, K., 2008. A Feedforward Tension Control in Drying Section of Roll to Roll e-Printing Systems, in: Proceedings of the 17th World Congress The International Federation of Automatic Control Seoul, Korea, July 6-11, 2008. pp. 11865–11870.

Lee, M.W., Kang, D.K., Kim, N.Y., Kim, H.Y., James, S.C., Yoon, S.S., 2012. . J. Aerosol Sci. 46, 1–6.

Leng, H., Lin, Y., 2011. . Int. J. Smart Nano Mater. 2, 78–91.

Li, H.X., Chen, C.P., 2000. . IEEE Trans. Neural Netw. 11, 356–65.

Li, Y., Wei, L., Zhang, R., Chen, Y., Jiao, J., 2012. . J. Nanomater. 2012, 1–6.

Lim, J., Jun, S., Jang, E., Baik, H., Kim, H., Cho, J., 2007. . Adv. Mater. 19, 1927–1932.

Lin, K.C., 2003. . IEEE Trans. Control Syst. Technol. 11, 109–118.

Lin, Y.-J., Su, Y.-C., 2012. . J. Appl. Phys. 111, 073712.

Lingling Li, Gehui Wu, Guohai Yang, Juan Peng, J.Z. and J.-J.Z., 2010. . Nanoscale.

Liu, F., Jang, M.-H., Ha, H.D., Kim, J.-H., Cho, Y.-H., Seo, T.S., 2013. . Adv. Mater. 25, 3657–62.

Liu, W., Davison, E.J., 2003. . IEEE Trans. Control Syst. Technol. 11, 555–564.

Mason, C.R., Li, Y., O'Brien, P., Findlay, N.J., Skabara, P.J., 2011. . Beilstein J. Org. Chem. 7, 1722–31.

Mastragostino, M., Arbizzani, C., Soavi, F., 2001. . J. Power Sources 97-98, 812–815.

Mastragostino, M., Arbizzani, C., Soavi, F., 2002. . Solid state ionics 148, 493–498.

McDow, B., Rahn, C., 1998. . Tappi J. 81, 197–205.

McQuade, D.T., Pullen, a E., Swager, T.M., 2000. . Chem. Rev. 100, 2537–74.

Mishra, S., Barton, K.L., Alleyne, a G., Ferreira, P.M., Rogers, J. a, 2010. . J. Micromechanics Microengineering 20, 095026.

Muhammad, N.M., Awais, M.N., Duraisamy, N., Kim, D.S., Choi, K.H., 2012a. . Thin Solid Films 520, 1751–1756.

Muhammad, N.M., Duraisamy, N., Dang, H.W., Jo, J., Choi, K.H., 2012b. . Thin Solid Films 520, 6398–6403.

Mukhopadhyay, P., Gupta, R.K., 2011. . Plast. Eng. 32–43.

Mustafa, M., Awais, M.N., Pooniah, G., Choi, K.H., Ko, J., Doh, Y.H., 2012. . J. Korean Phys. Soc. 61, 470–475.

Mustafa, M., Zubair, M., Kim, H.C., Choi, K.H., 2013. . J. Nanoelectron. Optoelectron. 8, 343–348.

Mustapha, N., Fekkai, Z., 2011. . J. Mater. Sci. Eng. A 1, 224–227.

Na, B.S., Kim, S., Jo, J., Kim, D., Na, S.-I., 2008. . Adv. Mater. 20, 4061–4067.

Nguyen, H.T., Nguyen, N.D., Lee, S., 2013. . Nanotechnology 24, 115201.

Nguyen, T.-P., 2011. . Surf. Coatings Technol. 206, 742–752.

Oh, M.H.J., Chen, M., Chuang, C.-H., Wilson, G.J., Burda, C., Winnik, M. a., Scholes, G.D., 2013. . J. Phys. Chem. C 117, 18870–18884.

Ohno, Y., Maruyama, S., Mizutani, T., 2010. Environmental effects on photoluminescence of single-walled carbon nanotubes, in: Marulanda, J.M. (Ed.), Carbon Nanotubes. InTech, pp. 109–123.

Okada, K., Sakamoto, T., 1998. An adaptive fuzzy control for web tension control system, in: IECON '98. Proceedings of the 24th Annual Conference of the IEEE Industrial Electronics Society (Cat. No.98CH36200). IEEE, pp. 1762–1767.

Omer, B.M., 2012. . J. nano Electron. Phys. 4, 6–9.

Onses, M.S., Song, C., Williamson, L., Sutanto, E., Ferreira, P.M., Alleyne, A.G., Nealey, P.F., Ahn, H., Rogers, J. a, 2013. . Nat. Nanotechnol. 8, 667–75.

Ouyang, J., Xu, Q., Chu, C.-W., Yang, Y., Li, G., Shinar, J., 2004. . Polymer (Guildf). 45, 8443–8450.

Pagilla, P.R., Dwivedula, R. V., Zhu, Y., Perera, L.P., 2003. . J. Dyn. Syst. Meas. Control 125, 361.

Pagilla, P.R., Siraskar, N.B., Dwivedula, R. V., 2007. . IEEE Trans. Control Syst. Technol. 15, 106–117.

Park, H.-S., Ko, S.-J., Park, J.-S., Kim, J.Y., Song, H.-K., 2013. . Sci. Rep. 3, 2454.

Park, J., Lee, A., Yim, Y., Han, E., 2011. . Synth. Met. 161, 523–527.

Park, K., Lee, D.-K., Kim, B.-S., Jeon, H., Lee, N.-E., Whang, D., Lee, H.-J., Kim, Y.J., Ahn, J.-H., 2010. . Adv. Funct. Mater. 20, 3577–3582.

Perelaer, J., Smith, P.J., Mager, D., Soltman, D., Volkman, S.K., Subramanian, V., Korvink, J.G., Schubert, U.S., 2010. . J. Mater. Chem. 20, 8446.

Pikul, J.H., Graf, P., Mishra, S., Barton, K., Rogers, J. a, Alleyne, A., Ferreira, P.M., King, W.P., 2010. . 2010 IEEE Sensors 2239–2242.

Pikul, J.H., Graf, P., Mishra, S., Barton, K., Rogers, J.A., Alleyne, A., Ferreira, P.M., King, W.P., 2011. . IEEE Sens. J. 11, 2246–2253.

Ponniah, G., Zubair, M., Doh, Y.-H., Choi, K.-H., 2013. . Int. J. Adv. Manuf. Technol. 71, 153–163.

Pron, A., Rannou, P., 2002. . Prog. Polym. Sci. 27, 135–190.

Pudas, M., Hagberg, J., Leppävuori, S., 2004a. . J. Eur. Ceram. Soc. 24, 2943–2950.

Pudas, M., Hagberg, J., Leppävuori, S., 2004b. . Prog. Org. Coatings 49, 324–335.

Qiao, Q., Li, B.H.H., Shan, C.X.X., Liu, J.S.S., Yu, J., Xie, X.H.H., Zhang, Z.Z.Z., Ji, T.B.B., Jia, Y., Shen, D.Z.Z., 2012. . Mater. Lett. 74, 104–106.

Rahman, K., Ali, K., Muhammad, N.M., Hyun, M., Choi, K., 2012a. . Appl. Phys. A 111, 593–600.

Rahman, K., Khan, A., Muhammad, N.M., Jo, J., Choi, K.-H., 2012b. . J. Micromechanics Microengineering 22, 065012.

Rahman, K., Khan, A., Nam, N.M., Choi, K.H., Kim, D.-S., 2011. . Int. J. Precis. Eng. Manuf. 12, 663–669.

Ramadoss, A., Kim, S.J., 2013. . Mater. Chem. Phys. 140, 405–411.

Raoufi, D., Kiasatpour, A., Fallah, H.R., Rozatian, A.S.H., 2007. . Appl. Surf. Sci. 253, 9085–9090.

Rath, A.K., Bernechea, M., Martinez, L., Konstantatos, G., 2011. . Adv. Mater. 23, 3712–7.

Reddy, V.S., Das, K., Ray, S.K., Dhar, A., 2006. Characteristics of MEH-PPV thin films on ITO electrode for organic light emitting diodes, in: Proc. of 9th Asian Symposium on Information Display. New Delhi, pp. 215–218.

Reich, S., Dworzak, M., Hoffmann, a., Thomsen, C., Strano, M., 2005. . Phys. Rev. B 71, 033402.

Rosa-Fox, N.D. La, 1999. . Opt. Mater. (Amst). 12, 267–271.

Sakamoto, T., 1999. Decentralized controller design of web tension control system in terms of interactions, in: Industrial Electronics, 1999. ISIE’99. Proceedings …. pp. 1466–1471.

Sakamoto, T., Fujino, Y., n.d. Modelling and analysis of a web tension control system, in: Proceedings of the IEEE International Symposium on Industrial Electronics. IEEE, pp. 358–362.

Saleh, M., Park, Y.-S., Baumgarten, M., Kim, J.-J., Müllen, K., 2009. . Macromol. Rapid Commun. 30, 1279–83.

Saygili, G., Ozsoy, C., Oner, I., Zafer, C., Varlikli, C., Icli, S., 2011. . Synth. Met. 161, 196–202.

Schmidt, H., Flügge, H., Winkler, T., Bülow, T., Riedl, T., Kowalsky, W., 2009. . Appl. Phys. Lett. 94, 243302.

Semaltianos, N.G., Logothetidis, S., Hastas, N., Perrie, W., Romani, S., Potter, R.J., Dearden, G., Watkins, K.G., French, P., Sharp, M., 2010. . Chem. Phys. Lett. 484, 283–289.

Sharma, P.K., Kumar, M., Pandey, A.C., 2010. . J. Nanoparticle Res. 13, 1629–1637.

Shirasaki, Y., Supran, G., Bawendi, M., Bulović, V., 2012. . Nat. Photonics 7, 13–23.

Sidorov, A.N., Yazdanpanah, M.M., Jalilian, R., Ouseph, P.J., Cohn, R.W., Sumanasekera, G.U., 2010. . Nanotechnology 18, 135301.

Son, D.I., Kwon, B.W., Park, D.H., Seo, W.-S., Yi, Y., Angadi, B., Lee, C.-L., Choi, W.K., 2012. . Nat. Nanotechnol. 7, 465–71.

Song, S., Sul, S., 2000. . IEEE Trans. Ind. Appl. 36, 640–648.

Song, W., Xie, J., Liu, S., Zheng, Y., 2012. . Int. J. Electrochem. Sci. 7, 2164–2174.

Suga, T., Ohshiro, H., Sugita, S., Oyaizu, K., Nishide, H., 2009. . Adv. Mater. 21, 1627–1630.

Sun, Y., Shi, G., 2013. . J. Polym. Sci. Part B Polym. Phys. 51, 231–253.

Sung, D., de la Fuente Vornbrock, a., Subramanian, V., 2010. . IEEE Trans. Components Packag. Technol. 33, 105–114.

Suo, B., Su, X., Wu, J., Chen, D., Wang, A., Guo, Z., 2010. . Mater. Chem. Phys. 119, 237–242.

Takei, K., Fang, H., Kumar, S.B., Kapadia, R., Gao, Q., Madsen, M., Kim, H.S., Liu, C.-H., Chueh, Y.-L., Plis, E., Krishna, S., Bechtel, H. a, Guo, J., Javey, A., 2011. . Nano Lett. 11, 5008–12.

Tang, C.W., VanSlyke, S. a., 1987. . Appl. Phys. Lett. 51, 913.

Thejo Kalyani, N., Dhoble, S.J., 2012. . Renew. Sustain. Energy Rev. 16, 2696–2723.

Tran, T.T., Choi, K.-H., Chang, D.-E., Kim, D.-S., 2011a. . J. Adv. Mech. Des. Syst. Manuf. 5, 329–346.

Tran, T.T., Choi, K.-H., Chang, D.-E., Kim, D.-S., 2011b. . J. Adv. Mech. Des. Syst. Manuf. 5, 7–21.

Tran, T.T., Zubair, M., Ponniah, G., Choi, K., 2013. An Evolution Strategy Based Autonomous Algorithm for Roll-to-roll Web Control System, in: Advances in Intelligent Systems and Computing. pp. 717–729.

Tsai, K.-H., Shiu, S.-C., Lin, C.-F., 2008. Improving the conductivity of hole injection layer by heating PEDOT:PSS, in: Kafafi, Z.H., Lane, P.A. (Eds.), Organic Photovoltaics. Proc. of SPIE, p. 70521B–70521B–8.

Tuan, N.H., Koh, K.H., Nga, P.T., Lee, S., 2011. . J. Cryst. Growth 326, 109–112.

Umar, A., Kim, S.H., Lee, Y.-S., Nahm, K.S., Hahn, Y.B., 2005. . J. Cryst. Growth 282, 131–136.

Valenzuela, M., 2003. . IEEE Trans. Ind. Appl. 39, 294–304.

Wang, C., Wang, Y., Yang, R., Lu, H., 2004. . IEEE Trans. Ind. Electron. 51, 381–386.

Wang, T., Qi, Y., Xu, J., Hu, X., Chen, P., 2005. . Appl. Surf. Sci. 250, 188–194.

Wang, Y., Sun, X.W., Member, S., Kia, G., Goh, L., Igzo, A.I.I., 2011. 58, 480–485.

Werbos, P.J., 1990. 78, 1550–1560.

Willemse, C.M., Tlhomelang, K., Jahed, N., Baker, P.G., Iwuoha, E.I., 2011. . Sensors (Basel). 11, 3970–87.

Yang, L., Rida, A., 2007. . Microw. Theory … 55, 2894–2901.

Yeh, D.-M., Huang, C.-F., Lu, Y.-C., Yang, C.C., 2008. . Appl. Phys. Lett. 92, 091112.

Yildiz, I., Raymo, F.M., 2006. . J. Mater. Chem. 16, 1118.

Yoffe, A.D., 2002. . Adv. Phys. 51, 799–890.

Yoshida, T., Takagi, S., Muto, Y., Shen, T., 2008. . IEEJ Trans. Ind. Appl. 128, 1133–1139.

Zhang, X., Alloul, O., Zhu, J., He, Q., Luo, Z., Colorado, H. a., Haldolaarachchige, N., Young, D.P., Shen, T.D., Wei, S., Guo, Z., 2013. . RSC Adv. 3, 9453.

Zhang, Z., Shao, C., Gao, F., Li, X., Liu, Y., 2010. . J. Colloid Interface Sci. 347, 215–20.

Zhu, J., Wei, S., Patil, R., Rutman, D., Kucknoor, A.S., Wang, A., Guo, Z., 2011. . Polymer (Guildf). 52, 1954–1962.

Zubair, M., Duraisamy, N., Choi, K.H., Hyun, M.T., 2013. . J. Mater. Sci. Mater. Electron. 25, 1–19.